2006

Coherent Structures and Aeolian Saltation

Jean Taylor Ellis
University of South Carolina - Columbia, jtellis@sc.edu

Publication Info
2006. Copyright 2006, Jean Ellis

COHERENT STRUCTURES AND AEOLIAN SALTATION

A Dissertation

by

JEAN TAYLOR ELLIS

Submitted to the Office of Graduate Studies of
Texas A&M University
in partial fulfillment of the requirements for the degree of

DOCTOR OF PHILOSOPHY

December 2006

Major Subject: Geography

COHERENT STRUCTURES AND AEOLIAN SALTATION

A Dissertation

by

JEAN TAYLOR ELLIS

Submitted to the Office of Graduate Studies of
Texas A&M University
in partial fulfillment of the requirements for the degree of

DOCTOR OF PHILOSOPHY

Approved by:

Chair of Committee,	Douglas J. Sherman
Committee Members,	David M. Cairns
	Steven F. DiMarco
	Vatche P. Tchakerian
Head of Department,	Douglas J. Sherman

December 2006

Major Subject: Geography

ABSTRACT

Coherent Structures and Aeolian Saltation.

(December 2006)

Jean Taylor Ellis, B.S., University of Southern California;

M.S., University of Southern California

Chair of Advisory Committee: Dr. Douglas Joel Sherman

Aeolian sand transport models, widely employed by coastal scientists and managers, assume temporal and spatial homogeneity within the saltation field. This research questions that assumption by demonstrating that the saltation field is event-driven, therefore indicating that the saltation field is not temporally steady. The findings from this research may explain a portion of the conclusions from previous studies that indicated inequalities between model-estimated and field-measured aeolian sand transport.

The relationship between unsteadiness in a turbulent wind field and pulses in a sand transport field was investigated on a beach near Shoalhaven Heads, New South Wales, Australia. Microphone-based saltation sensors, “miniphones,” and thermal anemometers (both instruments constructed exclusively for this field experiment) were co-located (0.02 m separation on center) and deployed between 0.01 and 0.0225 m above the bed, and sampled at 6000 Hz. Average grain size at the field site was 0.30 mm. Five runs totaling 2050 seconds of wind and saltation data were analyzed.

The continuous wavelet transform, using the Morlet wavelet base, was the principle method for analyzing the wind and saltation records. The cross continuous wavelet transform was used to analyze the wind and saltation time series concurrently. Wind, saltation, and cross events were discerned by selecting wavelet power coefficients between wavelet scales of 0.4 and 3.0 seconds and with coefficients exceeding the 95% confidence interval.

Average event spacing was 6.10, 6.50, and 6.73 seconds for the wind, saltation, and cross events, respectively. The average event spacing measured in this research was compared to the empirical-based model presented by Rao, Narashimha, and Narayanan (1971). The correspondence between the model and this research strongly suggests that bursting-type coherent structures were present. The durations of average wind, saltation, and cross events were 1.87, 2.10, and 1.73 seconds, respectively. Integral time scales, calculated using normalized auto correlation and power spectral density analysis, were approximately two seconds for the wind and saltation systems. The temporal coincidence of the integral time scale estimations and the event durations for the wind and saltation system strongly suggests that wind events are driving sand transport events.

ACKNOWLEDGEMENTS

Numerous individuals have contributed to this research, particularly my advisory committee. Douglas Sherman has always been a supportive and enthusiastic advisor and this work was greatly supplemented by our discussions and his suggestions. Steven DiMarco provided critical advice during the data analysis portions of this work. Vatche Tchakerian and David Carins provided useful and thoughtful comments.

This research was supported by National Science Foundation Doctoral Dissertation Research Improvement Grant (Award #0425770, co-PI, Douglas Sherman) and a National Science Foundation East Asia Summer Institute for US Graduate Students Grant (Award #0413541), that is also supported by the Australian Academy of Sciences. Texas A&M University, Department of Geography contributed a small portion of funds. During 2005, I was suported by the John A. Knuass National Oceanic and Atmospheric Administration (NOAA) Sea Grant Fellowship (based at NASA Headquarters). Texas Sea Grant, led by Dr. Robert Stickney, should be acknowledged for the supplemental support to this fellowship.

The following people partipated in the fieldwork: Eugene Farrell, Wansang Ryu, Barry Preist, Rebecca Morrison, and Diane Horn. The field research was conducted while I was a visiting scholar at the University of Sydney, School of Geosciences, Coastal Studies Institute. Andy Short was my host and was wonderful to me during my stay in Australia, as was his wife Julia. David Mitchell, Nelson Cano, Graham Lloyd, and John Connell, all at the University of Syndey, helped to arrange vehicles, time in the sediment laboratory, and allowed me to borrow University equipment, for example. Rob Brander (University of New South Wales) also assisted me with logisitics during my field experiment and during my stay in Australia.

TABLE OF CONTENTS

Page

LIST OF FIGURES

FIGURE Page

FIGURE Page

FIGURE Page

LIST OF TABLES

1. INTRODUCTION

1.1 Research Statement

The goal of this research is to identify and then characterize the relationships between turbulent wind events and sand transport events.

1.2 Conceptual Background

Bagnold attempted to explain, from a physics perspective, “some of the many strange phenomena produced by the natural movement of sand” over the Earth (1941: xvii). One of his most widely employed expressions relating mean wind velocity and mean grain sizes is still used, almost three quarters of century later, to estimate sand transport rates (Bagnold, 1936). Others, Kawamura (1951) and Lettau and Lettau (1977), for example, have formulated comparable aeolian transport models by assuming, akin to Bagnold, temporal and spatial consistency within the wind and saltation fields. However, irregularities in the transport field (Fig. 1-1), often manifested as streamers (c.f., Baas and Sherman, 2005), demonstrate that the saltation field is unsteady. This unsteadiness contributes to the discrepancies found between field measurements and model predictions of sediment transport (c.f., Sherman et al., 1998).

It has been well established that during high velocity conditions the wind field close to the bed is turbulent, unsteady, and dominated by quasi-coherent structures (Robinson, 1991a; Clifford and French, 1993). Grass (1971) and Laufer (1975) indicated that the most dominant quasi-coherent structure is the bursting structure. The burst and sweep is a multistage highly-intermittent process (or structure) in which fluid is rapidly ejected from, (burst) and injected toward, (sweep) the boundary, and is critical to sediment transport (Grass, 1971; Jackson, 1976). Bursting is also apparent during the ejection of hairpin vortices that occur throughout the boundary layer and have been linked to sediment transport (Best, 1992; Zhou et al., 1999; Adrian et al., 2000). Using the terminology from Hunt and Morrison (2000), the formation mechanism of burst and sweep are ‘bottom-up’ and the hairpin vortices are ‘top-down’ (Zhao et al., 1999).

This dissertation follows the style of Geomorphology.

Fig. 1-1. Unsteadiness in aeolian sand transport, dominated primarily by saltation. (Image provided by E.J. Farrell).

Only relatively recently (compared to Bagnold, 1936), have field-based studies been designed to investigate unsteadiness in the wind field and to link that unsteadiness to fluctuations in aeolian transport (Lee, 1987). These studies have employed qualitative, visual matching (e.g., Butterfield, 1991; Stout and Zobeck, 1997; Wiggs et al., 2004), or quantitative methods such as, the variable interval time averaging (VITA) method (Bauer et al., 1998; Baas, 2003), regression analysis (Lee, 1987; Sterk et al., 2002; Leenders et al., 2005), or wavelet analysis (Schönfeldt and von Löwis, 2003; Baas, 2006) to establish relationships between the wind and sand fields. Their findings ranged from mixed to inconclusive. Furthermore, none of these studies quantified the characteristic scales describing the temporal duration of individual turbulent wind events or individual pulses in sediment transport. This research aims to establish and quantify that correspondence for the transport of sand by wind. Recent research, outside aeolian geomorphology, has indicated that the continuous wavelet transform is a viable method for event detection, and therefore, this method has been adopted herein (c.f., Farge, 1992; Salmond, 2005).

1.3 Research Hypotheses

Major hypothesis: Pulses in aeolian transport are correlated with the unsteadiness in the wind field. This hypothesis involves three secondary hypotheses.

Secondary hypotheses: 1) Unsteadiness in the wind and sand fields can be identified by the continuous wavelet transform function; 2) Coherent structures are the dominant forcing mechanism driving sediment transport; 3) Bursting structures can be identified in the turbulent boundary layer.

1.4 Research Objectives

The main objectives of this research in support of testing the stated hypotheses are:

1. To design and implement a field experiment to measure short-term wind and sand transport fluctuations; and
2. To analyze the resultant time series for event detection, characterization, and matching.

1.5 Dissertation Outline

This dissertation comprises seven sections and two appendices. A brief introduction to turbulent flow in boundary layers, coherent structures, and identification of structures in the boundary layer is found in section 2. That section also includes a discussion on aeolian sediment transport, focusing on saltation, and the interactions that occur during saltation. Unsteadiness in aeolian saltation is discussed. The background section concludes with a discussion on event detection, in particular the variable interval time averaging (VITA) method and the continuous wavelet transform method. Section 3 describes the field site and the main instrumentation used in this research, thermal anemometers to measure wind, and a ‘miniphone’ to measure sediment transport intensity. Data reduction and signal processing methods are presented in section 4. The results of the grain size analysis are also presented in that section. Section 5 presents the data analysis for thermal anemometer and miniphone records. A visual comparison to qualitatively analyze the wind and saltation fields is presented. The results from regression analysis and cross covariance analysis follow. To determine the integral time scales, the normalized autocorrelation function and power spectral density analysis were employed. The rest of that section focuses on wavelet analysis. Wind and sand events were selected from the continuous wavelet transform analysis and the cross continuous wavelet transform analysis using criterion established in this research. Characteristics of the wind, saltation, and cross events are presented in that section. Section 6 synthesizes the findings presented in the previous section. That section also describes the characteristics of the coherent structures measured in this research and hypothesizes on their formation mechanisms. The final section presents the conclusions of this dissertation and discusses the implications of this research to aeolian geomorphology.

2. BACKGROUND

2.1 Section Introduction

This section begins with an introduction to the structure of turbulent boundary layers. The evolution of turbulence being perceived as a chaotic phenomena to a phenomena organized by quasi-coherent structures is discussed. Saltation, the most dominant aeolian transport mechanism is described. Unsteady wind and saltation fields and previous research investigating this unsteadiness is discussed. The final portion of this section discusses methods to detect events in wind and saltation time series. The main methods presented are the variable interval time averaging (VITA), this method will not be employed here, and the continuous wavelet transform methods.

2.2 Fluid Flow

2.2.1 Boundary Layers

When fluid flows across a surface, friction causes the formation of a boundary layer. Flow velocity increases from zero at the boundary to 99% of the free stream velocity at the outer edge of the boundary layer (Schlichting and Gersten, 2000), creating velocity gradients that produce shear stresses. The discussion below will focus on fully developed turbulent boundary layers over rough surfaces, because turbulent conditions occur during aeolian transport.

The turbulent boundary may be characterized as having an inner (close to the bed) and an outer (close to the free stream velocity) region (Fig. 2-1). Under turbulent flow conditions the wind velocity profile in the inner region is semi-log linear, and can be described using the “law of the wall” equation (first described by Prandtl, 1932):

$$\frac{u_z}{u_*} = \frac{1}{\kappa}\left(\ln\frac{z}{z_0}\right) \tag{2-1}$$

where u_* is shear velocity, u_z is flow velocity at elevation z above the bed, κ is the von Kármán constant (~0.4), and z_0 is the roughness length, or the height above the bed where flow velocity approximates to zero. The roughness length is typically 1/30th grain diameter (for uniform grains), but may be an order of a magnitude larger during periods of sediment transport (Sherman, 1992). The outer layer displays ‘apparent’ friction from turbulent motions, dominated by eddy mixing and the flow is described by the velocity defect law (Middleton and Southard, 1984):

$$\frac{u_z - u_\infty}{u_*} = f\left(\frac{z}{\delta}\right) \tag{2-2}$$

where u_∞ is free stream flow velocity and δ is boundary layer thickness. The overlap layer, (Fig. 2-1) comprising about the lower 10-30% of the total boundary layer (Bauer et al., 2004), is also called the logarithmic layer because the effects of the logarithmic-based "law of the wall" and the velocity defect law are both apparent (Middleton and Southard, 1984).

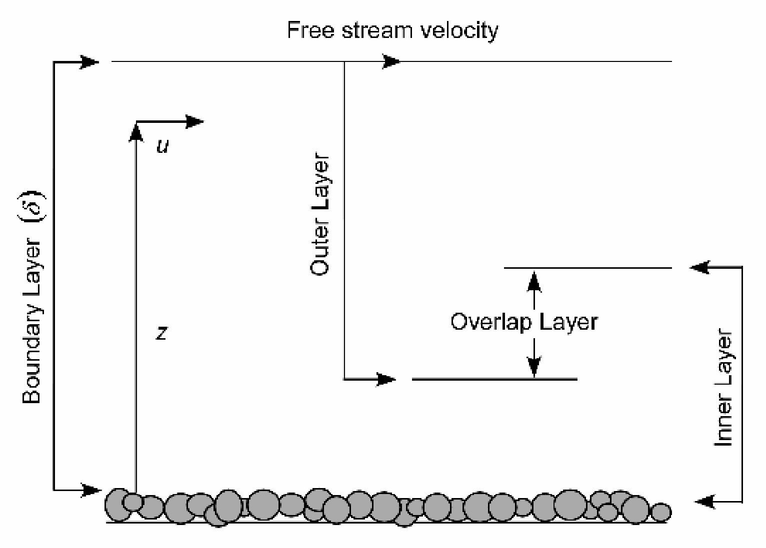

Fig. 2-1. Regions of the turbulent boundary layer. Diagram is not to scale. (Adapted from Middleton and Southard (1984), their Fig. 5-11).

2.2.2 Turbulence

The following is a brief review of turbulence summarized from Vennard and Street (1992) and Clifford and French (1993). Early works (e.g., Reynolds, 1895) defined turbulence as "entirely chaotic motion of small fluid masses through short distances in every direction as flow takes place" (Vennard and Street, 1982: 284, describing the history of turbulence). The motion of a fluid parcel may be split into three orthogonal components (u, v, and w) in the x, y, and z coordinate system (Fig. 2-2). Each velocity component comprises a mean (designated by the overbar) and a fluctuating, time varying, part (designated by a prime):

$$u = \overline{u} + u' \tag{2-3}$$

$$v = \overline{v} + v' \tag{2-4}$$

$$w = \overline{w} + w' \tag{2-5}$$

The *u* component is horizontal and parallel (along the streamline), *v* is perpendicular to *u*, and *w* is perpendicular to the *u*-*v* plane. Prandtl (1938) introduced the mixing layer (*l*), a concept that turbulent eddies transfer energy between the horizontal regions (or mixing layers) found in the boundary layers. Turbulent fluid particles coalesce into eddies and traverse in the *y* direction within their mixing layer (*l*) and transfer energy. The eddy size increases with increasing distance from the bed. Clifford and French (1993) noted that despite the recognition of these semi-organized features in the turbulent boundary layer (thus, somewhat questioning earlier, "chaotic" definitions of turbulence) it was not until the mid-1950s that efforts to visualize and measure the time-averaged motions turbulence (eddies) were made. Laufer (1975) indicated that it has been since the 1960s that there has been an agreement amongst those that study fluid dynamics that momentum transport in the turbulent boundary layer is not random and that there is a level of coherence to the flow.

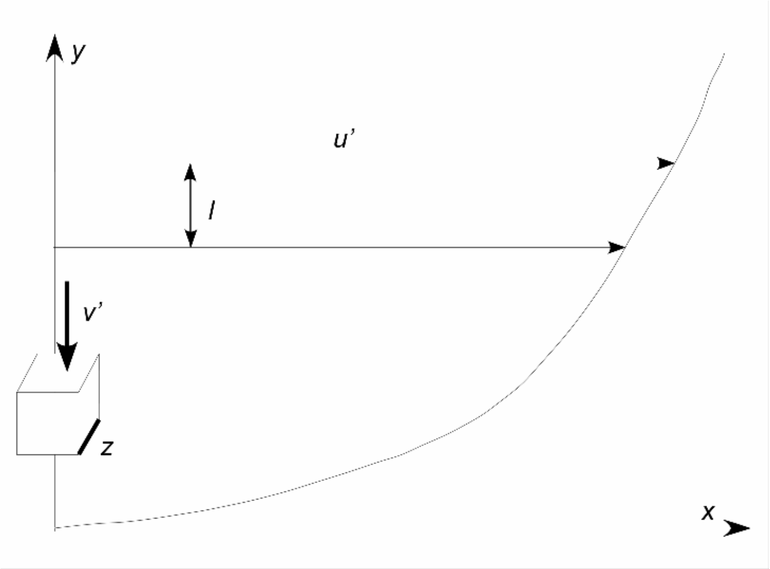

Fig. 2-2. Conceptual diagram to indicate mixing layer length (*l*) and the instantaneous velocity components. (Adapted from Fox (1977), his Fig. 5-3).

2.2.3 Coherent Structures

The occurrence of eddies, vortices, and other forms of coherent flow structures is common within turbulent boundary layers. A coherent motion (structure), as defined by Robinson (1991a: 602) is:

> a three-dimensional region of the flow over which at least one fundamental flow variable (velocity component, density, temperature, etc.) exhibits significant correlation with itself or with another variable over a range of space and/or time that is significantly larger than the smallest local scales of flow [and]
>
> is responsible for the maintenance (production and dissipation) of turbulence in the boundary layer.

Kline and Robinson (1989) and Robinson (1991a) completed a community-wide assessment on quasi-coherent structure research. Their efforts resulted in identification of major classifications of quasi-coherent structures: 1) streaks; 2) sweeps; 3) ejections; and 4) vortical motions (this category is an agglomeration of larger boundary layer motions (Best, 1993)) which will be discussed below. When describing boundary layer characteristics, dimensionless units are employed, designated by a ($^+$). Boundary layer dimensionless height (y^+) is:

$$y^+ = \frac{yu_*}{\nu} \tag{2-6}$$

where y is the ‘real’ elevation above the wall, u_* is shear velocity , and ν is kinematic viscosity. For all the examples in this section, the ‘real’ distances are shown in parentheses after the dimensionless elevations and $\nu = 1.51*10^{-5} m^2 / s$ (for 20°C air) and $u_* = 0.25 m/s$. Boundary layer dimensionless time (T^+), also equivalent to the turbulent bursting frequency (Rao et al., 1971), is scaled to the outer boundary layer parameters:

$$T^+ = \frac{TU_\infty}{\delta} \tag{2-7}$$

where T is ‘real’ time, U_∞ is free stream velocity, δ is boundary layer thickness, and $3 < T^+ < 7$ (Rao et al., 1971).

Runstadler et al. (1963) were the first to observe turbulent ‘eruptions’ originating from the inner portions of the turbulent boundary layer. Kline et al. (1967) described that the streaks originate at elevations close to the wall $y^+ < 5$ (0.030 mm) and had low velocities compared to the surrounding fluid. The streaks begin to oscillate, elevate, and accelerate around $8 < y^+ < 10$

(0.060 mm), and break up at approximately $10 < y^+ < 30$ (0.181 mm) (Fig. 2-3). Kline et al. (1967) termed these events ‘streak-ejections.’

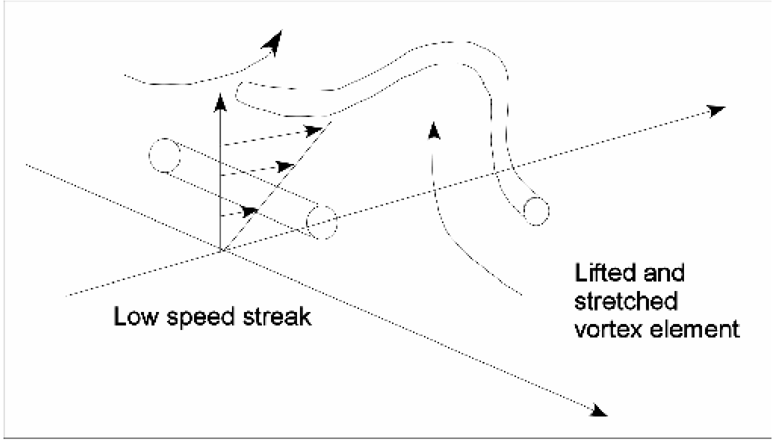

Fig. 2-3. Ejection processes envisioned by Kline et al. (1967). (Redrawn from their Fig. 19b).

Corino and Brodkey (1969) integrated the ‘streak-ejection’ process described by Kline et al. (1967) when they described the burst and sweep quasi-coherent turbulent structures. In the burst and sweep process, bursting is the streak-ejection that leaves a ‘hole’ at the wall that is filled by a high-speed fluid mass in an event called sweeping. Several dimensionless heights have been reported for bursting, in terms of the burst and sweep process: Kline et al. (1967), Corino and Brodkey (1969), and Kim et al. (1971) report dimensionless heights of approximately 30, 70, and 100, respectively ($y^+ = 100$ is 0.604 mm).

Burst and sweep events have been observed in aeolian and fluvial systems (e.g., Drake et al., 1988; Kostaschuk et al., 1991; Bauer et al., 1998), however, the relationship between these events and sediment transport is not well understood. Jackson (1976) and Grass (1983) indicate that burst and sweep is a critical factor in sediment transport. Many suggest a relationship between the sweep and sediment entrainment because they determined a majority of stress is coupled with sweep (Grass, 1971; Sterk et al., 1996; Bauer et al., 1998). However, others found a majority of stress residing in the burst (Kim et al., 1971; Wallace et al., 1972). Williams (1986) indicates that incipient grain motions are linked to both burst and sweep. Baas (2003) suggests that burst and sweep explains, in a general fashion, transport unsteadiness. The order of events, i.e., a sweep proceeding or trailing a burst, is also under debate (McLean et al., 1996; Sterk et al., 1996; Bauer et al., 1998).

Head and Bandyopadhayay (1981) and Smith et al. (1991) demonstrated that low velocity streaks close to the bed (described by Kline et al., 1967) can be ejected ('bursted') and horseshoe-shaped (wider along the *w*-axis) during lower flow velocities or hairpin shaped (narrower along the *w*-axis and higher along the *y*-axis) during higher flow velocities. These quasi-coherent structures differ from burst and sweep because of their shape and their size and are similar because they involve an ejection process that removes fluid from the lower portions of the boundary layer flow.

Smith and Walker (1990) and Zhou et al. (1999) visually determined that initial hairpin vortices result in the formation of subsidiary (nested) hairpin formation and growth. Smith and Walker (1990) and Head and Bandyopadhayay (1981) indicate that the ejection angle of the hairpins is 40-45° to the mean flow, while Zhou et al. (1999) report angles ranging between 8-75° (they reported an average of 45°) (Fig. 2-4). Head and Bandyopadhayay (1981) observed agglomerations of hairpin vortices during high flow conditions throughout the entire boundary layer (in the *y*-direction). Smith and Walker (1990) suggest that the origination of nested hairpin vortices involves low-speed streaks (Fig. 2-4), ones similar to those described by Kline et al. (1967). Zhou et al. (1999: 393) state that there is an "enhanced downward flow associated with its [the hairpin vortex] lift-up process," thus implying an interaction with the upper/outer boundary layer.

Vortices in the turbulent boundary layer have been identified as the "sinews and muscles of turbulence" (Küchermann, 1965) and they play "an important role in the overall turbulence dynamics" (Chakraborty et al., 2005: 189). Robinson (1991b: 169) relates the vortical motion to a human heart because the mass and momentum is "pumped" throughout the turbulent boundary layer. Vortical structures also contribute to a majority of the turbulence in the upper logarithmic portion of the boundary layer (Robinson, 1990). Adrian et al. (2000) conducted laboratory experiments (in air, during high velocity conditions) and report that hairpins are most frequently observed in groups. Adrian et al. (2000: 42) state that "it cannot be disputed that hairpin vortex signatures populate the boundary layer abundantly. They are found everywhere…" In his flow visualization model, Best (1992: 808) linked hairpin vortices and nested hairpins to the "patchiness of [sediment] entrainment observed in many experiments."

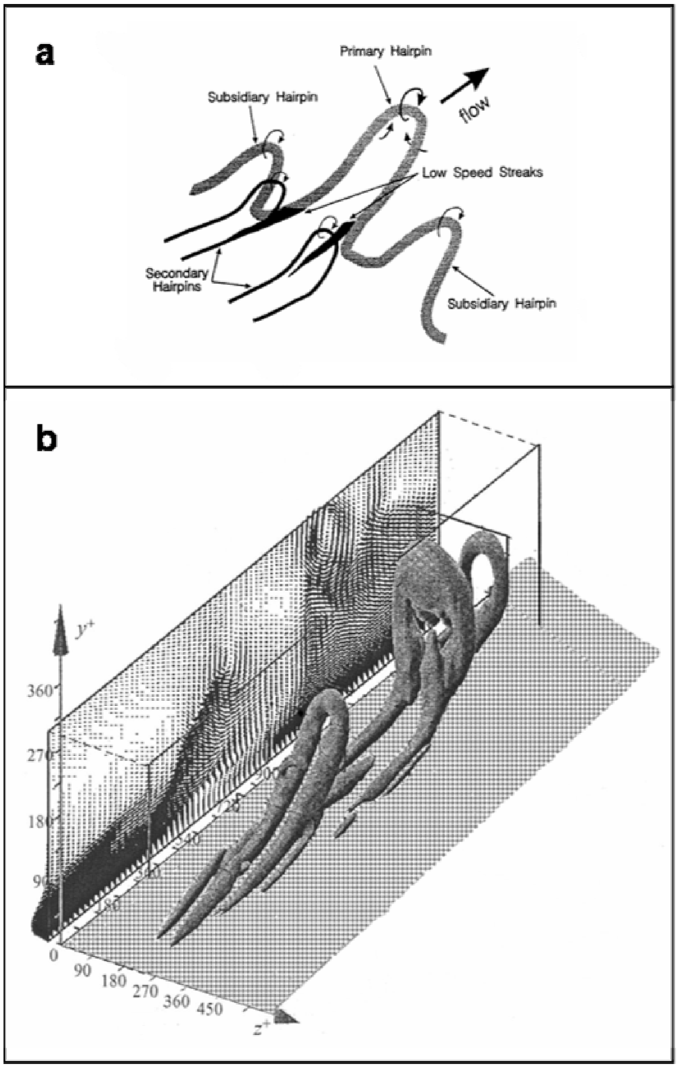

Fig. 2-4. (a) Nested hairpin vortices originating from low-speed streaks at an angle of 45° to mean flow. (Redrawn after Smith and Walker, 1990). (b) Sequence of multiple vortices. (Redrawn after Zhou et al. (1999), their Fig. 10b).

Hunt and Morrison (2000) introduced a model describing dominant coherent structure movement in the boundary layer according to the flow velocity regime. When high flow velocity conditions prevail in the boundary layer, Hunt and Morrison (2000), and Hunt and Carlotti (2001), indicate that the ‘top-down’ model is more dominant. In the ‘top-down’ model, turbulent eddies from the top of the boundary layer travel down toward the bed and elongate (in the *x*-direction) with decreasing distances toward the wall. These turbulent eddies impact the bed and a local internal boundary layer (IBL in Fig. 2-5) is formed within the “eddy surface layer (ESL, Fig. 2-5). Internal sub-structures called ‘anti-splats’ (Perot and Moin, 1995) form from eddies ejecting away from the bed with a periodicity scaled to the outer boundary layer (shown in Fig. 2-5 as ‘substructures’). In the ‘bottom-up’ model, local instabilities at the surface lead to the bursting sequence in the burst and sweep quasi-coherent structures. The local instabilities are an order of magnitude (temporally) smaller than top boundary-originated structures and scale to:

$$\frac{\nu}{u_*^2} \tag{2-8}$$

where ν is kinematic viscosity and u_* is shear stress (Hunt and Carlotti, 2001). The bottom-up model is consistent with the findings of Schoppa and Hussain (1997) and Jiménez and Penelli (1999) and is characteristic to boundary layers with lower flow velocities (Hunt and Morrison, 2000).

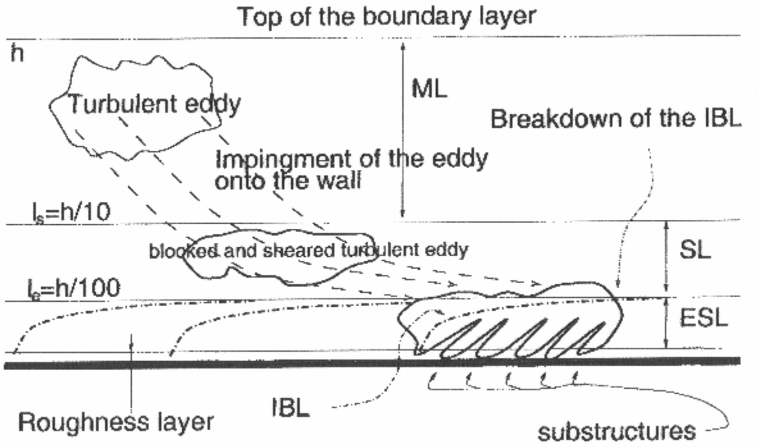

Fig. 2-5. Sketch of the turbulent boundary layer according to Hunt and Morrison (2000) where SL surface layer is and ESL is eddy surface layer. (Adapted from Hunt and Carlotti (2001) (their Fig. 1), in which they summarize the findings from Hunt and Morrison (2000)).

2.2.4 Characterizing Boundary Layer Turbulence

In attempting to link turbulence (coherent structures or events) to sediment transport, several have also characterized the length and time scales of the turbulent events within the boundary layer using the Kolmogorov inertial sub-range (Kolmogorov, 1941), Monin-Obukhov length scale, and the integral time scale, for example. Liao et al. (2004: 1025) indicated that the integral time scale is “the key characteristic time for the turbulence,” therefore will be used in this dissertation for turbulent detection.

The amount of correlation within one record (e.g., a turbulent wind time series) can be detected by calculating the autocorrelation function (defined here as ρ_{xx}). For turbulent flows, and many other geophysical processes, the correlation diminishes with increasing lag (τ). The integral time scale (T_i) is the time at which $\rho_{xx}(\tau)$ decreases rapidly so that the integral converges (Pope, 2000) and can be calculated from the autocorrelation function:

$$T_i = \int_0^\infty \rho_{xx}(\tau)\delta\tau \qquad \text{(2-9)}$$

Quadrio and Luchini (2003) suggest that a more simple method to calculate integral time scale is to use the first zero-crossing of the autocorrelation function, and this method was employed by Baas (2006). The integral time scale is also the frequency of the peak power spectral density (Pope, 2000).

2.3 Aeolian Sediment Transport

There are four recognized aeolian sediment transport mechanisms: creep, reptation, saltation, and suspension. Saltation is the dominant mode comprising approximately 75% of all aeolian sediment transport (Bagnold, 1941) and therefore is the focus of this review. Saltation typically comprises sediments ranging in size from 0.06-0.5 mm. Namikas (1999) estimated average saltation path lengths of 0.50 m and horizontal velocities of 2-3 m/s. Fig. 2-6 diagrams the basic trajectory of saltation. The total number of saltating particles (N_t) comprises the sum of particles entrained by aerodynamic (N_a) or impact (N_i) generated forces. Aerodynamic generated ejection is required when no external disturbances (i.e., transporting grains) are present. N_a is proportional to excess shear stress $(\tau_a - \tau_c)$:

$$N_a = \zeta(\tau_a - \tau_c) \qquad \text{(2-10)}$$

where ξ is a constant (10^5 grains Newton^{-1} sec^{-1}; Anderson and Haff, 1991), τ_a is short term mean shear stress at the bed, and τ_c critical shear stress, or the minimum shear stress needed for aerodynamic entrainment.

During their laboratory investigations Gerety (1985), McKenna Neuman and Nickling (1994), and Butterfield (1999b) estimated that between 50 and 80% of sediment flux occurs 0.02 m above the bed. However, it has been documented (e.g., Farrell and Sherman, 2003) that laboratory-based vertical flux profiles are significantly different than those derived from field-based measurements; the largest difference being that saltation is not as concentrated close to the bed (c.f., Namikas (2003) for equations). Namikas (1999) reported roughly 80% of transport is at elevations below 0.10 m in the field.

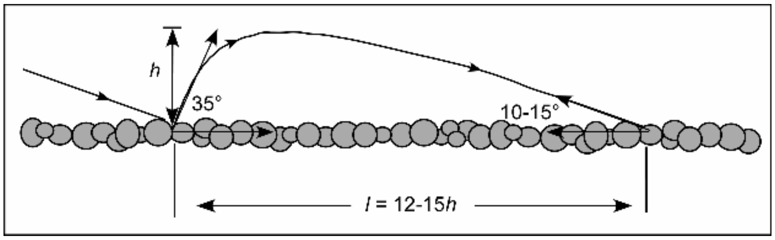

Fig. 2-6. Cartoon showing basic trajectory of saltation. (Adapted from Lancaster and Nickling (1994), their Fig. 17-13).

2.4 Saltation and Wind Interactions During Transport

2.4.1 Response Time

Extensive work in wind tunnels and with numerical modeling has measured or modeled the wind field and the transport of sand to determine the response time of sand to fluctuating wind speeds (Anderson and Haff, 1988, 1991; Butterfield, 1991, 1993, 1998; Spies et al., 2000). The Aberdeen numerical model (Anderson and Haff, 1991; McEwan and Willetts, 1991) shows that equilibrium between a saltation layer and an upper, sediment-free zone, comprises two response stages. The first stages occurring within approximately one second of an increase in wind velocity, is when the sand transport rate reaches equilibrium with the wind within the saltation layer, and is inversely related to shear velocity. The second phase occurs when the boundary layer above the saltation layer reaches equilibrium with the effective roughness changes from the enhanced saltation cloud. The numerical models reveal that the secondary response time is approximately 40 seconds (McEwan and Willets, 1991; McEwan, 1993).

Butterfield (1991; 1993) confirmed the dual response time during wind tunnel experiments. He measured primary and secondary response times of one second or less and approximately 100 seconds. He also concluded that the magnitude of velocity increase corresponds with response time, larger velocity increases have longer (2-3 s) response times. Lastly, Butterfield (1993) determined that shear stress and velocity adjust faster for increasing velocity than decreasing velocity. Spies et al. (2000) measured 2-3 s and 3-4 s primary response times for steadily increasing and decreasing winds, respectively.

A shortcoming of response time modeling in laboratory environments is that a steady increase or decrease of wind velocity is applied, a condition not common in nature. In the field, constant wind fluctuations may prevent the attainment of the equilibrium response. The ability to measure response time in the field has, until recently, been restricted because of instrumentation. Typically, sand traps have been used to measure time averaged transport rates, but the use of high frequency sensors, such as those used by Baas (2003) and Jackson and McCloskey (1997), paired with anemometers have overcome this limitation. Baas (2003) reported a 0.5 second primary response time and several have reported a one second response time (Jackson and McClosky, 1997; Sterk et al., 1998; Davidson-Arnott et al., 2003; Schönfeldt and von Löwis, 2003; Wiggs et al., 2004). However, McEwan and Willetts (1993: 106) suggest that a one second response time “may be an overestimate during “gusty”” winds because a grain will more easily be accelerated by an already present grain cloud rather than one initiated from zero flux.

2.4.2 Unsteadiness in the Saltation Field

Several studies have attempted to relate fluctuations in a wind field to variations in a transport field using qualitative and quantitative methods. These studies have employed various techniques to measure transport and have been conducted in the laboratory and in the field, as summarized in Table 2-1. Most laboratory studies that used qualitative methods (visual analysis of the two time series) found a correspondence between the wind and saltation. The field-based experiments showed disagreement using both qualitative and quantitative analysis methods. The consistency in the laboratory results may be because of the ability to control the conditions in the laboratory especially vis-à-vis steady wind velocity. Alternatively, the consistency in the laboratory results may be because the qualitative methods are not held to any statistical standards. Additionally, Spies and McEwan (2000) indicated that wind tunnels do not allow for realistic gust development because eddies are small compared to grain size.

A subset of the studies presented in Table 2-1 calculated correlation coefficients to relate wind velocity to saltation intensity (Table 2-2). Sterk et al. (2002), Namikas (2002), and Leenders et al. (2005) found that their statistics improved when employing longer time averaging lengths.

Several have measured the turbulent directional components (i.e., horizontal and vertical to the bed (c.f., Fig. 2-3)) in the wind field. The directional components can be measured with hot film or sonic anemometers and the resultant time series can be analyzed using quadrant decomposition (§2.5) or to determine which component of the velocity field is most correlated with the saltation field. Sterk et al. (2002), Schönfeldt and von Löwis (2003), and Leenders et al. (2005) concluded that the *u'* (horizontal) component was most highly correlated to saltation.

One deficiency with such studies is that none measure wind velocity and saltation with precisely and tightly controlled time and space synchronization. Wiggs et al. (2004) acknowledge that the discrepancies in their data are partially because the distance between their measuring devises are located too far apart, at approximately one meter. Baas (2003) and Baas and Sherman (2005) (papers based on the same field experiment) placed their saltation sensor (*Safires*) at 0.04 m above the bed, 0.10 m away from the hot film anemometer. Bauer et al. (1998: 353) deployed cup and hot film anemometer towers and tipping bucket sediment traps “within one meter” of each other (c.f., Bauer and Namikas, 1998 for details on sediment trap). Several authors (Jackson and McClosky, 1997; Sterk et al., 2002; and Davidson-Arnott et al. (2003) did not report the horizontal distances between their wind and sand measuring devises. It should be noted that previous studies (shown in Table 2-2) focused on establishing an overall linear dependency between the wind and sand records. However, none of these studies were able to discern individual wind or saltation events, nor were able to correlate these events.

Table 2-1. Summary of investigations (presented in chronological order) that attempted to establish a relationship between unsteadiness of the wind and sand fields. Summary statements from the authors were used to determine if there was a linkage between wind and sand (column 4). If there is a "N/A" in the fourth column, the author(s) made no comment.

Author (year)	**Study Location**	**Analysis Methods**	**Linkage between Wind & Sand Established?**	**Comments**
Lee (1987)	Field	Quantitative	Yes	Correlation coefficients
Jackson and McCloskey (1997)	Field	Quantitative/ Qualitative	Yes	Auto correlation, cross correlation, 2nd order polynomial r^2, visual matching
Butterfield (1991)	Field	Qualitative	No	Visual, time series matching (their Fig. 13)
Butterfield (1991)	Lab	Qualitative	Yes	Unsteady wind conditions, visual time series comparison (their Fig. 10)
Butterfield (1993)	Lab	Qualitative	Yes	Visual, time series matching (their Fig. 13.8)
Stout and Zobeck (1997)	Field	Quantitative		Intermittency function
Bauer et al. (1998)	Field	Quantitative	No	VITA
Butterfield (1998)	Lab	Qualitative	N/A	Fig. 6 shows sand lagging wind by 0.3 phase (wind was generated in sinuous motion)
Sterk et al. (1998)	Field	Quantitative	N/A	Correlation coefficients
Namikas (2002)	Field	Quantitative	Yes/No	Correlation coefficients (Yes for longer time averaging, entire run and 15 s blocks; No for 1 Hz data)
Sterk et al. (2002)	Field	Quantitative	N/A	Correlation coefficients
Davidson-Arnott et al. (2003)	Field	Qualitative	Yes/No	Yes at lower beach (their Fig. 6A); No at foredune top (their Fig. 6C)
Davidson-Arnott et al. (2003)	Field	Quantitative	No	Intermittency function
Schönfeldt and von Löwis (2003)	Field	Quantitative	Yes	Spavelet (their Fig. 6)
Wiggs et al. (2004)	Field	Quantitative	N/A	Time fraction equivalence method
Baas and Sherman (2005)	Field	Quantitative	Yes	VITA and covariance
Leenders et al. (2005)	Field	Quantitative	No	Correlation coefficients
Baas (2006)	Field	Quantitative	Yes	Spavelet, cross-correlation (of wavelet coefficients)
Davidson-Arnott and Bauer (2006)	Field	Quantitative	N/A	Correlation coefficients

Table 2-2. Summary of investigations that attempted to establish a relationship between unsteadiness the wind and sand fields using regression analysis. Linear regression analysis was used, unless noted otherwise.

Author (year)	**Correlation Coefficients**	**Comments**
Lee (1987)	0.68	
Jackson and McCloskey (1997)	0.90	Study 1: 2nd order polynomial
	0.94	Study 2: 2nd order polynomial
Sterk et al. (1998)	0.65	Storm 1
	0.57	Storm 2
Namikas (2002)	0.088	1 Hz, u_*^3 anemometer data (his Fig. 6E)
	0.464	1 Hz, u_*^3 drag plate data (his Fig. 6F)
Sterk et al. (2002)	0.54	Only periods with saltation were considered
	0.51	Only periods with saltation were considered
Schönfeldt and von Löwis (2003)	0.67	
Leenders et al. (2005)	0.62	4 Hz sample rate, horizontal wind velocity component; 3 June 2002 study
Leenders et al. (2005)	0.45	4 Hz sample rate, horizontal wind velocity component; 16 May 2003 study
Davidson-Arnott and Bauer (2006)	<0.05-0.40	1 Hz sample rate, only periods with saltation were considered

2.5 Event Detection

To be designated as an event, the magnitude (size) and duration (length) must exceed thresholds defined by the user or by the event detection method. An optimal method is one that can identify and select events from the background signal without selecting false events and without requiring extensive subjective decision-making/training from the user.

There are several analytical methods to detect and describe coherent structures in turbulent flows (most reviewed in Sullivan et al., 1996): for example, proper orthogonal decomposition, linear stochastic estimation, Gram-Charlier estimation, continuous and discrete wavelet transforms (Farge, 1992), quadrant decomposition (Krogstad and Skåre, 1995), and variable interval time averaging (VITA). All the aforementioned methods, with exception of VITA and wavelet require simultaneous, multiple point (i.e., multi-dimensional) measurements of the flow, usually at sampling frequencies faster than 10 Hz. The following discussion will focus on VITA and the continuous wavelet transform because these are the methods that have been most frequently used in the past (VITA) or that will be used herein (wavelet).

2.5.1 Variable Interval Time Averaging (VITA) Method

The variable interval time averaging (VITA) method is used to detect anomalies in time series of a particular variable, usually flow velocity. Anomalies, termed 'events,' are rapid departures from the local mean conditions. The VITA method was developed by Blackwelder and Kaplan (1976) as a means of detecting turbulent events and has frequently been employed to detect such events in water and air (e.g., Narahimha and Kailas, 1990; Bauer et al., 1998). The VITA method requires a continuous time series and is a type of bandpass filter that removes short duration and small magnitude events (Johansson and Alfredsson, 1982). The user determines an appropriate averaging time and threshold to distinguish an event from background 'noise.' Given a fluctuating wind speed (*u*) over time (*t*):

$$\langle u(t,T)\rangle = \frac{1}{T}\int_{t-T/2}^{t+T/2} u(s)ds \tag{2-11}$$

where *T* is the averaging period, *s* is the integration period, and $\langle \ \rangle$ indicates a variable-interval time average. As *T* approaches the total record length (T_r), VITA approaches the record average ($\bar{u}$):

$$\lim_{T\to T_r}\langle u(t,T)\rangle = \frac{1}{T_r}\int_{0}^{T_r} u(s)ds = \bar{u} \tag{2-12}$$

An instantaneous variance (VAR) of the fluctuating quantity (*u*) over an averaging period (*T*) can be calculated for every sample in the time series using:

$$\langle VAR(t,T)\rangle = \frac{1}{T}\int_{t-T/2}^{t+T/2} [u(s)-\bar{u}_T]^2 ds \tag{2-13}$$

The result is a filtered time series with discrete peaks indicating events. A threshold (*k*) must be assigned to determine if the peaks are VITA events:

$$\langle VAR(t,T)\rangle > k(VAR) \tag{2-14}$$

The last step of VITA is the use of a detection function *D(t)*:

$$D(t) = \begin{cases} 1 & if \quad \langle VAR(t,T)\rangle > k(VAR) \\ 0 & if \quad otherwise \end{cases} \tag{2-15}$$

that assigns a value of unity to a VITA event and zero otherwise. As *k* increases, the number of VITA events decreases.

A range of values has been used for *k*, and the choice is somewhat subjective. Johnasson and Alfredsson (1982) in a literature review, found a range of 0.2 to 1.6. Bauer et al. (1998) used 1.1, and Baas (2003) used 0.4. The number of VITA event also depends on *T*. Blackwelder and

Kaplan (1976) suggest a *T* based on dimensionless time. Bauer et al. (1998) and Baas (2003), employed 4 s and 2.5 s time averages, respectively. Some have adopted quantitative assignments of *k* and *T*. For example, Bogard and Teiderman (1986) suggest k = VAR/σ^2. Blackwelder and Kaplan (1976) applied VITA to wind speed measurements to detect burst-sweep events.

Bauer et al. (1998) and Baas (2003) used VITA analysis in an attempt to correlate wind and sand transport events. Bauer et al. (1998) concluded that VITA-selected wind events do not correlate with sediment transport fluctuations. In this experiment, anemometers measured wind speed at 1 Hz and a tipping-bucket sand trap (see Bauer and Namikas, 1998), located approximately 1 m away, sampled at 1 Hz and measured sediment transport fluctuations. Bauer et al. (1998) concluded by indicating that the uncertainties of their results might be solved with high frequency measurements of wind and sediment flux. Baas (2003) employed the VITA method on anemometer time series and found correlations with measurements from saltation sensors (Safires) located 0.1 m downstream.

A suite of criticisms about the VITA method have been noted. The subjectivity when assigning *k* and *T* is a major limitation of the method (Sullivan et al., 1994), and may result in under- or over-estimation of the number and timing of VITA events (Bauer et al., 1998). Bogard and Tiederman (1986) indicated that the VITA method can detect turbulent events in a wind time series. However, they pointed out that VITA is prone to false detections if a high threshold (*k*) is not selected. The VITA method is unable to determine the duration of an event. Johansson and Alfredsson (1982) indicated that the relationship between the frequency of event occurrence and the dependence on the threshold selection is exponential. Visual identification was deemed superior to VITA analysis in identifying structures in the wind field by Antonia et al. (1986). The VITA method will not be employed in this research because of the high level of subjectivity when selecting *k* and *T* (and the subsequent impact on event selection). Alternatively, a more quantitative-based method will be employed to select events in the wind and sand events.

2.5.2 Continuous Wavelet Transform

Wavelet analysis, introduced by Grossmann and Morlet (1984), is a method used frequently throughout geosciences (c.f., Kumar and Fourfoula-Georgiou, 1997). The wavelet method has been used to detect the influence of tides on a stream gauge (Lim and Lye, 2004), to characterize snowmelt in Antarctica using satellite imagery (Liu et al., 2005), to detect patterns in field and simulated forests (Mi et al., 2005), and to detect freak or breaking waves in the ocean (Mori et al., 2002 and Liu and Babanin, 2004, respectively). Farge (1992), however, is recognized as the first to introduce wavelet as a method to detect turbulent events in time series. Several others have since followed and have employed wavelet analysis as a means to detect coherent motions (Liandrat and Moret-Bailly, 1990; Gamage and Hagelberg, 1993; Terradellas et al., 2001).

Wavelet analysis simultaneously decomposes data into the scale (frequency) and time domain and therefore can be employed to detect individual coherent structures (in the wind field) occurring at characteristic scales at certain times. Wavelet energy corresponds to variations in the original signal at a given scale and position (i.e., location in the time series). If the original signal does not fluctuate at a given scale and position, the corresponding wavelet energy is zero (Farge, 1992). Advantages to the wavelet method over other analysis methods (in particular VITA), include that the input data do not have to be stationary and that wavelet analysis provides time and scale information, allowing the user to ascertain not only the location of the events, but also the scale/duration. Also, there is no subjective threshold required.

Torrence and Compo (1998: 61) indicated that wavelet maps (results of wavelet analysis) are subject to quantitative interpretation: “The wavelet transform has been regarded by many as an interesting diversion that produces colorful pictures, yet purely qualitative results.” However, Torrence and Compo (1998) introduced a method to designate regions in a wavelet map that are statistically significant at the 5% level (or the 95% confidence interval). Their methods have been employed by others to detect turbulent bursting in the nocturnal atmospheric boundary layer (Salmond, 2005) and to determine ecological patterns using simulated data and field data from a Beijing forest (Mi et al., 2005).

The following reviews basic concepts to wavelet analysis, especially those portions relevant to this research. More detailed descriptions may be found in Farge (1992), Meyers et al. (1993), and Hubbard (1998).

The wavelet transform is a mathematical technique that convolves a time series (x_b) with a wavelet base (§2.5.2.1) $\psi_0(\eta)$ at each point (b) for each scale (a):

$$W_b(a) = \sum_{b'=0}^{N-1} x_{b'} \, \psi^* \left[\frac{(b' - b)\delta t}{a} \right] \tag{2-16}$$

where (*) indicates the complex conjugate, N is the number of points in the time series, and δt is the time step. The values a and b are the wavelet coefficients where a is the dilation function (or width of the wavelet scale) and b is the time lag or translation parameter. In the continuous wavelet transform (rather than its counterpart, discrete wavelet transform), scale and time are continuously shifted. The continuous wavelet transform is considered superior to the discrete for extracting features in a time series, whereas the latter is more appropriate for noise reduction and data compression (Grinsted et al., 2004).

2.5.2.1 Wavelet Base

Selecting the wavelet base, or mother wavelet, is the most subjective portion of wavelet analysis. The Morlet and Mexican hat wavelets are selected here for further discussion because these two have been employed in research similar to this work (e.g., Salmond, 2005; Baas, 2006). Other wave bases, such as Daubechies, Haar, and Meyer, are detailed in Farge (1992), Wojtaszczyk (1997), and Hubbard (1998).

The Morlet wave base, shown in Fig. 2-7 is non-orthogonal, complex, and symmetrical. It is efficient at defining the initiation and termination of the changes in background conditions (Hagelberg and Gamage, 1994) and has effectively been used to characterize the durations of coherent structures (Thomas and Foken, 2005). Several others have used the Morlet wavelet, to discern intermittent periods in the nocturnal boundary layer (Salmond, 2005) and to find periods of turbulence in the atmospheric boundary layer (Terradellas et al., 2001), for example. The equivalent Fourier period for the Morlet wavelet is equal to the wavelet scale multiplied by 1.033. The equation for the Morlet wave base is:

$$\psi_0(\eta) = \pi^{-1/4} e^{i\omega_0\eta} e^{-\eta^2/2} \qquad (2\text{-}17)$$

where ω_0 is non-dimensional frequency and η is a non-dimensional time parameter.

The Mexican hat wave base (Fig. 2-7) is the normalized second-order of a Gaussian and is non-orthogonal, simple, and symmetrical. The equivalent Fourier period for the Mexican hat is equal to the wavelet scale multiplied by 3.97, therefore, the Morlet wavelet is superior for discerning features at smaller scales. Collineau and Brunet (1993: 377) concluded that the Mexican hat was “suitable” for counting “significant” events, however, their research did not consider the Morlet wavelet base (because it was a complex wavelet) and they were detecting events with periods of 100 seconds. Mallat and Zhong (1992) and Liu et al. (2005) have successfully used Mexican hat wavelet for edge detection. The equation for the Mexican hat wave base is:

$$\psi(\eta) = \frac{-1^3}{\sqrt{\Gamma(2.5)}} \frac{d^2}{d\eta^2}\left(e^{-\eta^2/2}\right) \qquad (2\text{-}18)$$

where Γ is the gamma function and η is a non-dimensional time parameter.

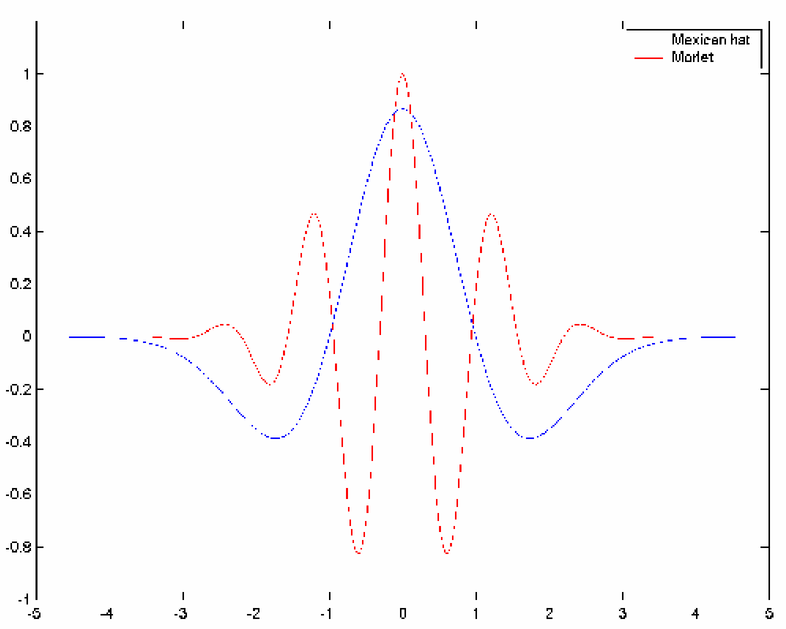

Fig. 2-7. The Mexican hat (blue) and the real portions of the Morlet (red) wave bases.

2.5.2.2 Wavelet Analysis in Aeolian Research

Wavelet analysis has been used in aeolian investigations by Schönfeldt and von Löwis (2003) and Baas (2006). Schönfeldt and von Löwis (2003) used the Haar wavelet base in a discrete wavelet transform of their horizontal and vertical (relative to the bed) wind measurements obtained from a Saltiphone deployed 0.10 m above the bed (c.f., Spaan and van den Abeele (1990) for details on the Saltiphone). Baas (2006) selected the Mexican hat to correlate boundary layer turbulence to aeolian transport measured with a *Safire* deployed 0.04 m above the bed (c.f., Baas (2004) for details on the *Safire*). Neither study analyzed the wavelet maps, rather they focused on spectral analysis of the wavelet coefficients, or “spavelet” (c.f., Petenko, 2001). Baas (2006) calculated that the peak spectral wavelet energies for wind and saltation were 60 s and 6-7 s., respectively. The wind and saltation records of Schönfeldt and von Löwis (2003) corresponded with the -5/3 Kolmogorov slope (Kolmogorov, 1941), while only the high frequency portions of the saltation spavelet curves calculated by Baas (2006) matched this slope.

2.5.3 Cross Continuous Wavelet Transform

Continuous wavelet transform provides a powerful data analysis tool for event detection in an individual time series, for example wind and sand records. However, events are only discernable for each time series. Grinsted et al. (2004) discussed the methods for a cross wavelet transform that allows for two time series to undergo continuous wavelet transform simultaneously. In this research, power wavelet coefficients from the thermal anemometer (W_{b_1}) and miniphone (W_{b_2}), calculated using Eq. 2-16, are used to calculate cross wavelet coefficients using the following:

$$W_{b_{12}} = W_{b_1} W_{b_2}{}^{*} \tag{2-19}$$

where (*) is the complex conjugate (c.f., Grinsted et al., 2004 for details on cross wavelet). Regions that are statistically significant at the 95% confidence interval can be identified.

3. STUDY SITE AND FIELD METHODS

3.1 Section Introduction

Section 3 begins with a description of the study site near Shoalhaven Heads, New South Wales, Australia. The instrument system and data collection are described, including the weather conditions on the day of data collection. The thermal anemometers and the saltation sensors, or “miniphones” are introduced. The dimensions and location of the hose-style sand traps described. Lastly, the two instrument configurations are presented.

3.2 Study Site Location

Sediment transport and wind data were collected 4 August 2004 on an un-named beach (34.5140° S, 150.4456° W) south of Seven Mile beach and north of Comerong beach, at the end of the Shoalhaven River near Shoalhaven Heads, New South Wales, Australia. This field site was selected because of the open, relatively flat topography and relatively small sand grain size. Also at this location wind could blow from a range of approximately 270° with a long enough fetch to transport sand and develop a boundary layer with a thickness in excess of one meter. Vehicles were allowed on this beach, also making this a logistically attractive field site. Fig. 3-1 shows the approximate location, of the study site and Figs. 3-2 and 3-3 are oblique images of the site. On 4 August 2004, the average temperature was 11.0°C, the average relative humidity was 53%, and the average wind speed was 25.4 km/hr at the Nowra meteorology station (site number 68072 at 34.9469º S 150.5353º W, Australian Government Bureau of Meteorology). On the previous day (3 August 2004) at the Nowra weather station, 0.6 mm of precipitation was measured between 13:05 and 13:19. No precipitation was reported at Nowra on 4 August 2004. Short (1983) and Wright (1970) provide details about the geomorphic history of Seven Mile and Comerong beaches.

Fig. 3-1. Field site location, between Seven Mile and Comerong beaches near Shoalhaven Heads, New South Wales, Australia. The black star indicates the location where the instruments were deployed. Wind was from the west during data collection (http://earth.google.com).

Fig. 3-2. Oblique photograph of the field site looking west from the location of the instruments toward the Shoalhaven River.

Fig. 3-3. Oblique photograph of field site looking north toward Seven Mile Beach.

3.3 Instrumentation

3.3.1 Thermal Anemometers

Custom, ruggedized thermal anemometers with a frequency response of 5 Hz were constructed by Dantec Dynamics (www.dantecdynamics.com) specifically for this field project. These sensors are similar to the Dantec Dynamics probes used by Butterfield (1999a) in his laboratory experiments. The probe is a stainless steel tube with sensors on the end and is designed to withstand intense sandblasting, but not moisture (e.g., direct raindrop impact) (Fig. 3-4). These thermal anemometers measure the *u'* wind velocity (c.f., Fig. 2-2). Previous studies (discussed in §2.4.3) that measured multiple components of the wind concluded that the *u'* velocity component was most correlated with the saltation field. Four thermal anemometers connect to one anemometer module (Fig. 3-4B) that is wired directly to the data acquisition system. The anemometer module requires 9-12 VDC (1 A) of power and outputs 0-5 VDC, a range that equates to approximately 0.2-30.0 m/s. The signal processing procedures are outlined in (§4.3.2).

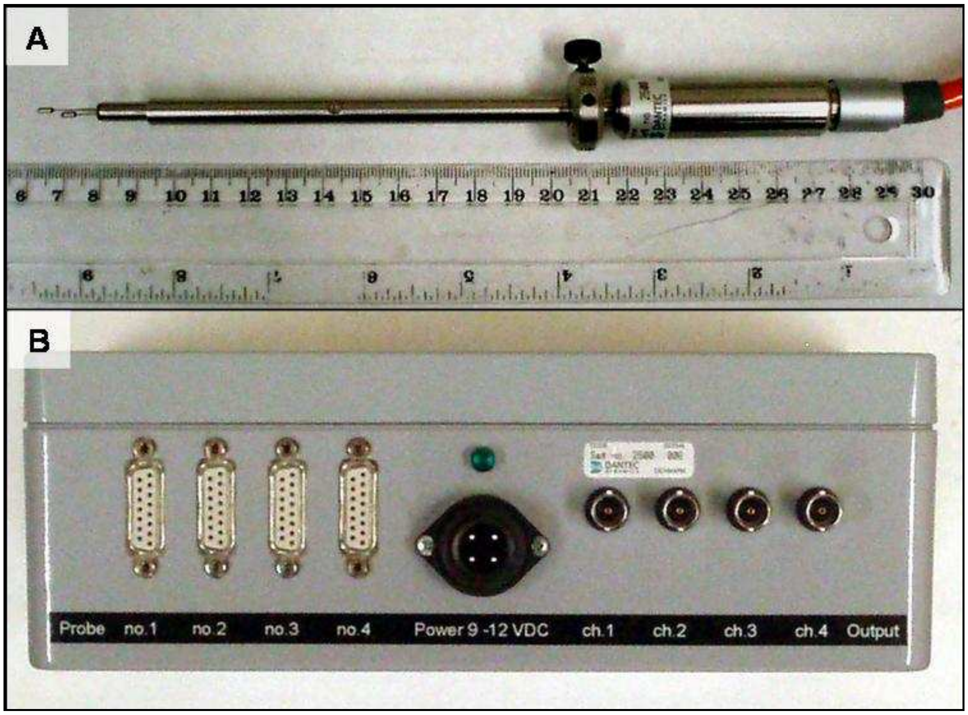

Fig. 3-4. Thermal anemometer sensor (A) and module (B) as manufactured by Dantec Dynamics. The probes that measure wind velocity (at ~7 cm on the ruler in (A)) are 8 mm (top) and 4 mm (bottom) and their diameter is approximately 2 mm. The diameter of the instrument (between ~22-27 cm on ruler) is 0.05 m.

3.3.2 Saltation Sensors

Microphone-based saltation sensors, “miniphones” were designed and constructed to detect discrete sand grain impacts. Technical details of the miniphones can be found in Ellis (2006; also Appendix A). Two microphone sizes were used: 1) 9.4 mm diameter (69 mm^2 frontal area) microphone with a sensor diameter of 6.0 mm (28.27 mm^2 frontal area); and 2) a 6.0 mm diameter (28 mm^2 frontal area) microphone with a sensor diameter of 4.0 mm (12.56 mm^2 frontal area) (Fig. 3-5). Here, microphones will be distinguished according to their sensor area.

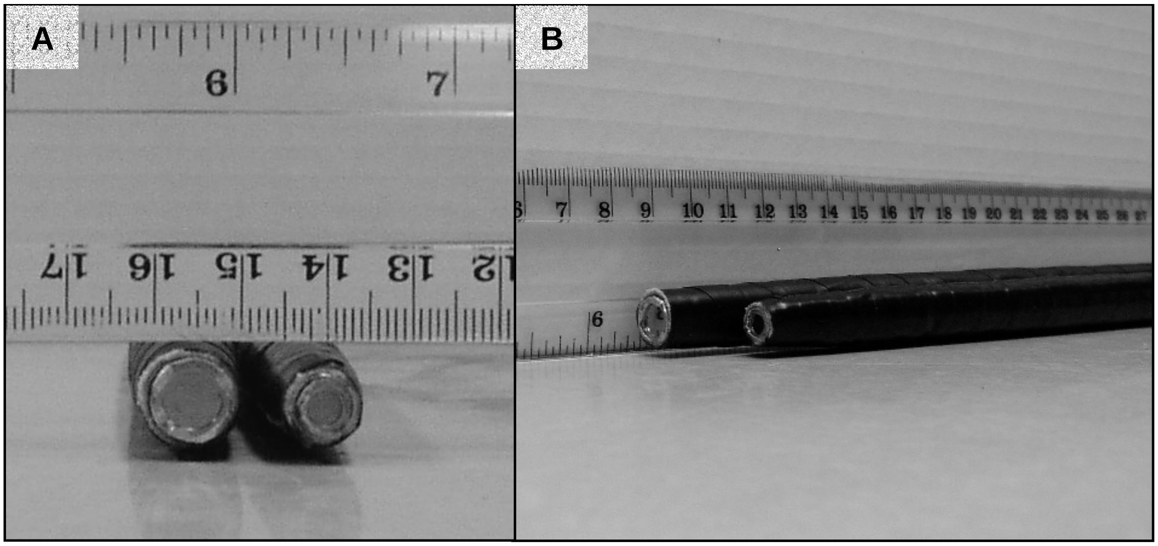

Fig. 3-5. Front (A) and side view (B) of miniphone. The 28.27 mm^2 miniphone is on the left and the 12.56 mm^2 is on the right in both panels.

3.4 Sand Traps

Hose-style sand traps (Fig. 3-6), similar to those described by Pease et al. (2002), were constructed to measure sediment transport rates and capture sand for grain size analysis. Grain sizes and sediment transport rates were used to calibrate the efficiency of the miniphones (c.f., Ellis, 2006; also Appendix A). The opening of the trap was 0.10 m high by 0.10 m wide and the downwind trap length was 0.20 m.

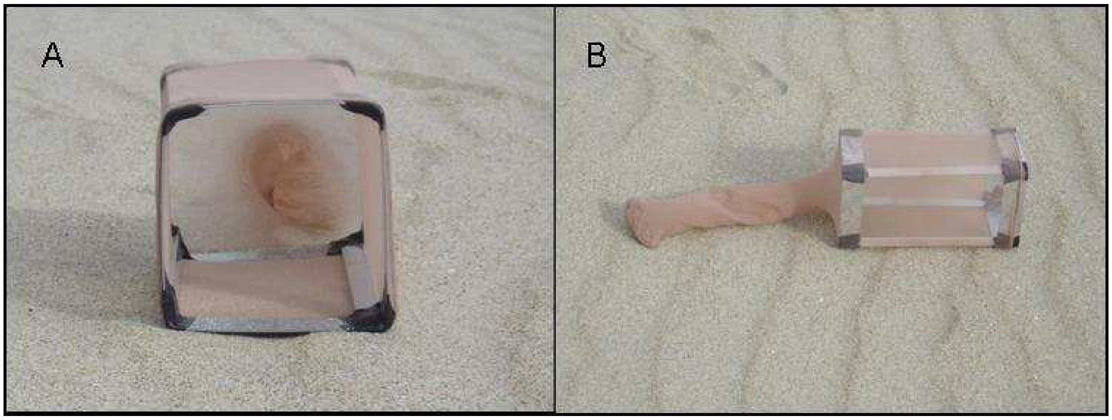

Fig. 3-6. Hose-style traps deployed during the field experiment. The exposed (A) dimensions are 0.10 m wide by 0.10 m high. The depth (B) of the trap is 0.20 m.

3.5 Instrument Deployment

This research was part of a larger field project, therefore, the deployment was more expansive than needed to accomplish the objectives of this study. The discussion below will focus only on the portions of the field deployment relevant for this research.

Two instrument configurations were used (A-B), and are shown in Fig. 3-7. Both configurations had one thermal anemometer and miniphone pair mounted on a tower. The miniphones and thermal anemometers were secured using wooden mounts (Fig. 3-8) and located 0.02 m apart (bed-parallel), on center. The instrument elevations are shown in Table 3-1. Sand traps were deployed during each data run. During Configuration A, the center of Trap 1 was located 0.20 meters from the center of the TA-MIC pair. Fig. 3-9 is a photograph taken during Configuration A and Fig. 3-10 shows a close-up of an instrument tower. During Configuration B, two traps were deployed, Trap 1, 0.20 m from the TA-MIC pair and Trap 2, 0.10 m from Trap 1.

Table 3-1 shows the instrument configuration and start time for the five data runs. The miniphones and thermal anemometers were monitored synchronously at 6000 Hz to optimize the multiplexing (speed) of the data acquisition system. The thermal anemometer and miniphone nomenclature that is maintained throughout the dissertation is also found in Table 3-1. This table also shows whether the 28.27 mm^2 or 12.56 mm^2 microphones were deployed.

Data were collected and stored using a National Instruments DAQ Card 6036E, connected to a Microsoft-based laptop (Intel Pentium M processor 15000 MHz, 512 MB RAM). During data acquisition, the laptop was powered by its internal battery, rather than a generator, to avoid introducing electronic noise into the system.

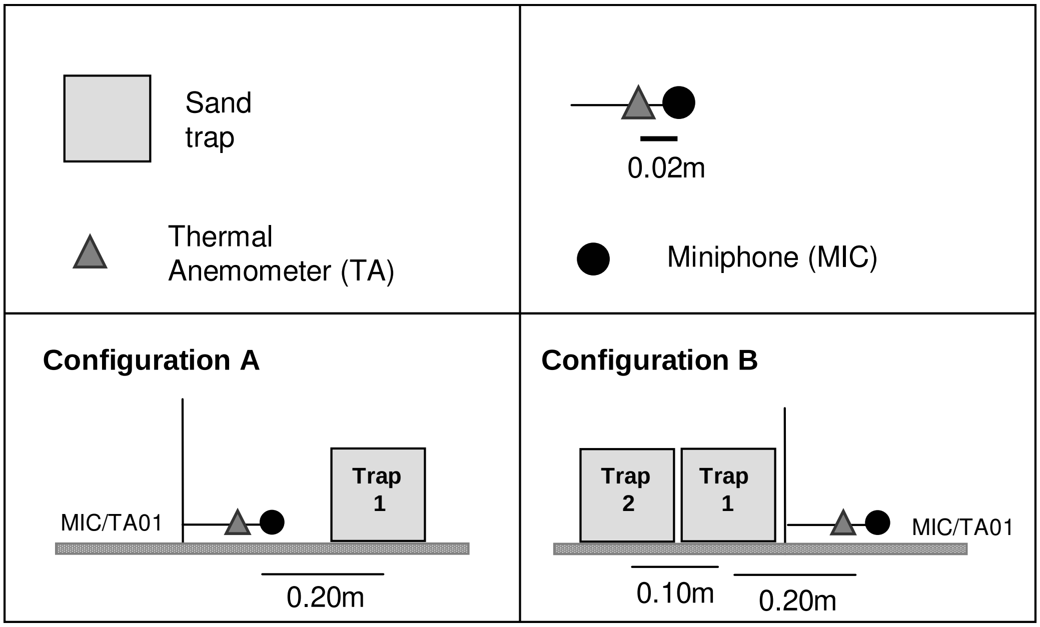

Fig. 3-7. Schematic showing the two (A, B) instrument configurations used during the field experiment. Instrument elevations for the thermal anemometer (TA) miniphones (MIC) are found in Table 3-1.

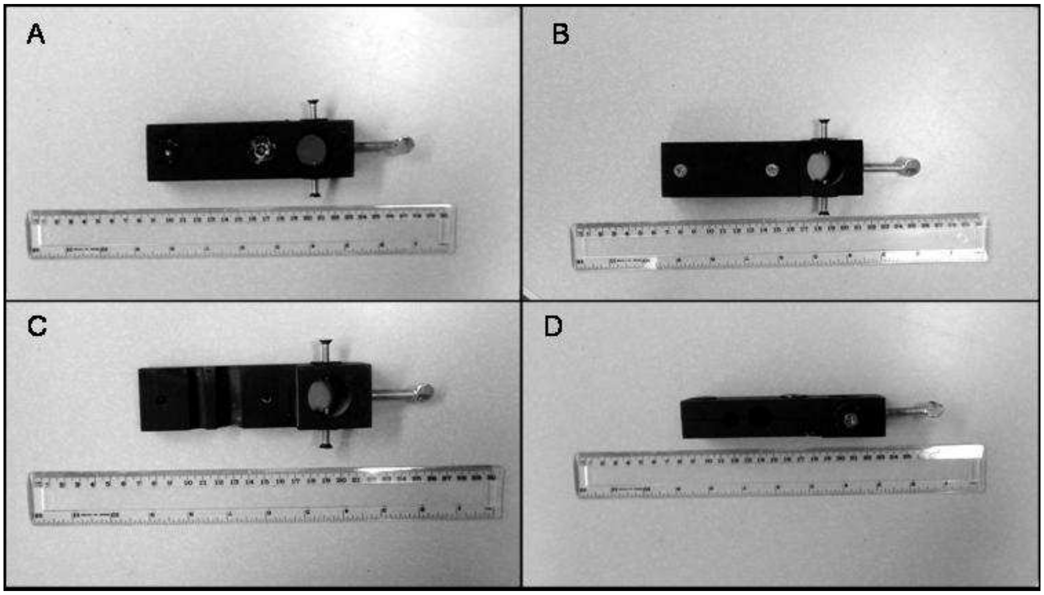

Fig. 3-8. Photographs of the wooden mounts used to secure the thermal anemometers and miniphones onto the instrument towers. (A) is a bottom view, (B) is a top view, (C) is a top view with the cover taken off to show the groves where the miniphone (left) and thermal anemometer (right) are placed, and (D) is the side that is exposed to the wind.

Table 3-1. Details for each data run, including the run start time, instrument elevations (shown under the run number), miniphone (MIC) sizes, and instrument configuration for the five data runs used in this research. The sample rate for the MIC and TA was 6000 Hz.

	Run Start Time	**Run Length (s)**	**MIC Size (mm^2)**	**Instrument Configuration**
Run 1	12:05	354		A
0.01 m			28.27	
Run 2	13:37	346		A
0.0225 m			12.56	
Run 3	14:13	670		A
0.02 m			12.56	
Run 4	15:03	1138		A
0.02 m			12.56	
Run 5	16:05	1218		B
0.02 m			12.56	

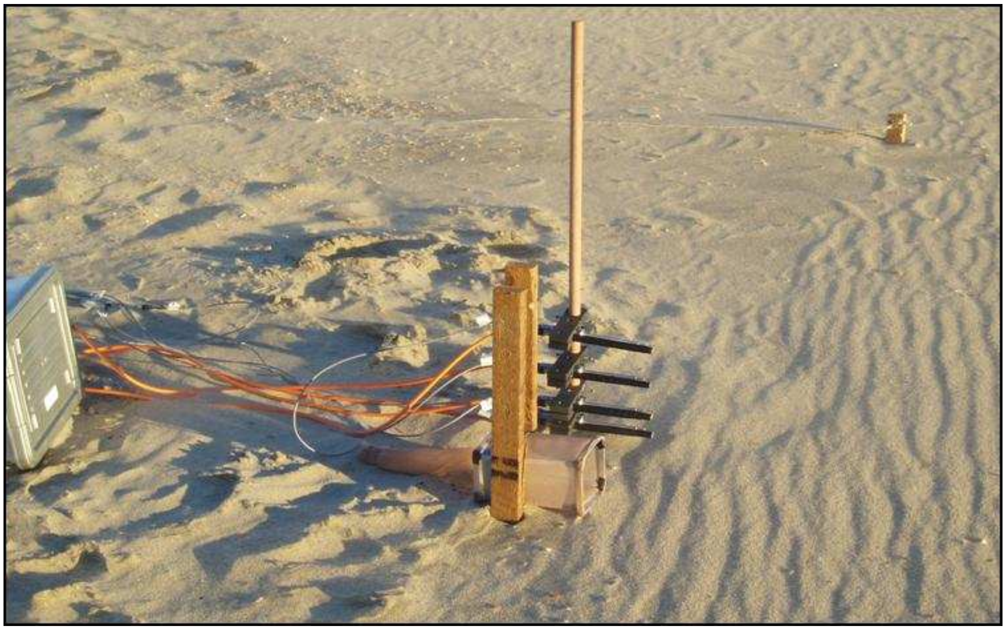

Fig. 3-9. Instruments deployed during a Configuration A run. The box shown on the left of the photograph is the anemometer module in a protective plastic case. Only the bottom TA-MIC pair is used in this research.

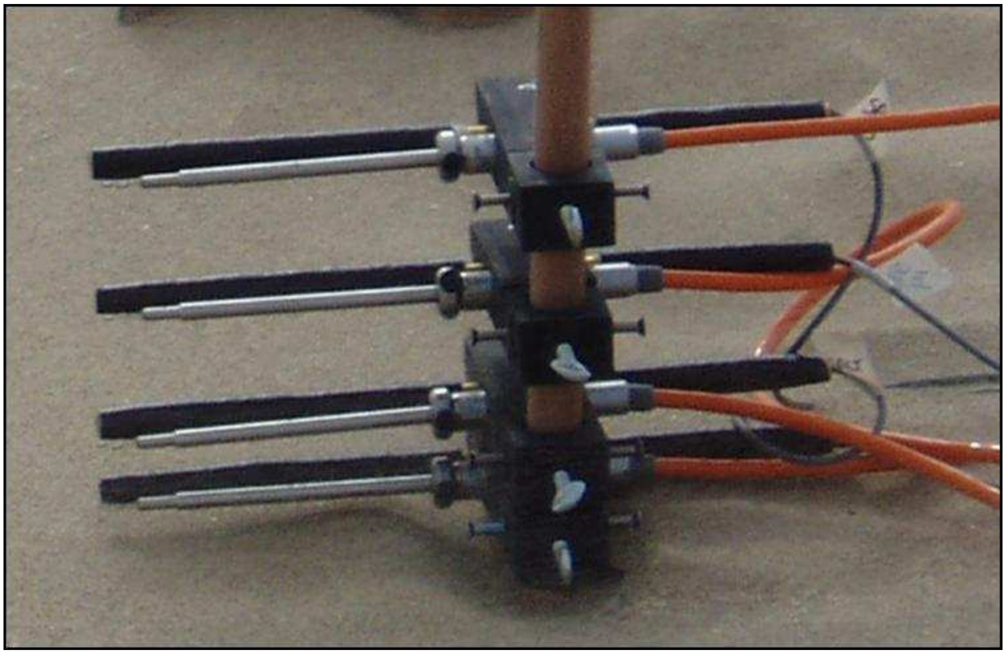

Fig. 3-10. Thermal anemometers (silver) and miniphones (black) mounted on an instrument tower at 0.02, 0.06, 0.12, and 0.20 m above the bed. A portion of a sand trap can be seen on the top of the photograph. This photograph was taken during a Configuration A run. Only the bottom TA-MIC pairs are used in this research.

4. DATA REDUCTION AND SIGNAL PROCESSING

4.1 Section Introduction

This section focuses on the process of reducing and analyzing the thermal anemometer and miniphone data. The statistical and visual methods for processing and reducing the miniphone data are discussed. The results of the thermal anemometer and miniphone calibrations are presented. The calibrated time series of the data used in this research are presented. A discussion of smoothing and detrending techniques and graphs showing the results follow. Finally, the grain size characteristics from the collected samples are presented.

4.2 Miniphone Data Reduction

The miniphones used in this study were designed to measure unsteadiness in the saltation field and were not designed to withstand long periods of intense saltation. It was observed during the field experiment that the surface of the miniphone melted. Fig. 4-1 shows the degradation of the miniphone surface after a ~1200 second deployment in the saltation layer. Intense saltation causes the miniphone diaphragm (the portion of the miniphone that senses the impacts; c.f., Ellis (2006); also Appendix A) to vibrate rapidly, increasing the temperature and eventually causing the surface to melt. Runs 4 and 5 were truncated where signal degradation was apparent and when the performance of the algorithm to select impacts diminished because the signal to noise ratio became too large (c.f., Ellis (2006); also Appendix A for algorithm details). Fig. 4-2 shows the entire raw miniphone time series from Run 4 that was truncated at 600 seconds as an example. The signal began to degrade from the beginning of the record, but is more apparent around 500 seconds. However, the performance of the algorithm did not degrade until after around 600 seconds (Note: If the standard deviation threshold (step 5) is increased, the algorithm is able to discern impacts with increased signal to noise ratios; however, it was determined here that the same threshold would always be used within one run). The co-located thermal anemometer (10-second averages) is plotted on Fig. 4-2 (red trace) to show that the decreasing average miniphone signal is not related to a decrease in the background noise (wind).

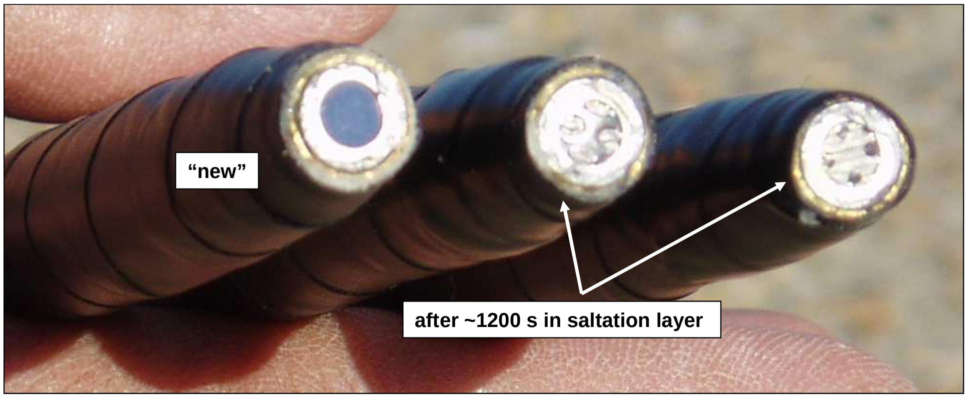

Fig. 4-1. Photograph of a miniphone before deployment (left) and two miniphones (middle and right) that were deployed in the saltation layer at 0.02 m above the bed for about 1200 seconds.

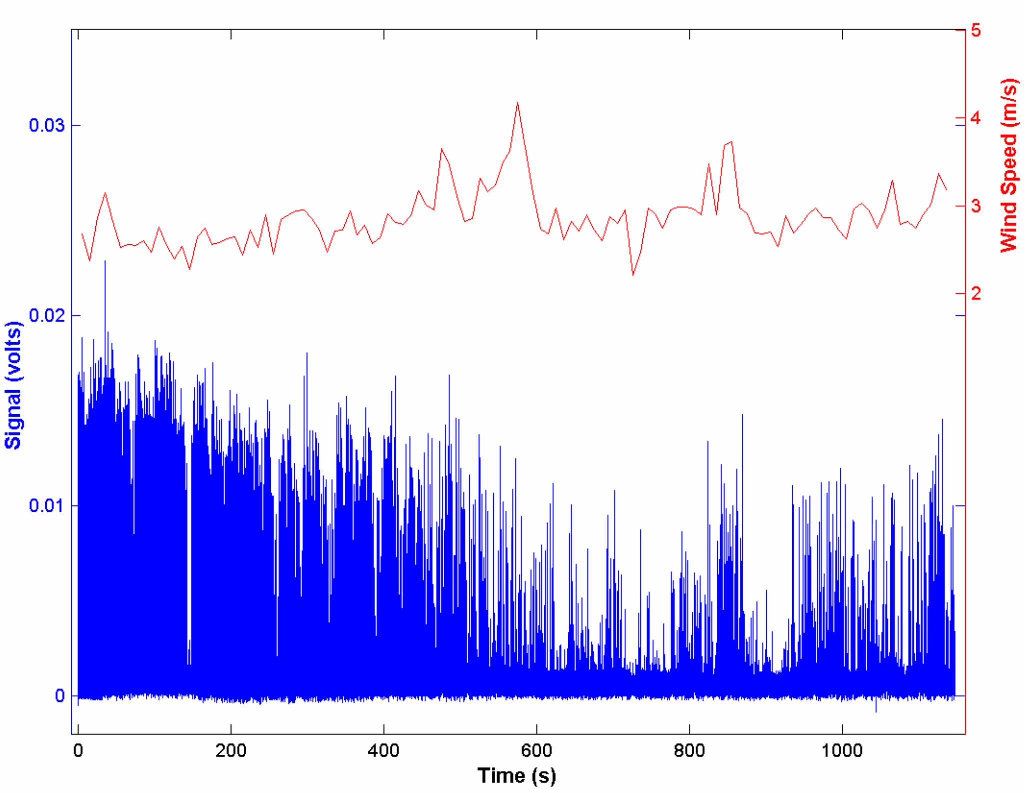

Fig. 4-2. Run 4 raw miniphone (left axis) and 10-second average of the thermal anemometer (right axis). Only 0-600 s was considered in this research.

In order to link saltation and wind events Sterk et al. (2002) and Davidson-Arnott and Bauer (2006) only considered portions of their saltation records where the saltation counts were either just greater than zero or were fairly intense. During Run 3, shown in Fig. 4-3, the latter portions of the record show little to no saltation (e.g., only a couple impacts between 550-600 s). This record was truncated at 450 seconds where the saltation intensity decreased and the signal to noise ratio increased (see discussion above). The time series from Runs 1 and 2 were not truncated.

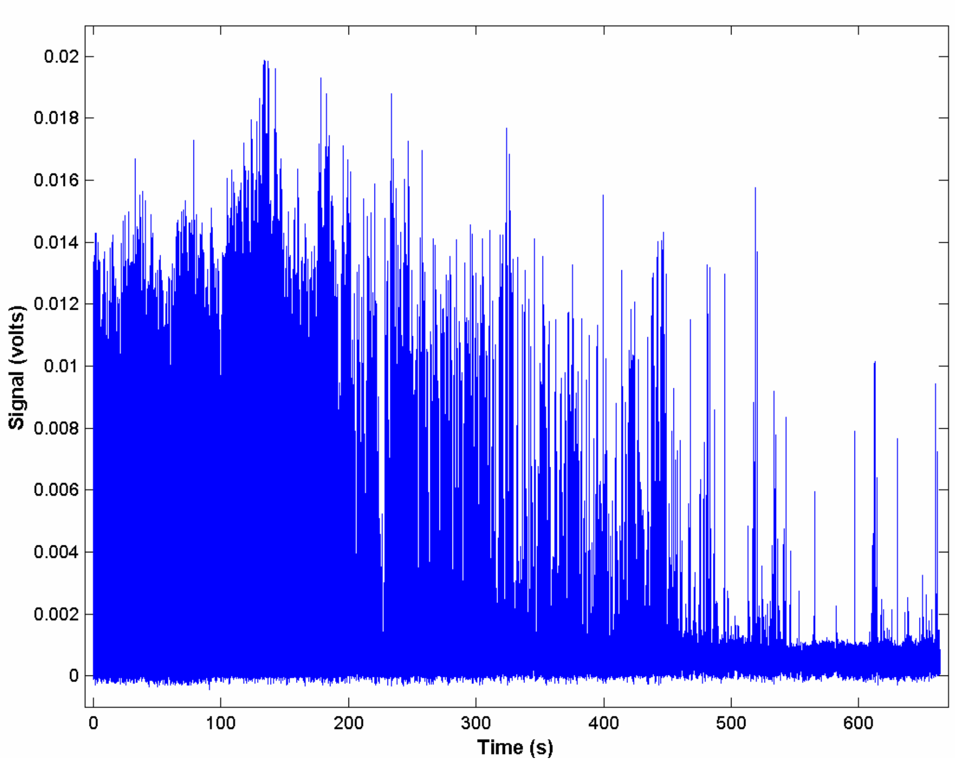

Fig. 4-3. Raw miniphone time series from Run 3. Only 0-450 seconds was considered in this research.

4.3 Signal Processing Methods

4.3.1 Miniphones

The miniphone, because it is microphone- (acoustic)-based, detects grain impacts and other background sound, such as wind. Because of the very different frequencies of the signal produced, it is possible to separate the grain impacts from the background noise. An algorithm was developed to isolate grain impacts from the "raw" miniphone signal. The resultant time series were reduced from 6000 Hz to 5 Hz by accumulating impact counts because the thermal anemometer response frequency was limited to 5 Hz and it is ideal for data processing to have both time series at the same sample rate. Details about these procedures are provided in Ellis (2006; also Appendix A).

4.3.2 Thermal Anemometers

Fig. 4-4 shows a 30 second example of an un-calibrated thermal anemometer time series, sampled at 6000 Hz. Each thermal anemometer was calibrated using the equations provided by Dantec Dynamics. Appendix B shows the MATLAB algorithm and the associated calibration coefficients. After calibration, thermal anemometer records were block averaged to a 5 Hz sample rate to correspond to the response time of the instrument (§3.3.1). The 5 Hz, calibrated version of Fig. 4-4 is shown in Fig. 4-5.

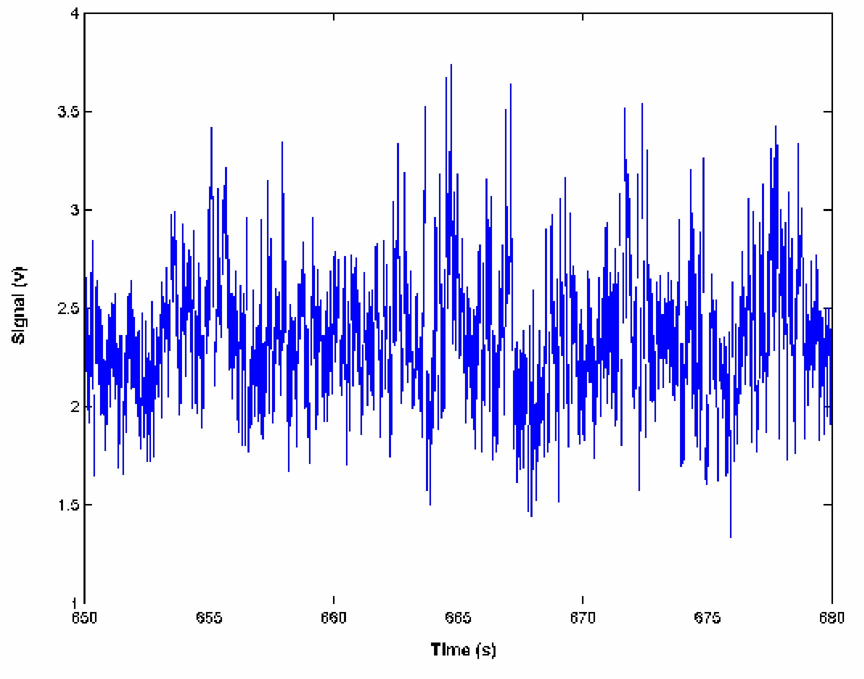

Fig. 4-4. Un-calibrated (6000 Hz) thermal anemometer time series.

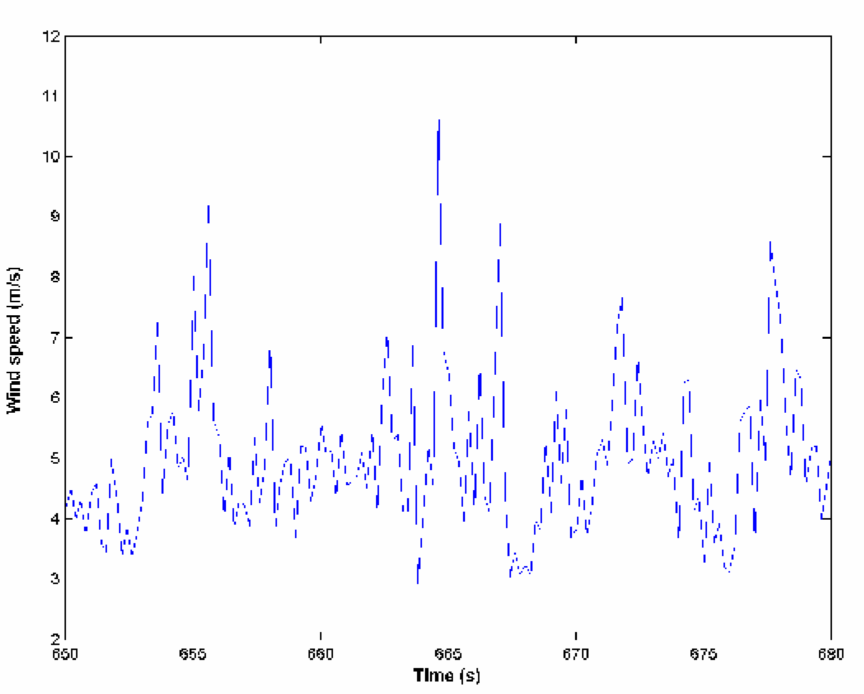

Fig. 4-5. Calibrated and block averaged (5 Hz) thermal anemometer time series.

4.4 Thermal Anemometer and Miniphone Time Series

The 5 Hz time series that will be used in this dissertation are presented in Figs. 4-6 to 4-10. The total number of saltation impacts for the microphones and the average wind speed measured by the thermal anemometers are presented in Table 4-1.

Table 4-1 indicates that higher average wind speeds do not always correspond with higher rates of grain impact. During Run 4, the lowest average wind speeds and the lowest impacts per second were measured. Run 2 had the highest transport rates, however, the average wind velocities were approximately 0.3 m/s slower than those measured during Run 3 (the run in which the highest average wind speeds were measured). The impact per second count during Run 1 cannot be directly compared to Runs 2-5 because a larger miniphone was deployed, thus explaining the large impact counts and low average wind speeds. However, the different miniphone sizes for Run 1 will not impact subsequent analysis because these tests compare relative transport intensities within the run, not between runs.

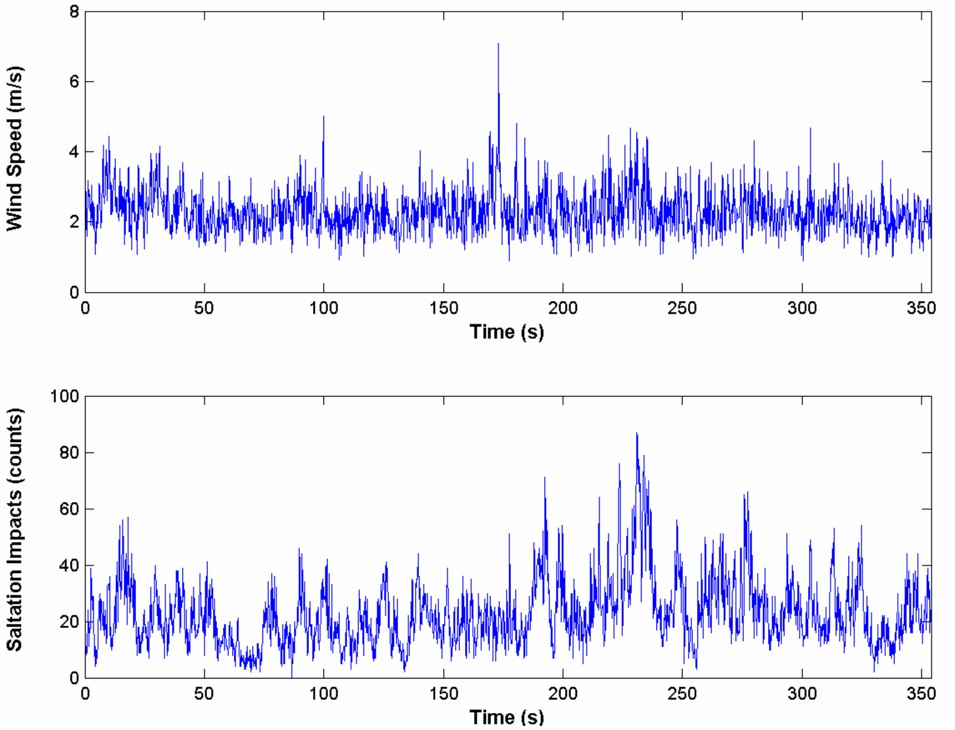

Fig. 4-6. Run 1 time series for the miniphone and the thermal anemometer tower.

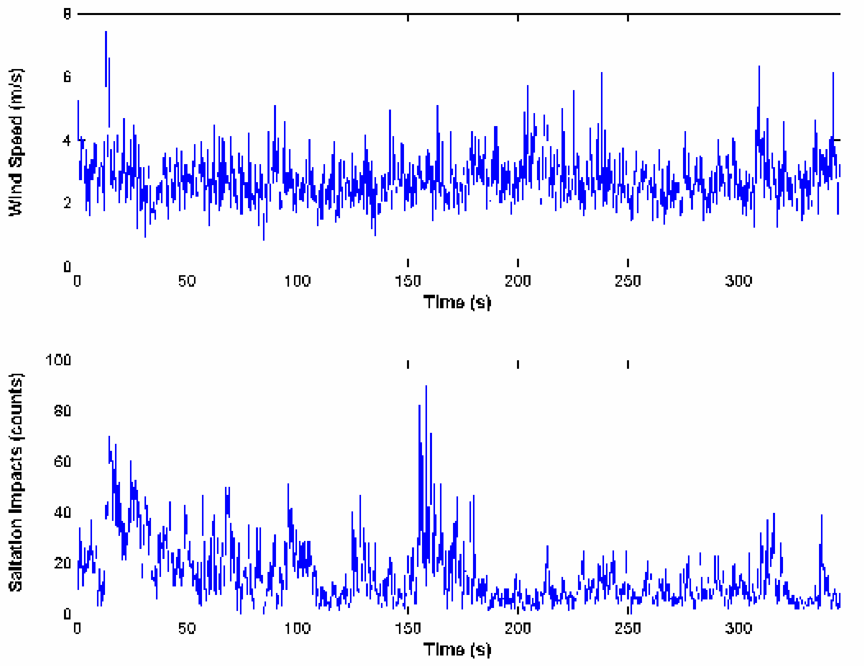

Fig. 4-7. Run 2 time series for the miniphone and the thermal anemometer tower.

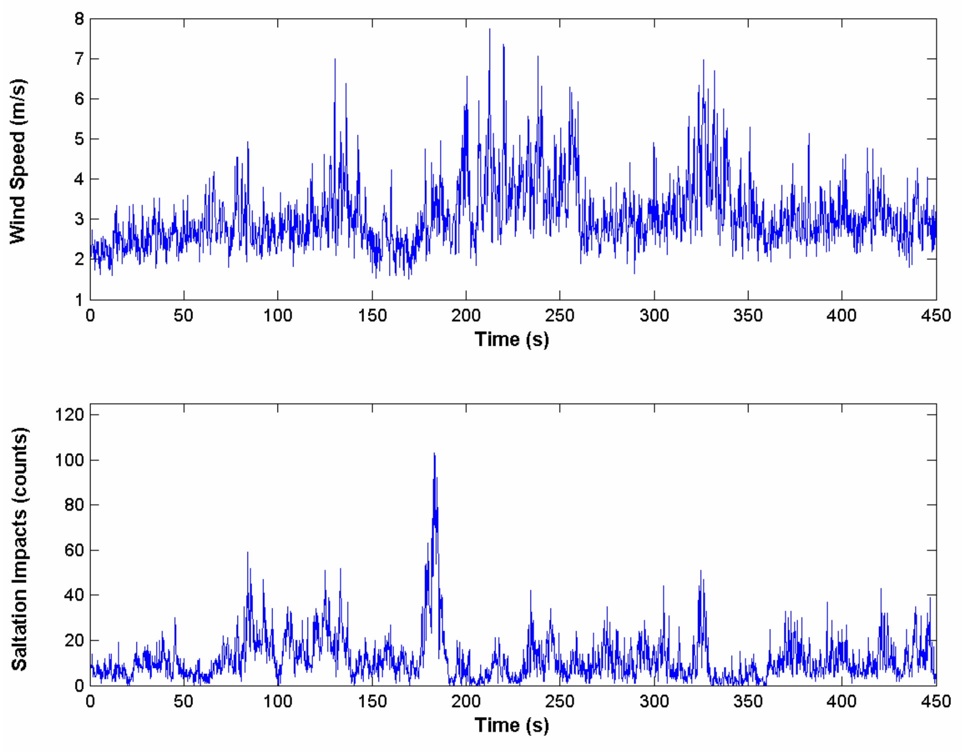

Fig. 4-8. Run 3 time series for the miniphone and the thermal anemometer tower.

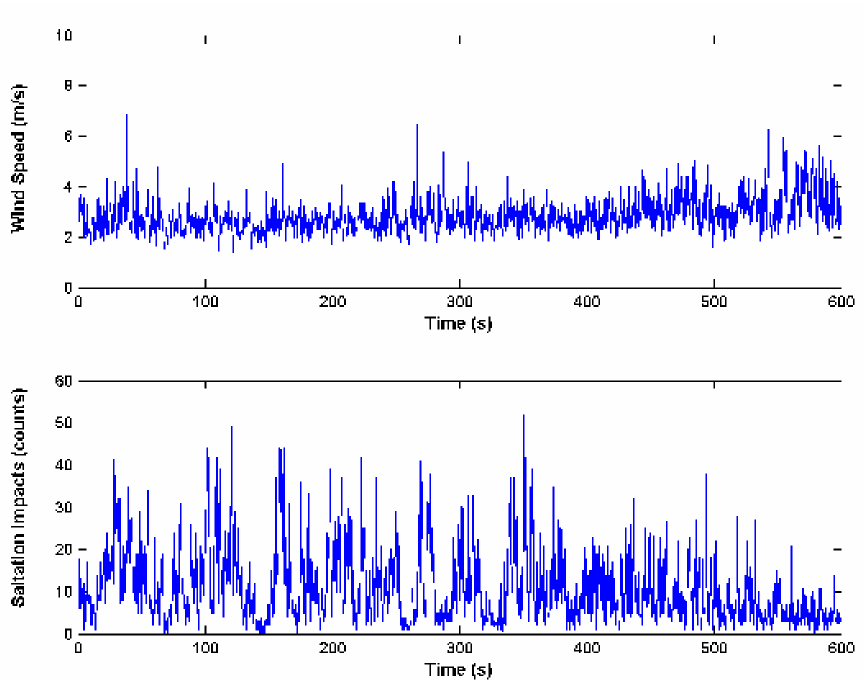

Fig. 4-9. Run 4 time series for the miniphone and the thermal anemometer tower.

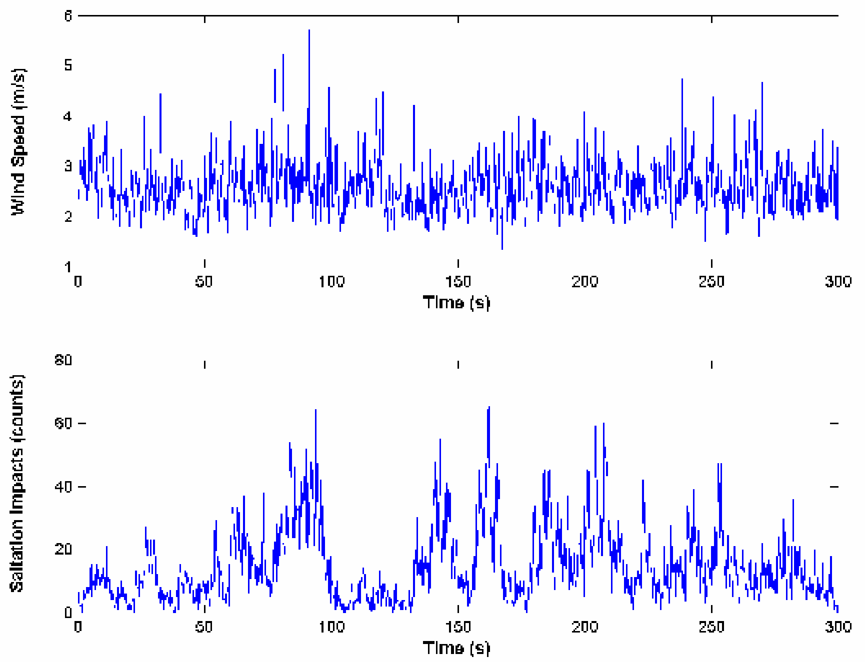

Fig. 4-10. Run 5 time series for the miniphone and the thermal anemometer tower.

Table 4-1. Summary data showing the total grain impacts for each run, average impact counts per second (impacts per second), and the average wind speed for each anemometer, and the miniphone size.

	Record Length (s)	**MIC Surface Area (mm^2)**	**Total Grain Impacts (counts)**	**Impacts Per Second**	**Average Wind Speed (m/s)**
Run 1 (0.01m)	354				
MIC		28.27	40540	114.52	
TA					2.29
Run 2 (0.0225m)	346				
MIC		12.56	26247	75.86	
TA					2.76
Run 3 (0.02m)	450				
MIC		12.56	26431	58.74	
TA					3.07
Run 4 (0.02m)	600				
MIC		12.56	33224	55.37	
TA					2.85
Run 5 (0.02m)	300				
MIC		12.56	22281	74.27	
TA					2.62

4.5 Smoothing and Trend Removal

The 5 Hz time series (presented in §4.4) were further processed to remove long-term trends found in the data (similar to a low-pass filter). The 5 Hz thermal anemometer and miniphone time series were detrended using linear regression and a third-order polynomial regression analysis. The residuals from the linear regression were saved and were used for the third-order polynomial regression analysis and the (new) residuals were saved. The equations and the percent variances removed during the detrending process are presented in Table 4-2. The detrended time series are shown in Figs. 4-11 to 4-15 where panel A shows the thermal anemometers and panel B show the miniphones. The variance removed (%), shown on Table 4-2, ranges from 0.10 to 49.08. These extremes are both found within the thermal anemometer records, Runs 5 and 1, respectively. The concern is that, for the runs where a high level of variance is removed (e.g., Run 1 TA, Run 2 MIC), that the time series is not dampened to the extent where potential events may be eliminated.

The 5 Hz time series (presented in §4.4) were also reduced to produce a 1 Hz time series. Davidson-Arnott and Bauer (2006) completed their regression analysis using 1 Hz data. At 1 Hz, visual comparison (qualitative analysis) is easier (compared to 5 Hz) because the higher frequency fluctuations are removed. Davidson-Arnott et al. (2003) also employed a 1 Hz sample rate for their qualitative analysis. To reduce the 5 Hz miniphone record to 1 Hz, the 5 Hz time series were accumulated. A corresponding thermal anemometer record was made by block averaging the 5 Hz time series to 1 Hz. The 1 Hz time series are shown in Figs. 4-11 to 4-15 where panel C show the thermal anemometers and panel D show the miniphones.

Table 4-2. Equations for the third order polynomial models and the resultant percent variance removed used to detrend the thermal anemometer and microphone time series.

	Equation for the Third-Order Polynomial Model	**Variance Removed (%)**
Thermal Anemometer		
Run 1	$y = 0.209213 - 0.00802163x + 0.0000605892x^2 - 1.1905x^3$	49.08
Run 2	$y = 0.383452 - 0.00985197x + 0.000056199x^2 - 8.90193x^3$	2.13
Run 3	$y = -0.491931 + 0.00536497x - 0.00000385546x^2 - 1.986x^3$	14.46
Run 4	$y = 0.285585 - 0.00825123x -0.0000024725x^2 + 3.17326E-9x^3$	13.12
Run 5	$y = 0.0584822 - 0.00202748x + 0.0000153366x^2 - 3.17717x^3$	0.10
Miniphone		
Run 1	$y = 7.53209 - 0.295053x + 0.00225205x^2 - 0.0000044525x^3$	13.74
Run 2	$y = 6.48155 -0.13044x + 0.000533282x^2 - 5.02535E-7x^3$	24.84
Run 3	$y = -9.28479 + 0.217699x - 0.00110923x^2 + 0.00000154411x^3$	7.76
Run 4	$y = -1.45711 + 0.0068195x + 0.000027367x^2 - 7.7099E-8x^3$	9.35
Run 5	$y = -6.21518 + 0.103192x - 0.000132859x^2 - 7.81906E-7x^3$	8.64

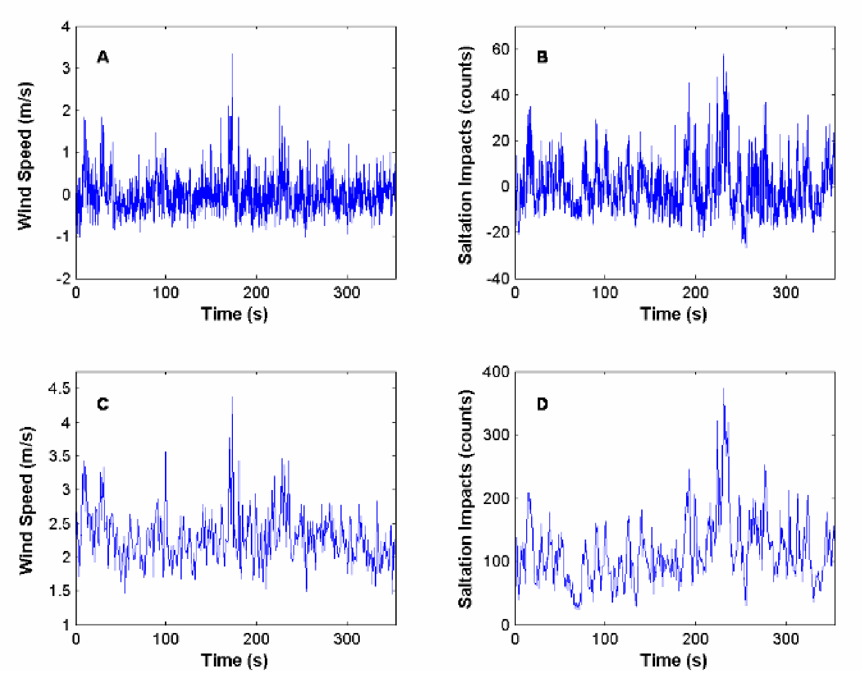

Fig. 4-11. Results from various smoothing and detrending techniques for the thermal anemometer (A and C) and miniphone (B and D) for Run 1. Panels A and B show the 5 Hz detrended time series and panels C and D show the 1 Hz time series.

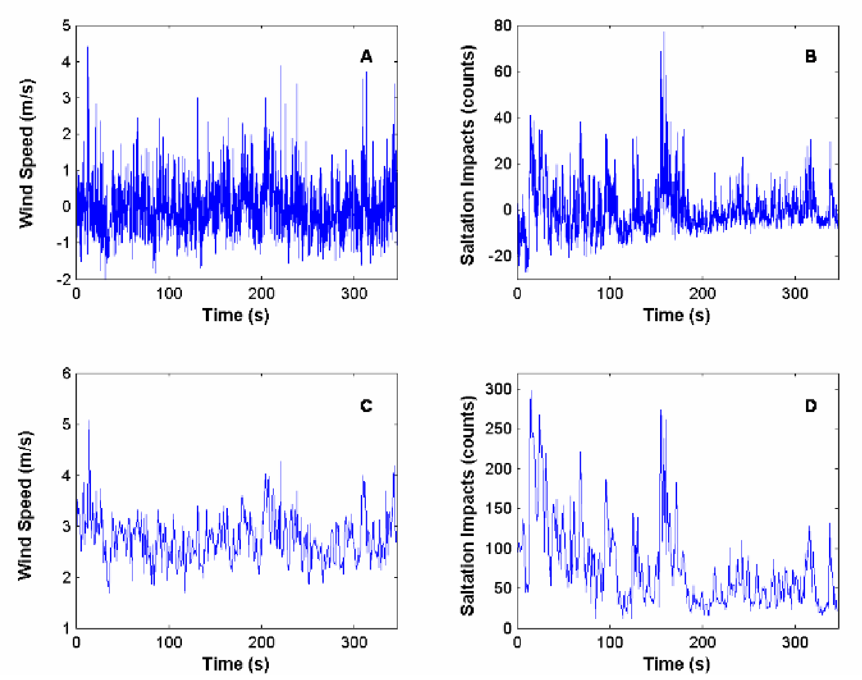

Fig. 4-12. Results from various smoothing and detrending techniques for the thermal anemometer (A and C) and miniphone (B and D) for Run 2. Panels A and B show the 5 Hz detrended time series and panels C and D show the 1 Hz time series.

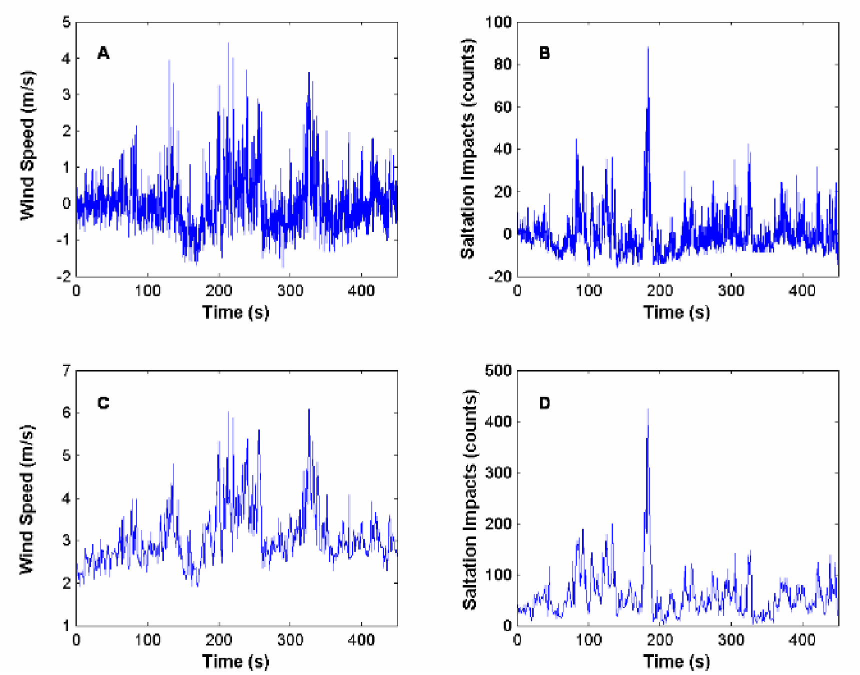

Fig. 4-13. Results from various smoothing and detrending techniques for the thermal anemometer (A and C) and miniphone (B and D) for Run 3. Panels A and B show the 5 Hz detrended time series and panels C and D show the 1 Hz time series.

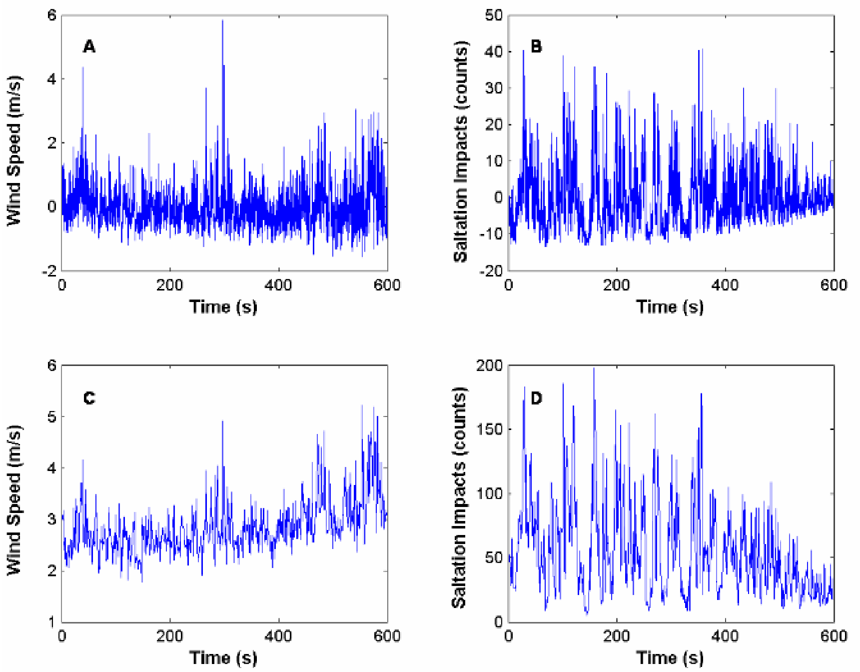

Fig. 4-14. Results from various smoothing and detrending techniques for the thermal anemometer (A and C) and miniphone (B and D) for Run 4. Panels A and B show the 5 Hz detrended time series and panels C and D show the 1 Hz time series.

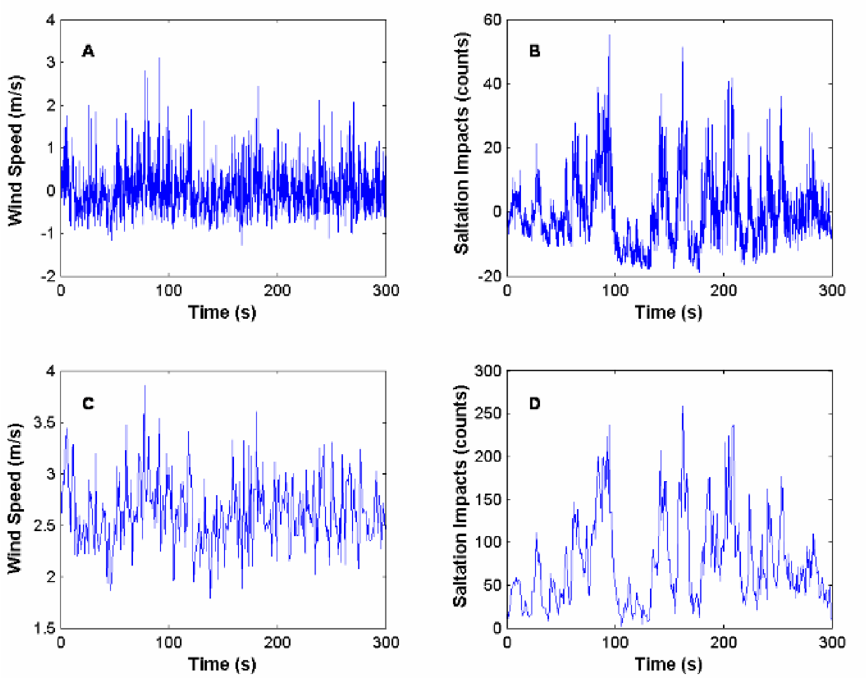

Fig. 4-15. Results from various smoothing and detrending techniques for the thermal anemometer (A and C) and miniphone (B and D) for Run 5. Panels A and B show the 5 Hz detrended time series and panels C and D show the 1 Hz time series.

4.6 Grain Size

4.6.1 Methods

Sediments collected in the hose traps were washed and oven dried for 24 hours. A splitter was used to separate the samples into 90-100 g portions. The sub-samples were placed in a Ro-Tap shaker for 15 minutes with sieves ranging in size between 0.5 and 3.25 phi, at quarter phi intervals, for a total of twelve sieves.

4.6.2 Results

The median grain size (D_{50}) for Runs 1-5 at the study site was 0.30 mm or 1.73 phi (Fig. 4-16). The sand at the site was primarily medium sand (69.7% (25.9% fine sand and 4.4% coarse sand)) and was well sorted, $\sigma = 0.135mm$ (geometric method of moments (Krumbein and Pettijohn, 1938)) (grain statistics calculated using Blott, 2000). The difference between the grain size statistics for each run was small. Sediments collected in the traps deployed during Runs 1-5 were weighed and the results are shown in Table 4-3.

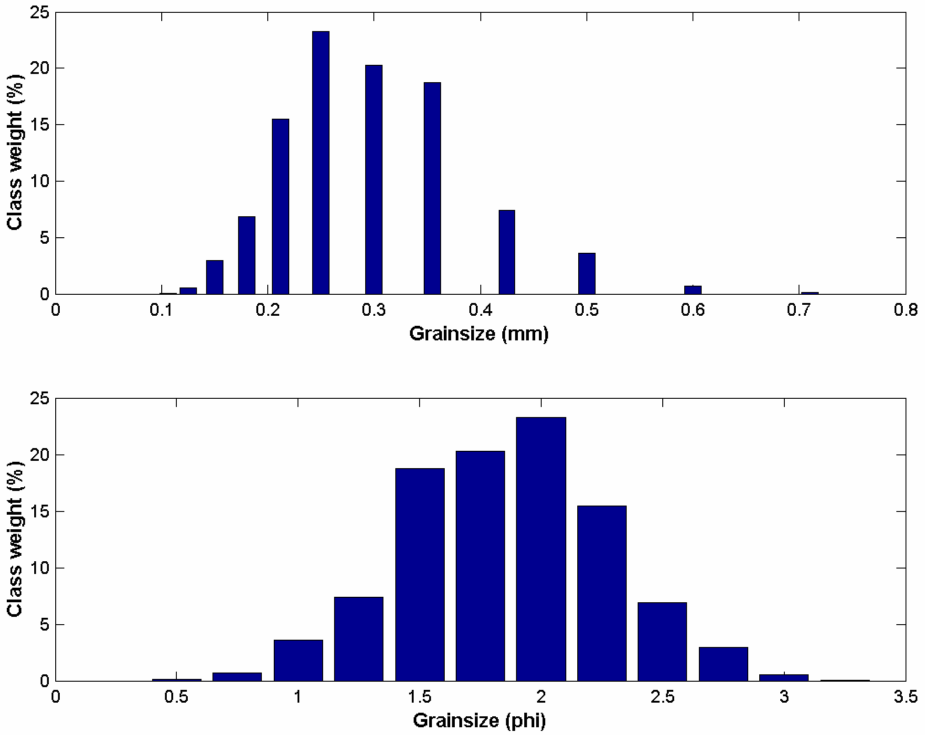

Fig. 4-16. Grain size distributions for the average of Runs 1-5, presented in the mm (top) and phi (bottom) scales.

Table 4-3. Results from the hose-style traps deployed during the data runs. Sediment trapping rate is presented, calculated by dividing sediment weight by trap deployment time. Trap 2 was deployed 20 seconds longer than the run duration for the thermal anemometers and miniphones (Table 3-1).

Run	Trap Deployment Time (s)	Sediment Weight (g)	Rate (g/s)
1	354	1018.25	2.88
2	366	2131.05	5.82
3	670	2248.59	3.36
4	1138	2987.70	2.63
5 (Trap 1)	1218	1486.47	1.22
5 (Trap 2)	1218	1535.48	1.26

5. DATA ANALYSIS

5.1 Section Introduction

In this section the general fluctuations in the wind and saltation fields using the 1 Hz data are compared qualitatively. Results from regression analysis comparing the general relationships between the wind and saltation fields are presented. The duration of the section is dedicated to presenting the results from quantitative methods using the 5 Hz demeaned wind and saltation records. First, normalized cross covariance analysis was used to determine if there was a temporal lag between the wind and saltation time series. The integral time scales derived from normalized autocorrelation and power spectral density function analyses are presented. The details of the continuous wavelet transform method are described and the rationale for selecting the Morlet wavelet base is presented. The results from the continuous wavelet transform method and the wavelet maps for the wind and saltation fields are presented. The significant regions of the wind and saltation wavelet maps were used to discern events. Cross continuous wavelet transform analysis was used to simultaneously compare the wind and saltation time series. The cross wavelet maps are presented and the significant regions of the cross wavelet maps are used to discern events.

5.2 Qualitative Analysis

The 1 Hz records for the miniphones and thermal anemometers were plotted together (Figs. 5-1 to 5-5) for visual comparison, following the approach of Davidson-Arnott and Bauer (2006) and others (see Table 2-1 in §2.4.2). Generally, there is good visual (qualitative) correspondence between the wind and saltation records. However, there are periods when the two records do not covary. In the following discussion, general trends between the wind and sand are compared.

During large portions of Run 1 (Fig. 5-1) the wind and saltation records were in phase. Around 70 s, the saltation count decreased without a corresponding decrease in wind speed. However, there were several portions of the time series, between 200-250 s, for example, where the saltation and wind appeared to be in phase. The strongest wind event did not have a corresponding saltation event (centered around 160 s). The largest saltation event (~230 s) was accompanied by a wind event.

Run 2 (Fig. 5-2) was dominated by poor correspondence between the two records between ~170 s and ~250 s. After the large saltation peak at 160 s and a secondary peak at ~170 s, the saltation record dramatically reduced without a corresponding response by the wind record.

A small precipitation event occurred (§3.2) the day before data were collected causing the sand surface to be slightly moist, especially towards the beginning of data collection. It is hypothesized that the large saltation events removed patches of the dry and available sand away from the system. The reduction in measured saltation following the large peak (for example at ~160 s) may have occurred because the system was sediment limited, i.e., there were (temporarily) no patches of sediment dry enough to reach the threshold for transport. The wind and saltation began to synchronize around 250 s, however, it is harder to observe because the time series do not overlay each other. The larger saltation peaks at the end of the time series (~320 s and ~340 s) are lagged behind the wind time series.

During Run 3 (Fig. 5-3) relatively large saltation peaks (at ~130 s, ~180 s, and ~320 s) were followed by periods of limited saltation without corresponding decreases in wind, similar to conditions observed during Run 2. Overall, during Run 3, the wind and saltation records co-varied between 0-40 s, 75-140 s, and 360-420 s There were also periods of low saltation counts that were not preceded by increases in saltation, nor were accompanied by decreases in the wind velocity (centered around 60 s, for example).

During Run 4 (Fig. 5-4) the two time series were in phase until ~510 seconds. The exceptions occurred at ~290 s and ~415 s when the saltation count decreased without a corresponding wind decrease. Also, the saltation bursts at ~110 s, ~120 s, and ~150 s appear to be disproportionate compared to the corresponding wind velocities. Toward the end of the record (~510 s to 600 s), the wind and saltation records are out-of-phase, the wind is generally increasing and the saltation counts are slightly decreasing.

The saltation record for Run 5 (Fig. 5-3) is dominated by four large peaks centered around 80 s, 140 s, 160 s, and 205 s. The wind field is not steady during these increases in saltation. Each saltation increase is followed by a rather large decrease in saltation count varying in length. Overall, this run is the most out-of-phase.

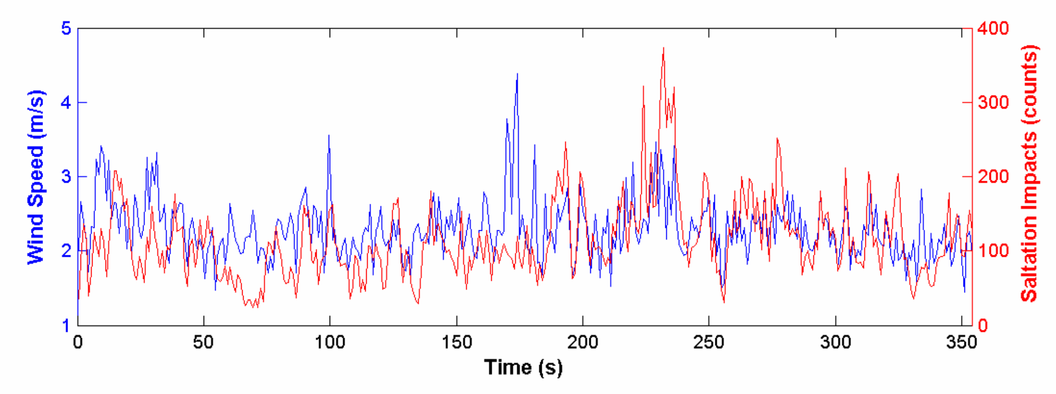

Fig. 5-1. Run 1, 1 Hz records for the wind (blue) and saltation (red).

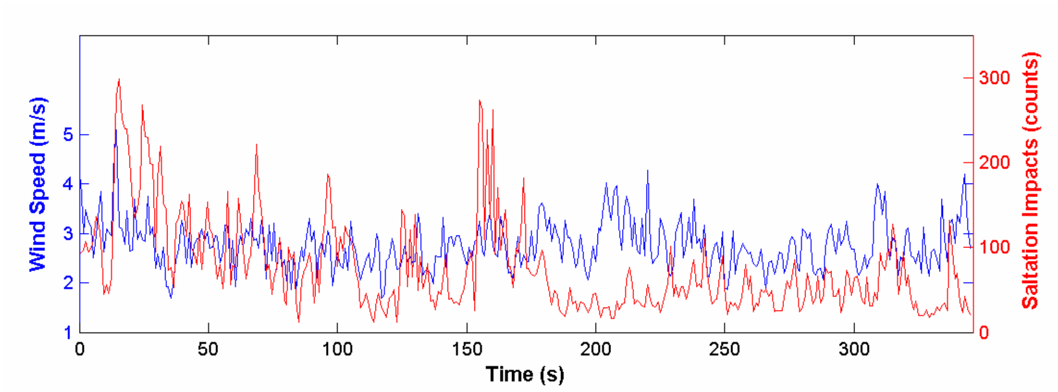

Fig. 5-2. Run 2, 1 Hz records for the wind (blue) and saltation (red).

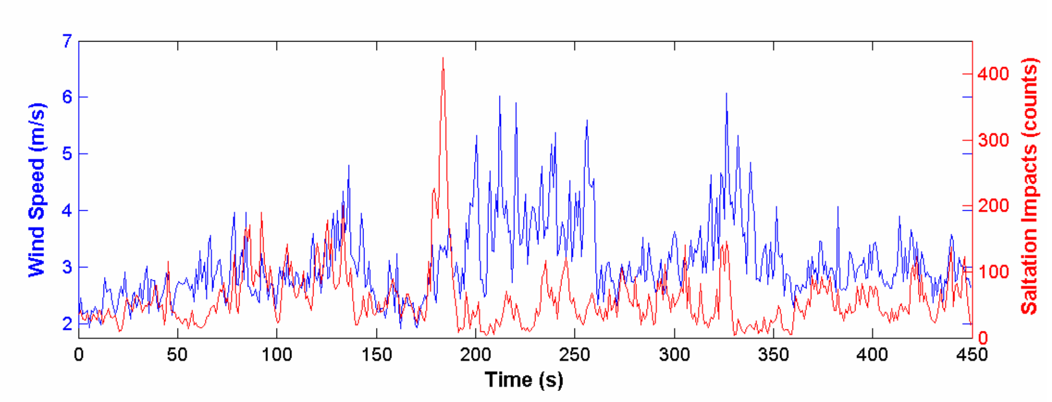

Fig. 5-3. Run 3, 1 Hz records for the wind (blue) and saltation (red).

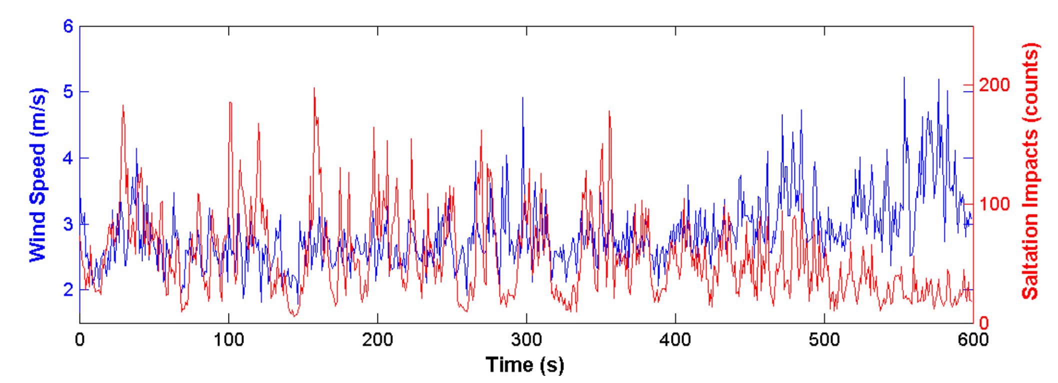

Fig. 5-4. Run 4, 1 Hz records for the wind (blue) and saltation (red).

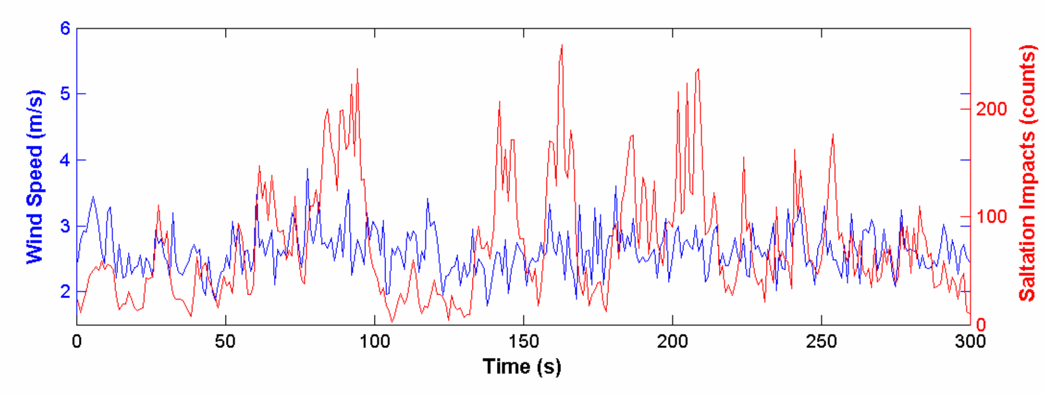

Fig. 5-5. Run 5, 1 Hz records for the wind (blue) and saltation (red).

5.3 Regression Analysis

Regression analysis was conducted using the 1 Hz thermal anemometer and miniphone records to evaluate the dependency of the saltation on the wind. Previous studies (e.g., Namikas, 2002; Davidson-Arnott and Bauer, 2006) have also employed a 1 Hz sample rate for regression analysis. Table 5-1 shows the results of this analysis. These results show a physically poor, yet statistically significant (for four of the five runs), relationship between the wind and saltation fields. The average r^2 value across all runs was 0.05, which is comparable to values reported by Namikas (2002) (using his 1 Hz data) and Davidson-Arnott and Bauer (2006) (Table 2-2). The r^2

value would most likely be improved by increasing the time averaging, as found by Namikas (2002), Sterk et al. (2002) and Leenders et al. (2005).

Table 5-1. Linear regression statistics comparing the thermal anemometer (dependent variable) with the miniphone (independent variable) 1 Hz records.

	r^2	**Slope**	**y-intercept**	***p*-value**
Run 1	0.137	48.35	3.63	0.00
Run 2	0.050	24.65	7.77	0.00
Run 3	0.011	6.96	37.33	0.03
Run 4	0.001	2.53	48.15	0.37
Run 5	0.045	33.00	-12.10	0.00

5.4 Normalized Cross-Covariance

Cross-covariance analysis was used to determine the response time of the saltation field to the fluctuating wind field. The cross-covariance coefficients were calculated by comparing the 5 Hz demeaned thermal anemometer (*x*) records to the miniphone (*y*) records using:

$$C_{xy}(\tau_k) = \frac{1}{N-k}\sum_{i=1}^{N-k}(x_i - \bar{x})(y_{i+k} - \bar{y}) \qquad (5\text{-}1)$$

where $\tau = k\Delta t$ and is the lag time for *k* sampling intervals (Δt) in seconds. Cross-covariance coefficients were normalized by the standard deviation (σ) using $\rho_{xy} = C_{xy} / \sigma_x \sigma_y$. Normalized coefficients (ρ_{xy}) range between -1 and 1 and maximum correlation is indicated by unity. Confidence intervals at 95% were calculated using 2σ according to Sciremammano (1979).

Cross-covariance analysis revealed that with exception to Run 2, the dominant significant peak was at the zero lag (Fig. 5-6). The dominant peak during Run 2 was at 0.2 seconds. The normalized cross-covariance coefficients for a lag of 0 and 0.2 s are: $\rho_{xy}(\tau_0) = 0.1556$ and $\rho_{xy}(\tau_{0.2}) = 0.1625$, respectively for Run 2. A positive lag of 0.2 seconds indicates that the wind is leading the saltation by 0.2 seconds. The zero lag peak for Run 3 was not significant.

These results indicate the sand is responding almost instantaneously (<0.2 s, restricted by sample rate of input data) to fluctuations in the wind field. Most laboratory studies and numerical models suggest response times on the order of one second (e.g., Butterfield, 1991, 1993; §2.4.1), however, Baas (2003) measured a response time of 0.5 seconds in the field. Determination of the response time is fundamental to future data analysis in this research. If a lag time on the order of several seconds had been detected, for example, the wind and saltation time series would have been temporally adjusted so they were in phase.

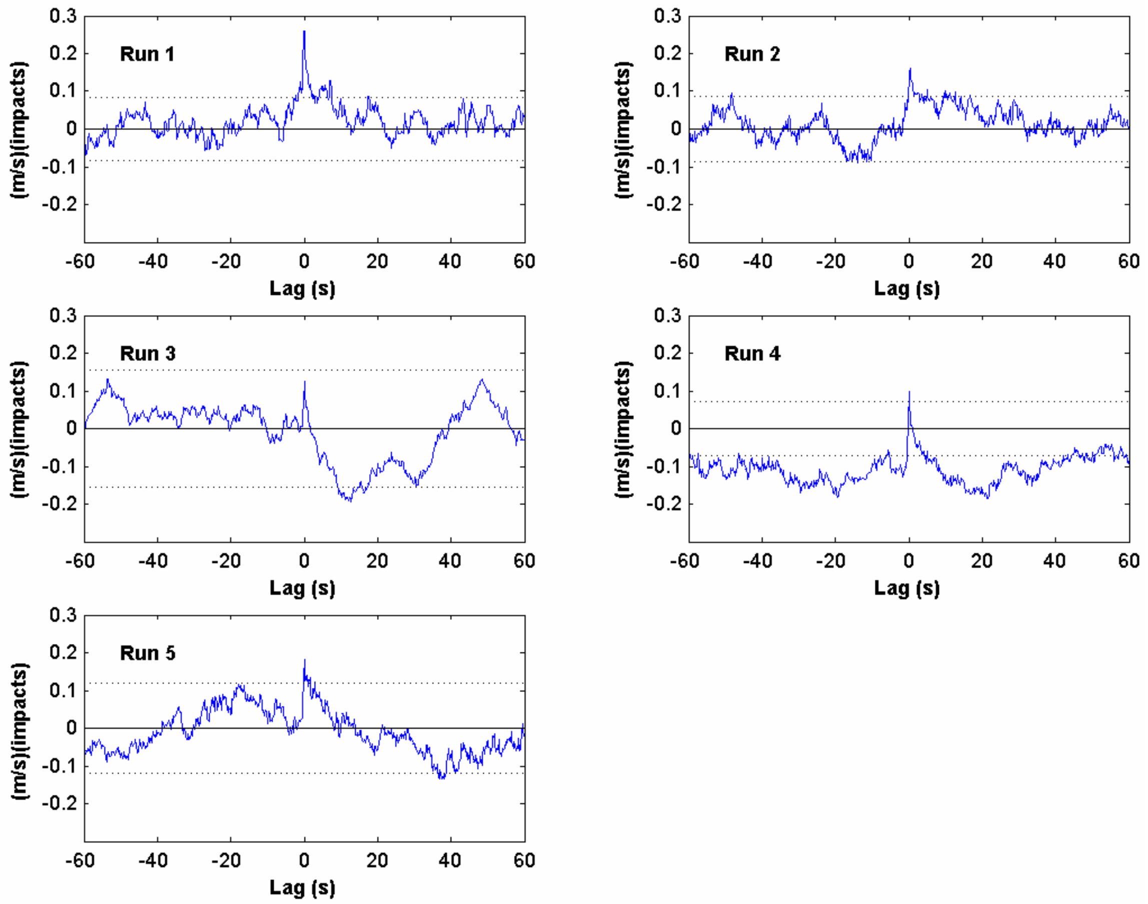

Fig. 5-6. Results of normalized cross-covariance analysis. Dashed lines indicate the 95% confidence interval and positive lags indicate the saltation is lagging the wind.

5.5 Estimating the Integral Time Scale

5.5.1 Normalized Autocorrelation Function

The integral time scale is one of the characteristic scales of turbulence (§2.2.4) and it can be calculated using the autocorrelation function or power spectral density analysis. Both methods are used here. Autocorrelation function (ACF) coefficients were calculated for the miniphone and thermal anemometers using the 5 Hz demeaned data following:

$$C_{xx}(\tau)=\frac{1}{N-k}\sum_{i-1}^{N-k}\left(x_i x_{i+k}\right) \tag{5-2}$$

where x is a value in a time series (either miniphone or thermal anemometer) with a length N, and $\tau = k\Delta t$ is the lag time for k sampling intervals (Δt) in seconds. ACF coefficients (ρ_{xx}) were normalized by the standard deviation (σ) of the time series x using $\rho_{xx} = C_{xx}/\sigma_x$. Normalized coefficients range between -1 and 1. The 95% confidence interval lines were plotted at $\pm 2/\sqrt{N}$. Integral time scales were calculated by finding the maximum value of the cumulative integral of the autocorrelation coefficients (§2.2.4).

Graphs showing the normalized autocorrelation results are shown in Figs. 5-7 and 5-8, for the wind and saltation, respectively. Table 5-2 shows the integral time scale for the wind and saltation. The average integral time scales for the wind and saltation are 1.84 seconds and 2.14 seconds, respectively. There is more variation about the mean for the wind than for the sand integral time scale. The standard error of the mean ($\sigma_m = \sigma/\sqrt{n}$) for the wind and saltation was 0.59 and 0.24 seconds, respectively. During Run 5, the shortest integral time scale for the wind (0.78 s) and the longest integral time scale for the saltation (2.84 s) was observed.

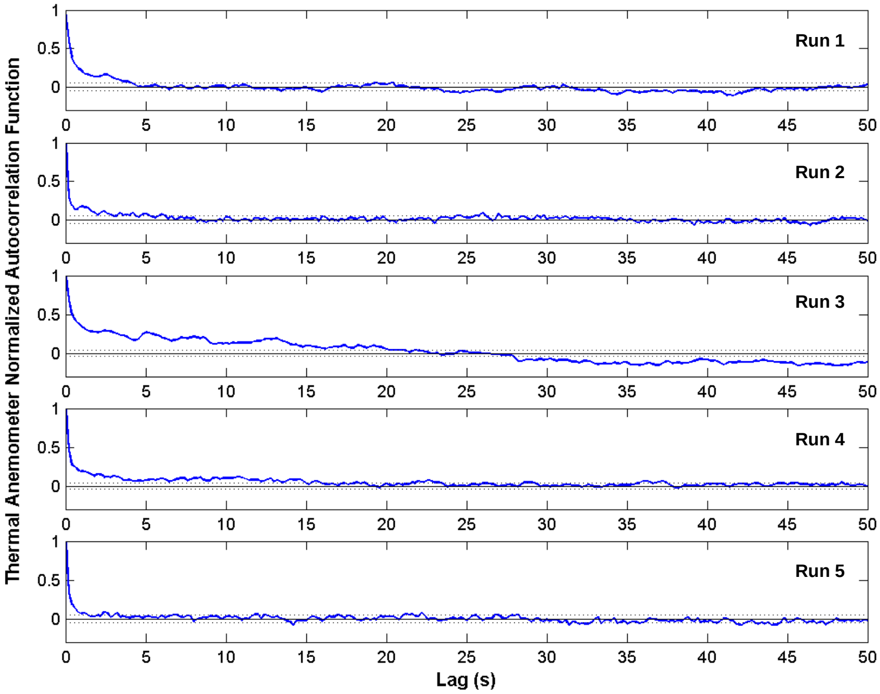

Fig. 5-7. Normalized autocorrelation results from the thermal anemometer (wind) for Runs 1-5. The dashed lines indicate the 95% confidence intervals and the solid line is at zero.

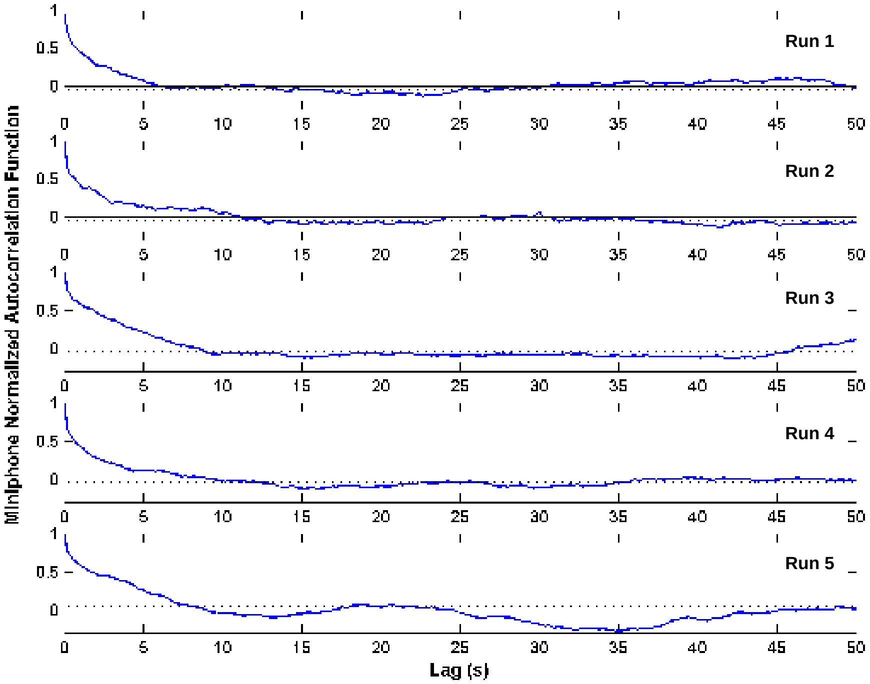

Fig. 5-8. Normalized autocorrelation results from the miniphone (saltation) for Runs 1-5. The dashed lines indicate the 95% confidence intervals and the solid line is at zero.

Table 5-2. Integral time scales derived from the normalized auto correlation function for the wind and saltation records.

NACF Integral Time Scales		
	Wind (s)	**Saltation (s)**
Run 1	0.85	1.55
Run 2	1.08	2.09
Run 3	3.68	2.52
Run 4	2.81	1.72
Run 5	0.78	2.84
Avg.	*1.84*	*2.14*

5.5.2 Power Spectral Density

Power spectral density was calculated using the 5 Hz demeaned records using:

$$S_{xx}(f_k) = \frac{\Delta t}{N}\left[X^*(f_k)X(f_k)\right] \tag{5-3}$$

where k=0,1,2…N-1 and (*) is the complex conjugate. The records were divided into 64 point lengths (to increase the degrees of freedom and decrease the width of the confidence bands), demeaned, and a Hanning window was applied. Only the following frequencies (f) were considered, according to Nyquist:

$$0 \le f \le {}^{1}\!/_{2\Delta t} \tag{5-4}$$

Power spectral density results are shown in Figs. 5-9 and 5-10 for wind and saltation, respectively. The frequencies where the spectral peaks occur, the integral time scales, are shown on Table 5-3. Four of the five runs have a maximum spectral peak at 1.60 s, Run 2 is different with a spectral density peak for wind and sand at 1.42 s and 1.83 s, respectively. Standard errors of the means for wind and saltation are 0.08 and 0.10 s, respectively.

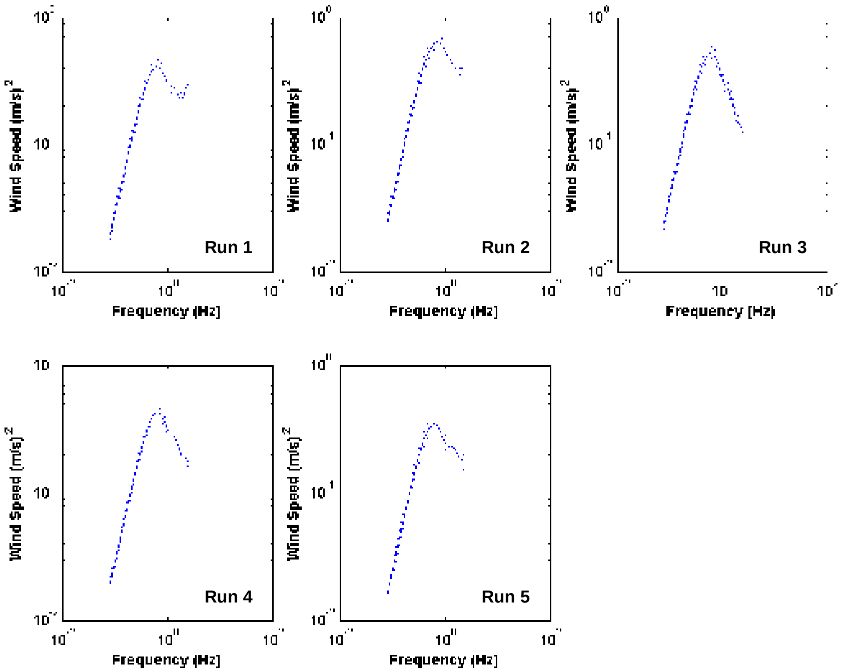

Fig. 5-9. Power spectral density results for the wind field for Runs 1-5. The dashed lines are the 95% confidence intervals.

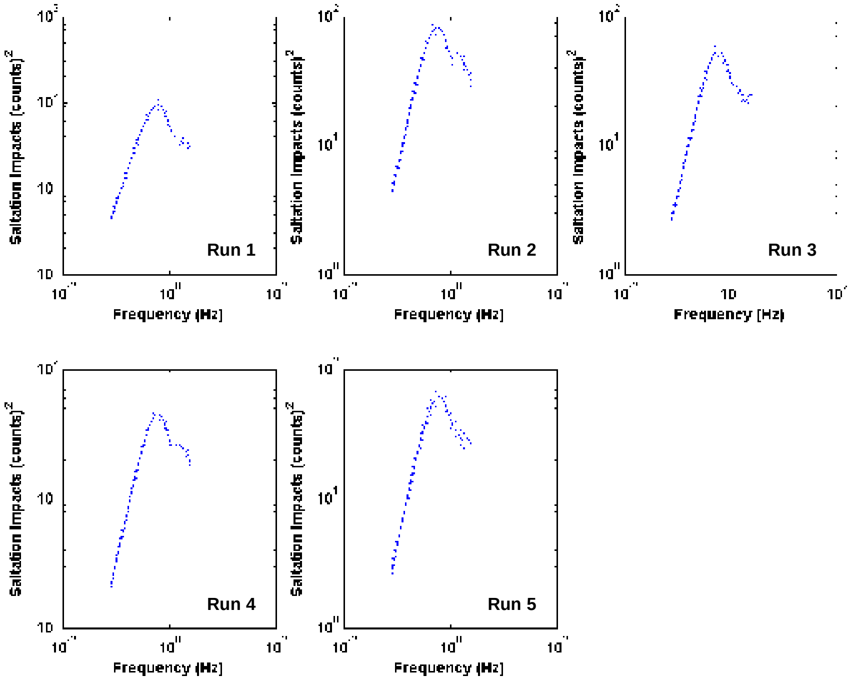

Fig. 5-10. Power spectral density results for the saltation for Runs 1-5. The dashed lines are the 95% confidence intervals.

Table 5-3. Integral time scales for the wind and saltation estimated from the peaks of the power spectral density analysis.

Power Spectral Density Integral Time Scales		
	Wind (s)	**Saltation (s)**
Run 1	1.60	1.60
Run 2	1.42	1.83
Run 3	1.60	1.60
Run 4	1.60	1.60
Run 5	1.60	1.60
Avg.	*1.56*	*1.65*

Integral time scales for wind and saltation estimated using the normalized autocorrelation and the power spectral density methods were all approximately two seconds. The differences between the averages for two methods for the wind and saltation were approximately 0.3 and 0.5 seconds, respectively. If all estimations, using both methods, are averaged, the integral time scale for wind is 1.70 s and for saltation is 1.90 s. The strong similarity between the estimations calculated using normalized autocorrelation and power spectral density methods indicate that the integral time scale for wind and saltation is around two seconds.

5.6 Continuous Wavelet Transform

5.6.1 Method

Continuous wavelet transform (CWT) analysis was performed on the 5 Hz demeaned thermal anemometer and miniphone time series to locate local variations of power within the records and ultimately locate events in the respective time series. Zero padded time series (to lengths equaling powers of two) were convolved with the Mexican hat (Eq. 2-18) and the Morlet (Eq. 2-17) wavelet functions (§2.5.2). For each wavelet function, scales (a_j) were calculated using (according to Torrance and Compo, 1998):

$$J = \delta j^{-1} \log_2 \left(N \delta t / a_0 \right) \tag{5-5}$$

$$a_j = a_0 2^{J\delta j} \tag{5-6}$$

where a_0 is the smallest resolvable scale equivalent to $2\delta t$, δt is sample rate (in seconds) (therefore, 0.4 for this research), *N* is the maximum number of samples in the time series, and $\delta j = 0.125$. The δj value relates to the spectral width of the wavelet base and smaller values increase the resolution of the wavelet map. In her paper that focused on intermittent turbulence at small scales (<2.0 seconds), Salmond (2005) selected $\delta j = 0.5$, the “largest value that still gives adequate sampling in scale” for the Morlet wavelet base (Torrence and Compo 1998: 67). Torrence and Compo (1998: 67) indicated that one can use an “arbitrary” set of scales to build up to a “complete picture” according to the data. For this research, scales between 0.4 and 121.77 s were employed.

For the Morlet wavelet (Eq. 2-17), a non-dimensional frequency (ω_0) of six was used, following Farge (1992). Continuous wavelet power was calculated by squaring the wavelet coefficients (calculated using Eq. 2-16). The power wavelet transform coefficients were normalized by $1/\sigma^2$ for easier comparison between the wind and saltation results.

The continuous wavelet transform power coefficients were plotted over time and wavelet scale (i.e., the wavelet maps). On the wavelet maps, regions with higher relative power have ‘hotter’ colors, i.e., red and orange, and regions with lower relative power have ‘cooler’ colors, i.e., blue and cyan. Portions of the CWT that were significant at the 5% level are designated by bold black lines. The Cone of Influence (COI), a region that is created at the beginning and end of the CWT time series and becomes larger (i.e., longer in time) with increasing scale, was also plotted. The region within the COI, shaded grey on the wavelet maps, represents results that should be interpreted cautiously (Torrence and Compo, 1998). The MATLAB code used in this dissertation to calculate the COI and the wavelet significance was modified from Torrence and Compo (2006).

To focus on small scale fluctuations in the wavelet time series, wavelet power coefficients found at scales less than or equal to 3.0 seconds, and that were significant at the 5% level were vertically integrated and multiplied by $1/\log_2(scale)$. This calculation results in a time series that shows either the wind or sand events occurring at the primary response time scale of Butterfield (1991; 1993). Using this “event time series,” event duration for the wind and sand time series are calculated.

5.6.2 Wavelet Base Selection

The results of the continuous wavelet transform for the saltation time series collected during Run 1 using the Mexican hat wavelet base are shown in Fig. 5-11. Fig. 5-12 shows the same saltation time series (Run 1) using the Morlet wavelet. Generally, both wavelet maps have a vertical (i.e., oriented according to the *y*-axis) pattern at the smaller wavelet scales, more so with the Mexican hat. The regions of the Morlet wavelet map that are significant (at the 5% level) at the small wavelet scales (<3 s) correspond with the increases in saltation better than the significant regions on the Mexican hat wavelet map. For example, the increased periods of saltation around 40 s, 100 s, and 345 s are not selected (at the 5% level) by the Mexican hat, but are selected using the Morlet wave base. Visual qualitative inspection of Fig. 5-12 (Morlet wavelet) reveals that increases in the saltation record are selected by the Morlet wavelet base when using the confidence levels and when focusing on the small wavelet scales.

Fig. 5-13 shows the Mexican hat (top) and Morlet (bottom) wave bases for the saltation time series (Run 1). The maps in Fig. 5-13 are the same as those shown in Figs. 5-11 and 5-12, except that Fig. 5-13 only shows the wavelet scales between 0.4 s and 3.0 s. Fig. 5-13 illustrates in more detail than Figs. 5-11 and 5-12 that the increases in the saltation time series correspond better with the Morlet wavelet map than with the Mexican hat wavelet map, in particular the significant portions of the wavelet maps. The Morlet wave base will be used in this dissertation because of its superior performance to select small-scale fluctuations in the time series and because Salmond (2005) used this wave base in her research (which is similar to this work).

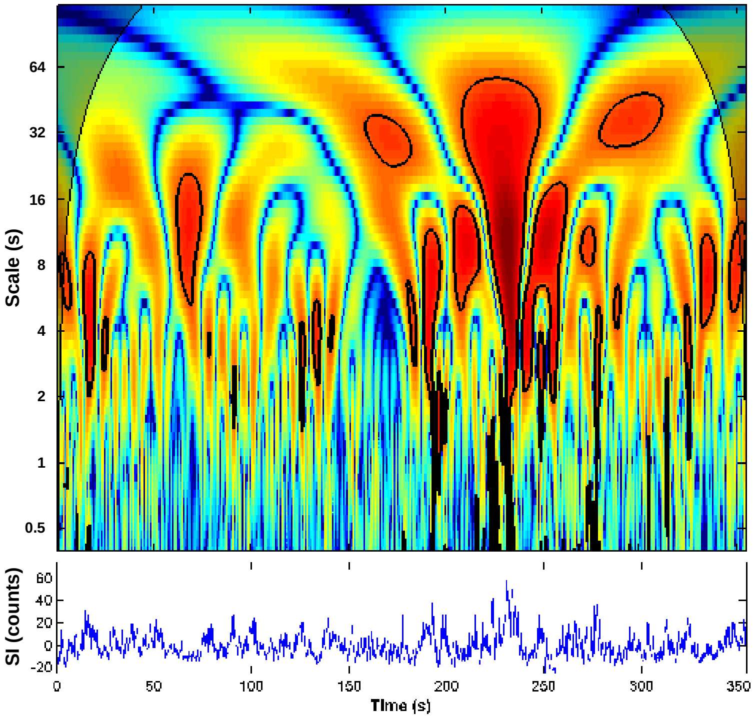

Fig. 5-11. Results from the continuous wavelet transform using the Mexican hat wavelet base (top) of the demeaned saltation time series from Run 1 (bottom). Colors on the wavelet map (top) indicate wavelet power intensity. 'Hotter' colors (red and orange) indicate higher power and 'cooler' colors (blue and cyan) indicate lower power. The bold black lines on the wavelet map designate regions that are significant at the 5% level (95% confidence interval).

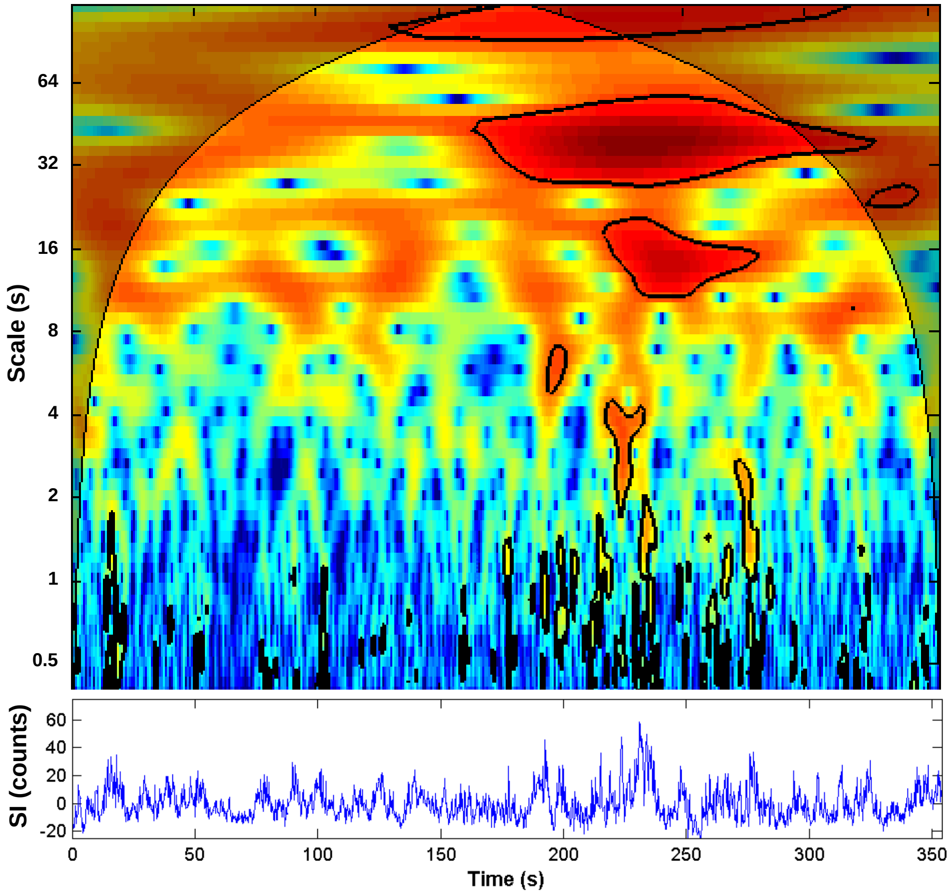

Fig. 5-12. Results from the continuous wavelet transform using the Morlet wavelet base (top) of the demeaned saltation series from Run 1 (bottom). Colors on the wavelet map (top) indicate wavelet power intensity. ‘Hotter’ colors (red and orange) indicate higher power and ‘cooler’ colors (blue and cyan) indicate lower power. The bold black lines on the wavelet map designate regions that are significant at the 5% level (95% confidence interval).

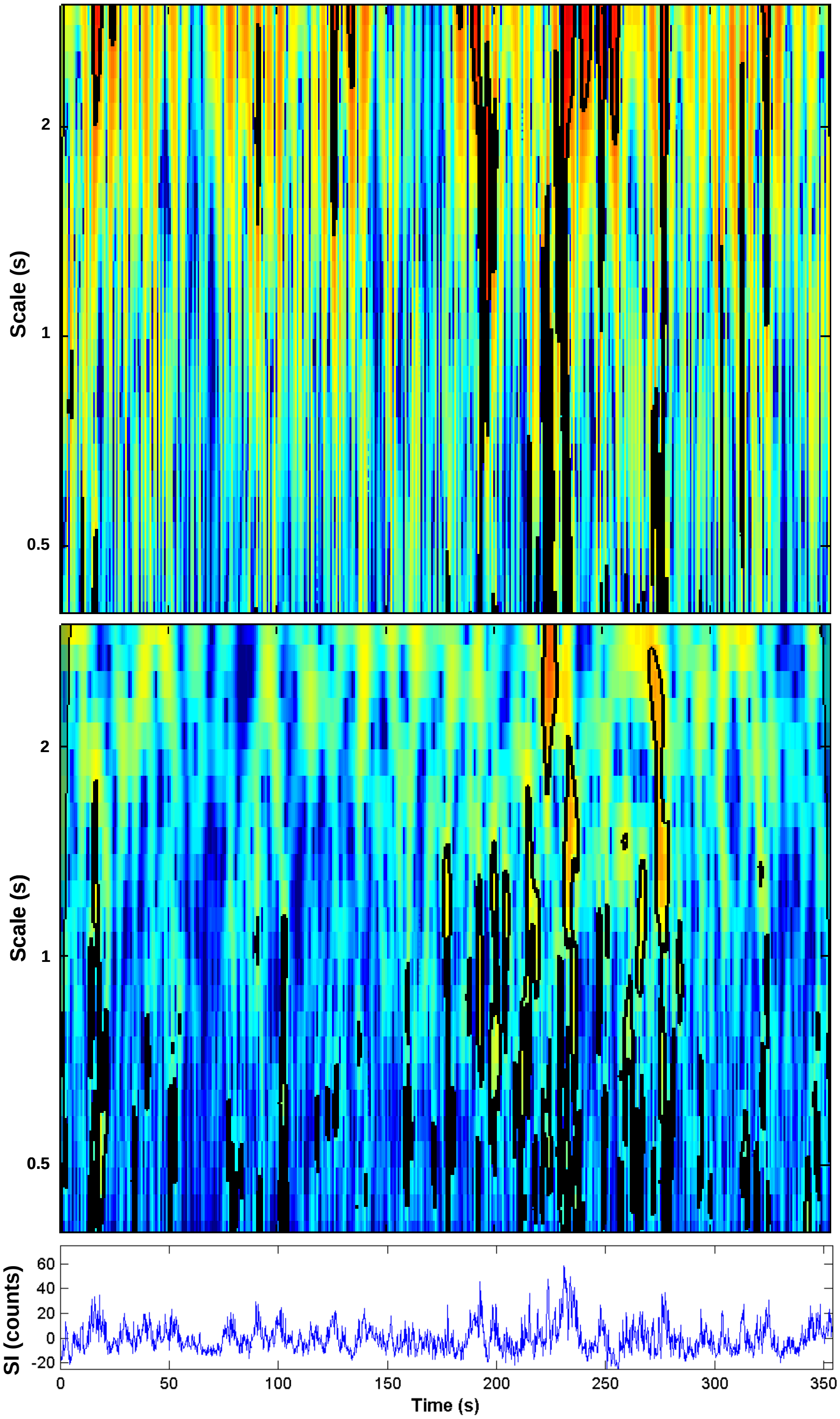

Fig. 5-13. Wavelet map using the Mexican hat (top) and Morlet (bottom) wavelet bases on the demeaned saltation time series from Run 1. Only wavelet scales 0.4-3.0 s are shown. Colors on the wavelet maps indicate wavelet power intensity. 'Hotter' colors (red and orange) indicate higher power and 'cooler' colors (blue and cyan) indicate lower power. The bold black lines on the wavelet maps designate regions that are significant at the 5% level (95% confidence interval).

5.6.3 Wavelet Maps

The wind and saltation wavelet maps for Runs 1-5 are shown in Figs. 5-14 to 5-18. The wind wavelet results are shown on the top wavelet map and the saltation on the bottom wavelet map. Above and below the wind and saltation maps, respectively, are the corresponding 5 Hz demeaned time series. A few generalizations can be made about all the wavelet maps:

1) Greater relative wavelet powers, denoted by “hotter” colors, are generally found at the larger scales;
2) There is strong correspondence between the 5% significance level regions, in particular, the scales at less than about three seconds, and the input time series. These periods of significance are short (i.e., <5 s) in duration.
3) Between the wavelet scales of 32 s and 64 s, there are long-lasting (in the *x*-axis direction), high-energy, regions that are significant at the 95% confidence interval that persist.

Visual inspection of the wind and saltation, particularly the small scales (≤3 s) reveal that periods of wind match fairly well with periods of saltation. Wavelet analysis reveals several instances where there is little significant wind or saltation for tens of seconds. For example, at the beginning (~0-75 s) of Run 3 there are two significant events in the wind and saltation wavelet maps. All four events occur at scales less than one. There is a region that is within the 95% confidence interval at the beginning of Run 3 in the wind and saltation fields in the larger scales (>32 s), however, this region is within the Cone of Influence (c.f., §5.6.1). Analysis of the individual wavelet maps are discussed below.

The Run 1 wind wavelet map (Fig. 5-14) is dominated by significance (defined in this analysis as above the 95% confidence interval and designated on the wavelet map by the bold, black lines) from ~0-275 s at the larger scales. The 5 Hz demeaned time series shows that generally, the mean of the wind speed between 0-275 s is slightly higher than mean toward the end of the record. A significant wavelet event around 175 s is present at almost every scale and corresponds with the largest increase in the wind time series. Between 175-300 s on the saltation Run 1 wavelet map (Fig. 5-14), there is a cluster of significance corresponding with an increase in saltation. The details of the increase in saltation between 175-300 s is shown by the small increase of significance in the small wavelet scales. The significant wavelet region around a wavelet scale of 32 s between 175 and 300 seconds corresponds with the general increase in mean saltation.

The significant wavelet regions occurring at the small wavelet scales on the wind wavelet map Run 2 (Fig. 5-15) between 0-260 seconds are more evenly distributed (temporally) compared to other runs. This run did not have a high amount of wavelet power at the larger scales compared to the other runs. The corresponding saltation wavelet map did have a lot of power at the larger scales for the first 175 seconds of the record. After ~175 seconds, the wavelet power reduced dramatically and there were almost no significant regions in the smaller wavelet scales. The reduction in wavelet power after ~175 s matches the reduction of counts in the saltation time series.

The wind and saltation wavelet maps for Run 3 (Fig. 5-16) show cooler colors (low power) between 0-75 seconds, corresponding with reduced wind velocities and saltation counts. The significance in the wind wavelet map is dominated by significant activity at 200-250 s at wavelet scales between 0.4 s and ~20 s, corresponding with an increase in wind velocity. The Run 3 saltation time series has a large peak at ~175 s that coincides with a region of significance that spans almost all the wavelet scales.

The average wind speed during Run 4 (Fig. 5-17) increases throughout the run. Between ~450-600 s that wind speed increase is evident on the wavelet map because there is significance at every scale, in particular an increased amount at the lower scales compared to the other portions of the time series. The saltation wavelet map shows an increase of cooler colors toward the end of the run, especially the last ~25 s, indicating that the wavelet power is low. The saltation impact count decreases toward the end of the run, so the wavelet map corresponds with the time series.

Significance at the small wavelet scales is fairly consistent throughout the Run 5 wind wavelet map (Fig. 5-18), with exception to the period between 130-150 s (during which there is a slight decrease in the mean wind velocity). The saltation wavelet map for Run 5 shows that there are two periods where there are no significant regions at scales less than 16 s, between ~0-55 s and between ~100-130 s. In particular, in the region around 100 seconds, the demeaned saltation count is negative with no large increases, therefore a strong wavelet power is not expected.

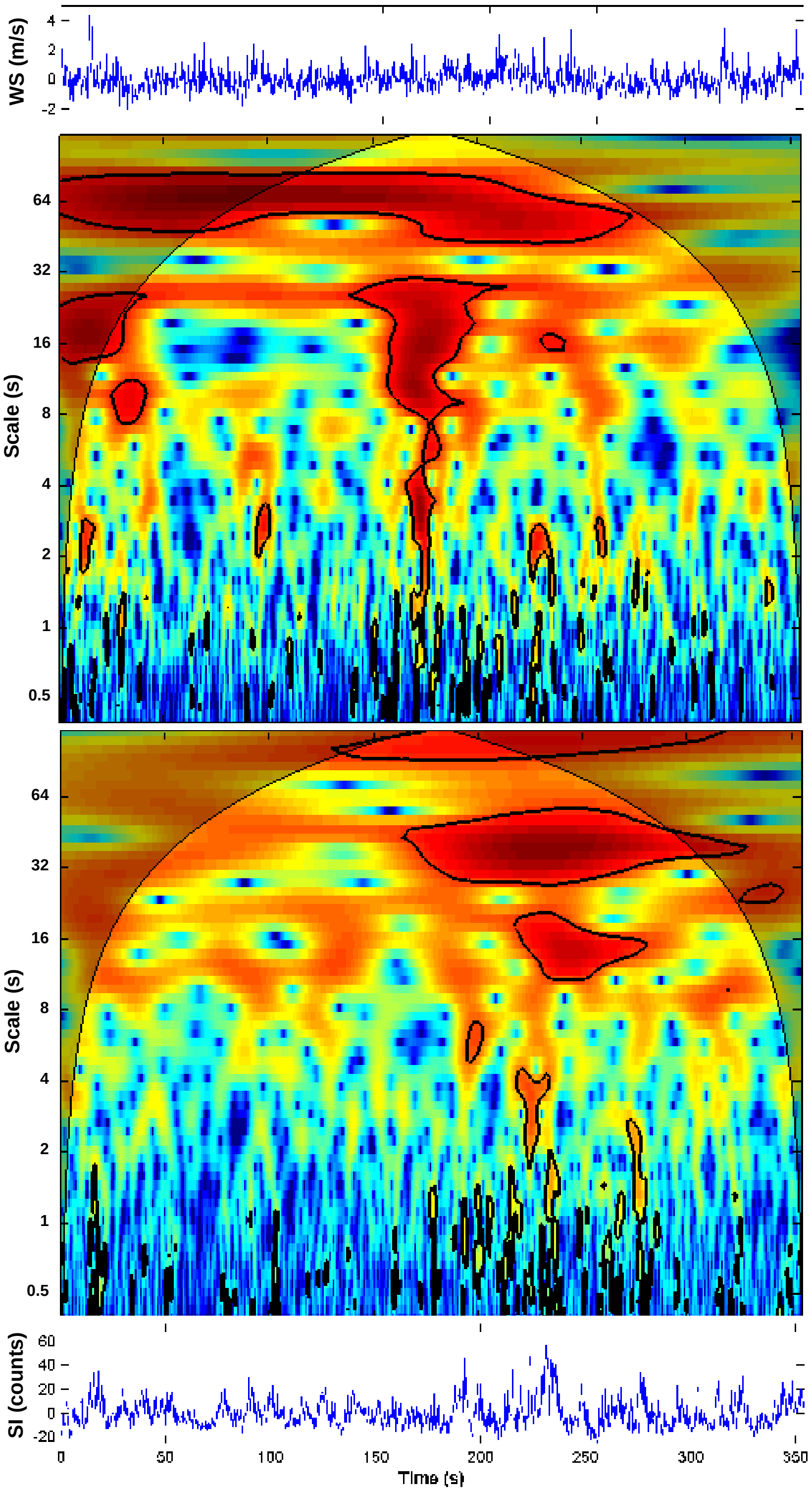

Fig. 5-14. Continuous wavelet transform wavelet map using a Morlet wave base for Run 1, wind (top wavelet map) and saltation (bottom wavelet map). The time series (5 Hz detrended) used in the wavelet analysis are shown above (wind) and below (saltation) the wavelet maps. Colors on the wavelet maps indicate wavelet power intensity. ‘Hotter’ colors (red and orange) indicate higher power and ‘cooler’ colors (blue and cyan) indicate lower power. The bold black lines on the wavelet maps designate regions that are significant at the 5% level (95% confidence interval).

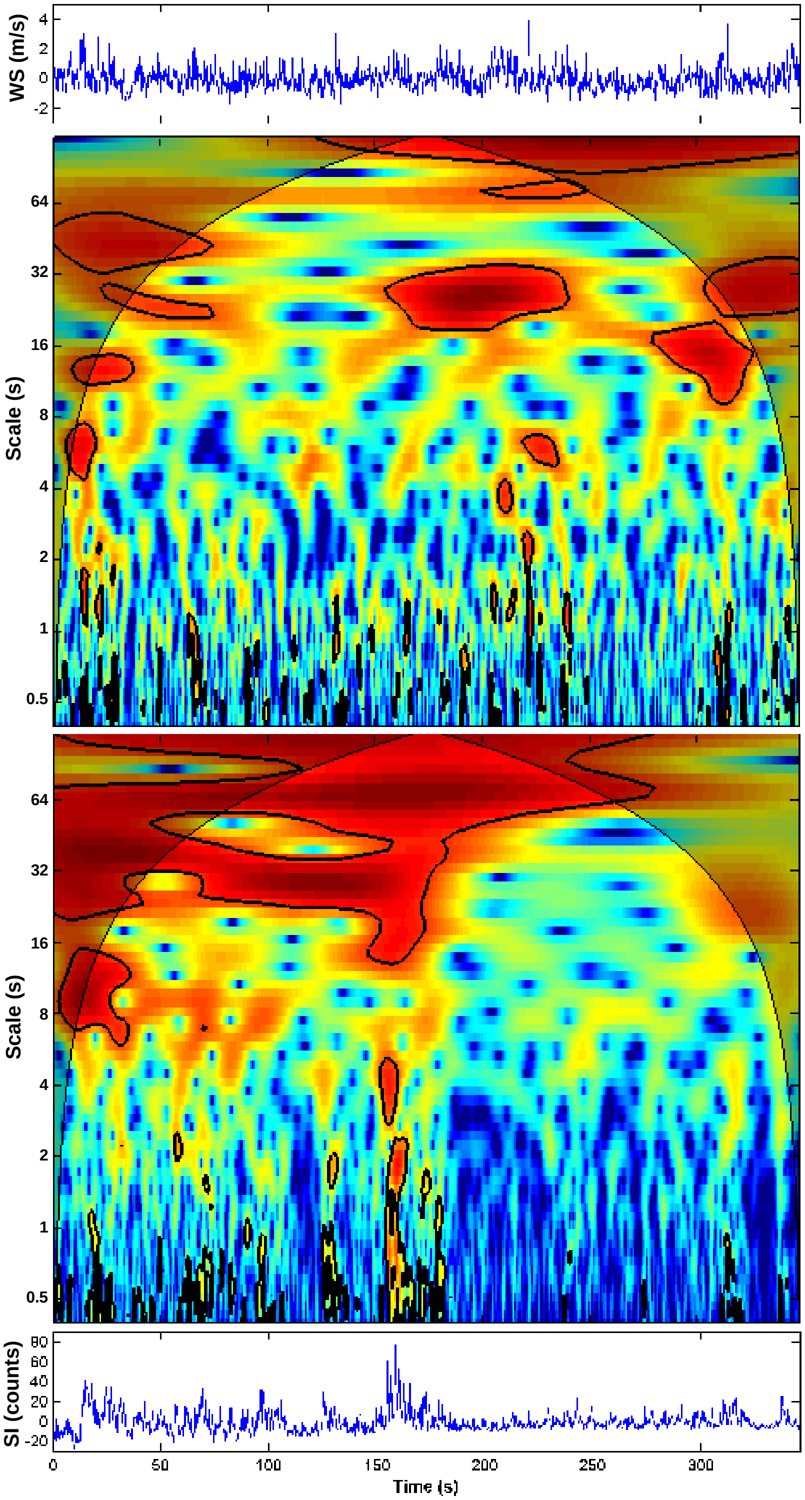

Fig. 5-15. Continuous wavelet transform wavelet map using a Morlet wave base for Run 2, wind (top wavelet map) and saltation (bottom wavelet map). The time series (5 Hz detrended) used in the wavelet analysis are shown above (wind) and below (saltation) the wavelet maps. Colors on the wavelet maps indicate wavelet power intensity. 'Hotter' colors (red and orange) indicate higher power and 'cooler' colors (blue and cyan) indicate lower power. The bold black lines on the wavelet maps designate regions that are significant at the 5% level (95% confidence interval).

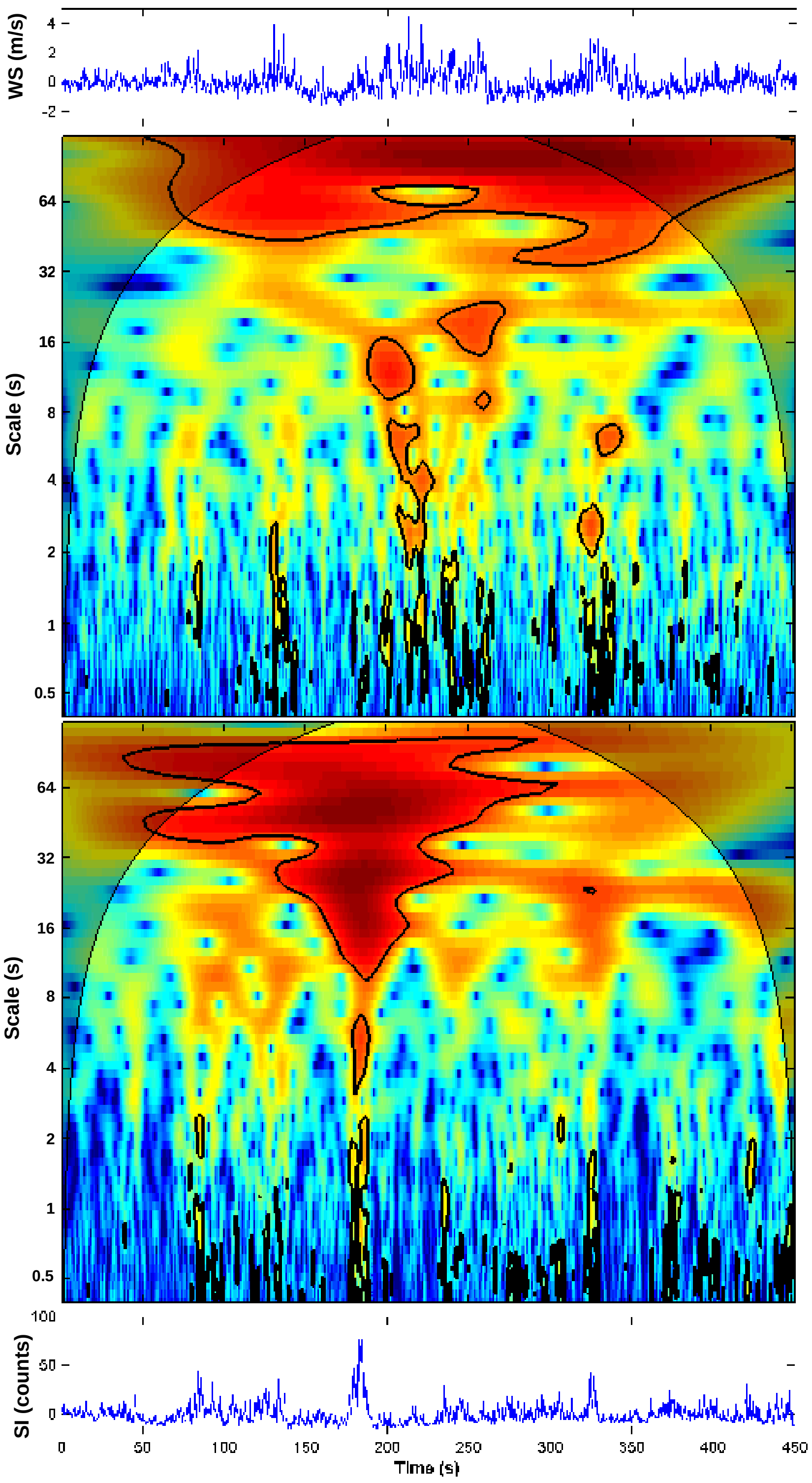

Fig. 5-16. Continuous wavelet transform wavelet map using a Morlet wave base for Run 3, wind (top wavelet map) and saltation (bottom wavelet map). The time series (5 Hz detrended) used in the wavelet analysis are shown above (wind) and below (saltation) the wavelet maps. Colors on the wavelet maps indicate wavelet power intensity. ‘Hotter’ colors (red and orange) indicate higher power and ‘cooler’ colors (blue and cyan) indicate lower power. The bold black lines on the wavelet maps designate regions that are significant at the 5% level (95% confidence interval).

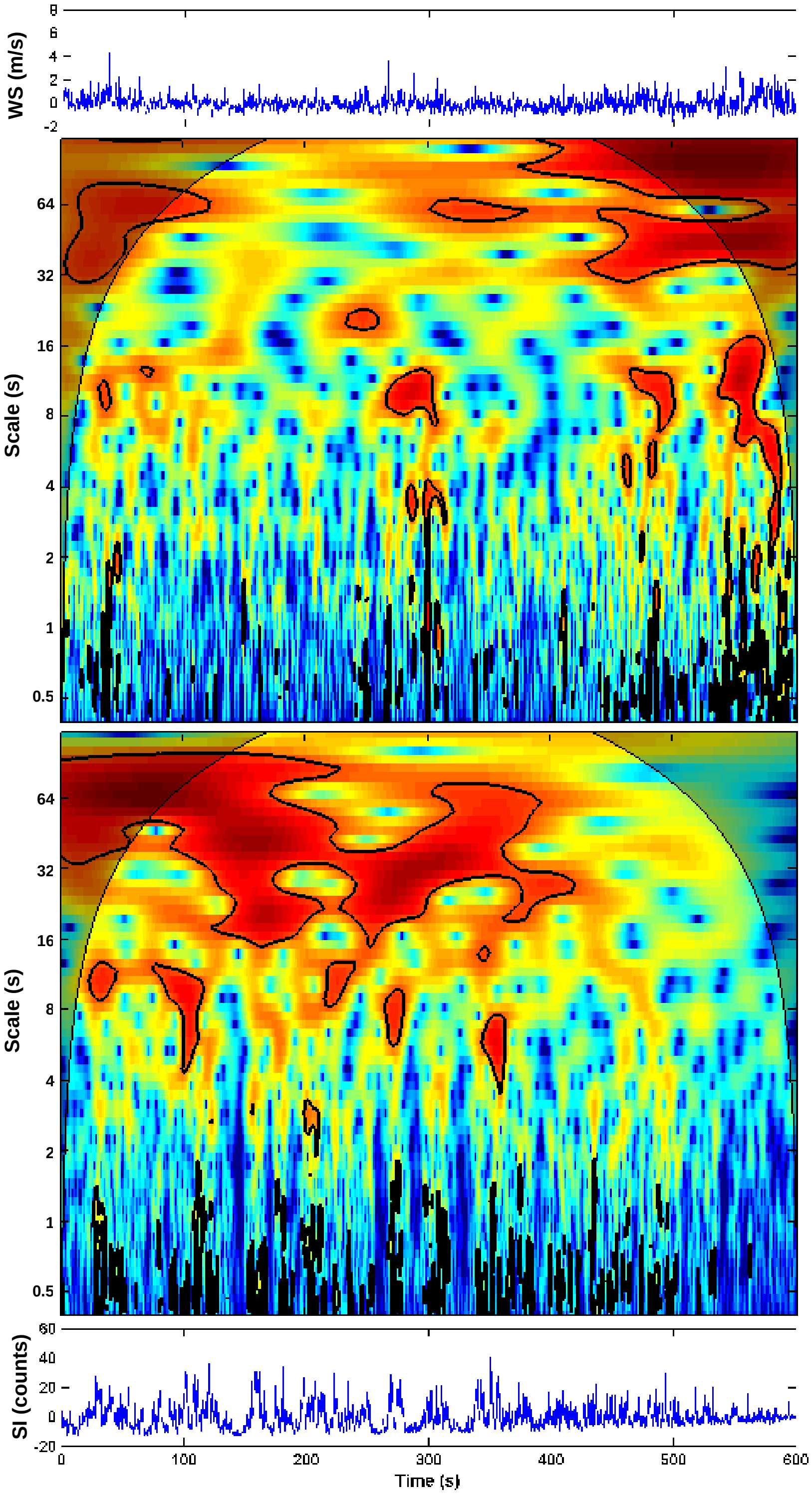

Fig. 5-17. Continuous wavelet transform wavelet map using a Morlet wave base for Run 4, wind (top wavelet map) and saltation (bottom wavelet map). The time series (5 Hz detrended) used in the wavelet analysis are shown above (wind) and below (saltation) the wavelet maps. Colors on the wavelet maps indicate wavelet power intensity. ‘Hotter’ colors (red and orange) indicate higher power and ‘cooler’ colors (blue and cyan) indicate lower power. The bold black lines on the wavelet maps designate regions that are significant at the 5% level (95% confidence interval).

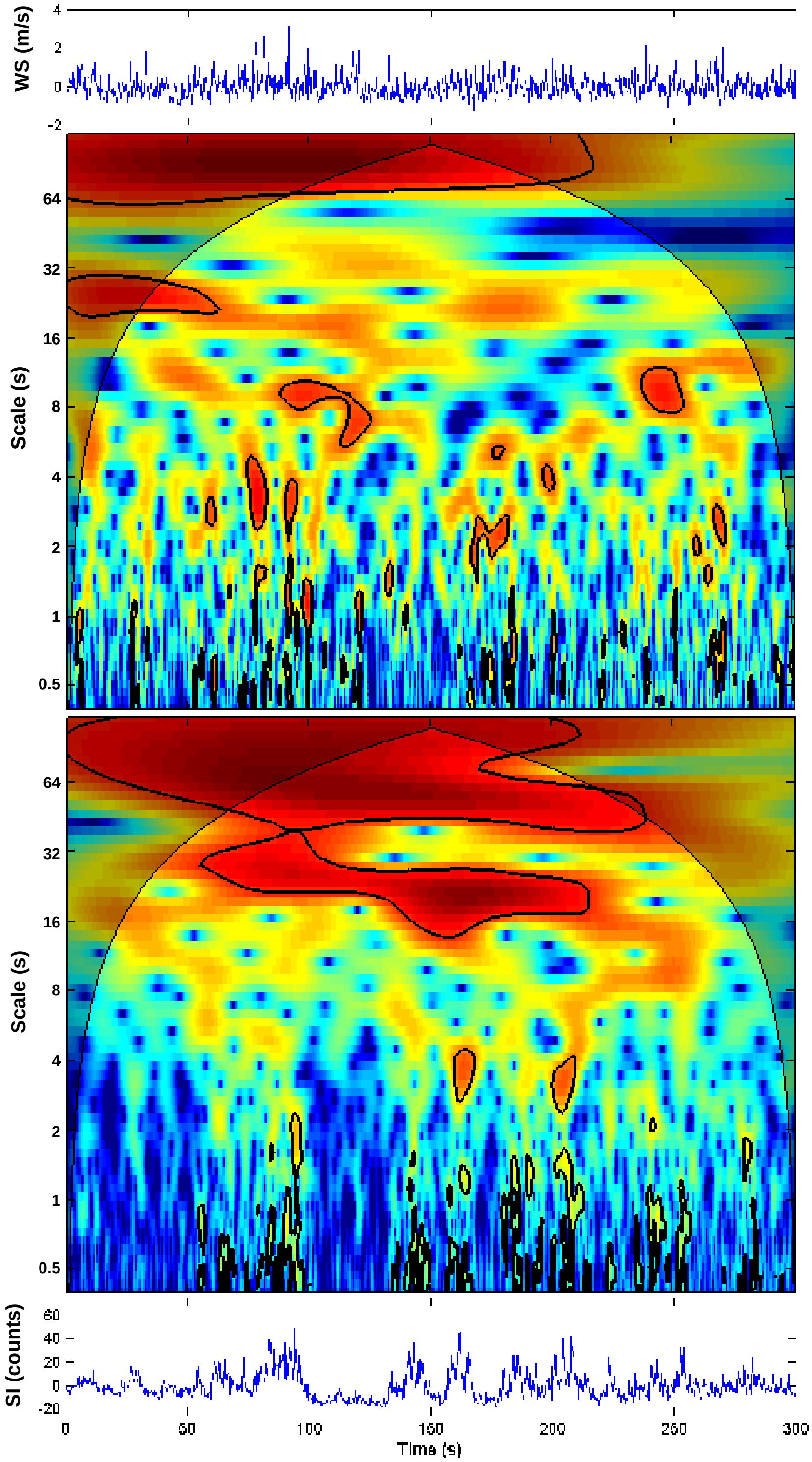

Fig. 5-18. Continuous wavelet transform wavelet map using a Morlet wave base for Run 5, wind (top wavelet map) and saltation (bottom wavelet map). The time series (5 Hz detrended) used in the wavelet analysis are shown above (wind) and below (saltation) the wavelet maps. Colors on the wavelet maps indicate wavelet power intensity. ‘Hotter’ colors (red and orange) indicate higher power and ‘cooler’ colors (blue and cyan) indicate lower power. The bold black lines on the wavelet maps designate regions that are significant at the 5% level (95% confidence interval).

5.6.4 Wind and Saltation Event Detection and Analysis

Significant (at the 5% level) wavelet power coefficients, that also have an equivalent Fourier period less than or equal to three seconds, were isolated from the wavelet maps. The resultant time series were reduced to wind and saltation events using the methods described in §5.6.1. Fig. 5-19 to 5-23 show the 5 Hz demeaned wind time series (A), the wind events (B), the saltation events (C), and the 5 Hz demeaned saltation time series (D). In Figs. 5-19 to 5-23, the magnitude of the events (shown in panels B and C) is not relevant to the event comparison. Where there is an event, the focus is to calculate and determine the duration of the event.

Visual (qualitative) comparison of the wind and sand 5 Hz demeaned time series and the wavelet-derived event time series show a strong correspondence. Increases in the 5 Hz demeaned records are captured in the event time series. Some examples of the strong correspondence between the 5 Hz records and the wavelet events are, for the wind: Run 1 at ~175 s, Run 3 at ~ 325 s, and Run 5 at ~175 s, and for the sand: Run 2 at ~160 s and Run 4 at ~200 s.

Table 5-4 shows the number of events and average event spacing (calculated by dividing record length by number of events). The average event spacing across all runs was longer for saltation (6.50 s; standard error = 0.25 s) than for wind (6.10 s; standard error = 0.33 s). The number of events calculated in the wind and saltation were within 10% of each other, except for Runs 2 and 5. During both of these runs there were more wind events, resulting in shorter average event spacings.

The average event duration for the wind and saltation is 1.87 s (standard error = 0.13 s) and 2.10 s (standard error = 0.09 s), respectively. The average standard deviation for the wind (1.55 s) is higher than for saltation (1.45 s). During Run 1, the average wind and saltation event durations were almost equal, 2.17 s and 2.14 s Average event duration of 2.17 s was also calculated for the wind for Runs 1 and 3.

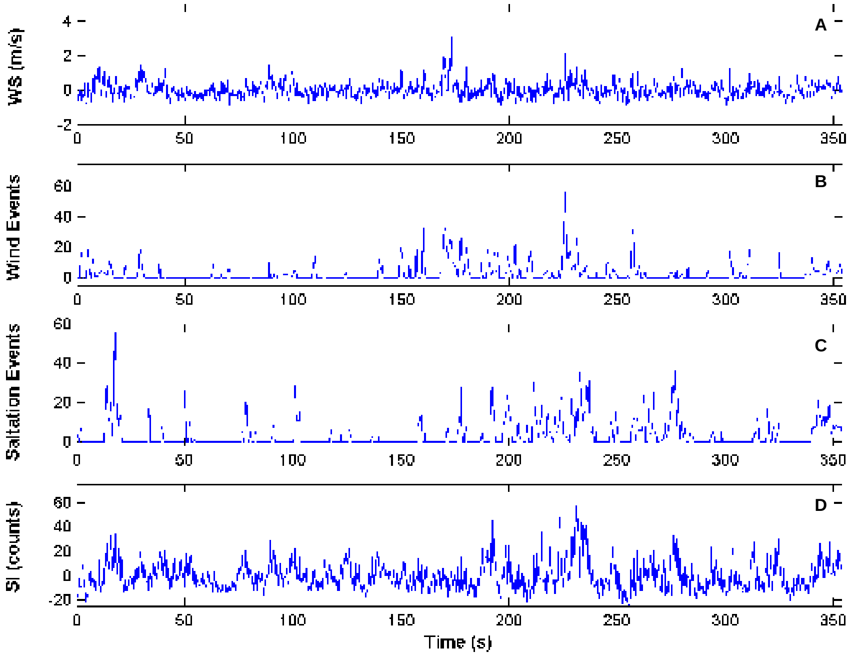

Fig. 5-19. Wavelet wind (B) and sand (C) events and the corresponding 5 Hz demeaned time series, wind speed “WS” (A) and saltation impacts “SI” (D) for Run 1.

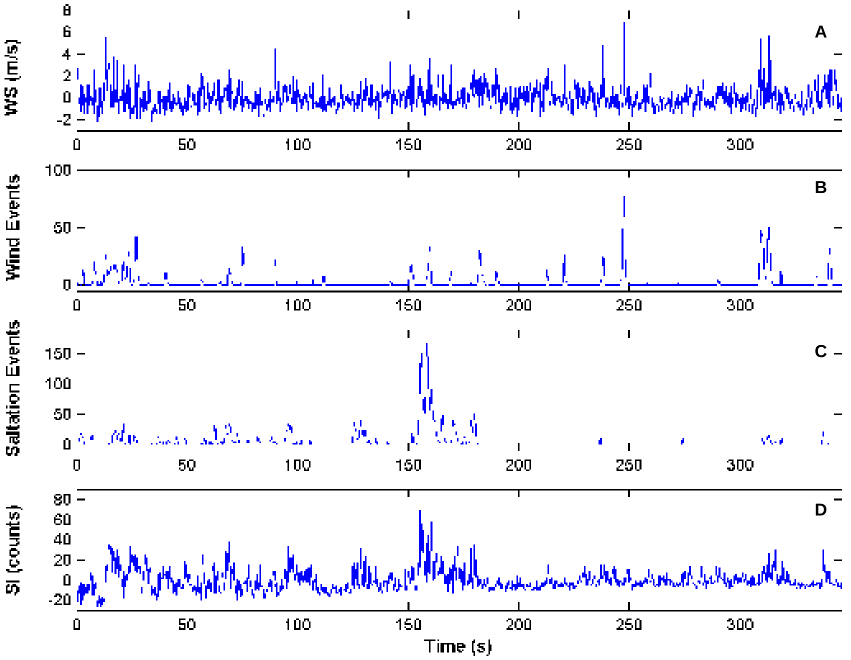

Fig. 5-20. Wavelet wind (B) and sand (C) events and the corresponding 5 Hz demeaned time series, wind speed “WS” (A) and saltation impacts “SI” (D) for Run 2.

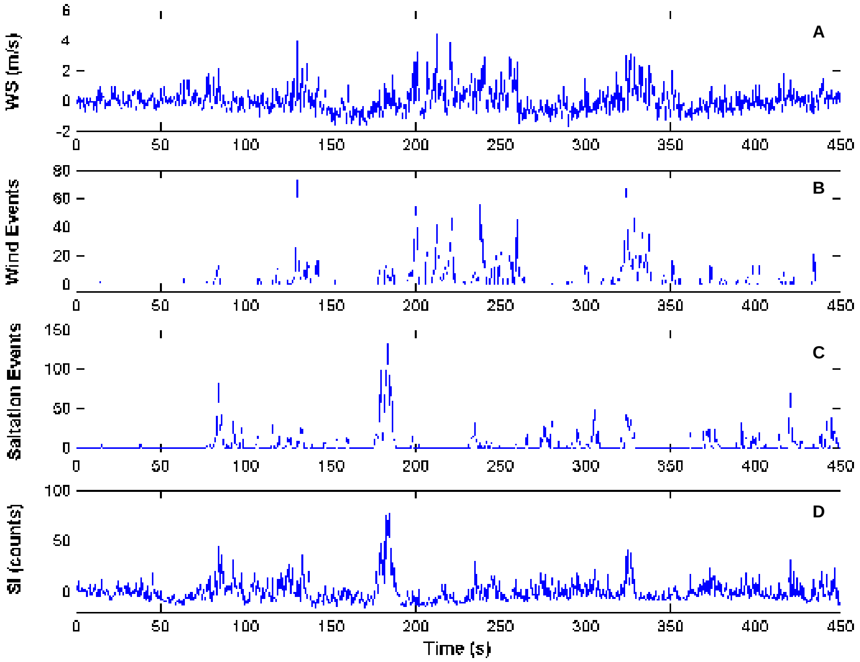

Fig. 5-21. Wavelet wind (B) and sand (C) events and the corresponding 5 Hz demeaned time series, wind speed “WS” (A) and saltation impacts “SI” (D) for Run 3.

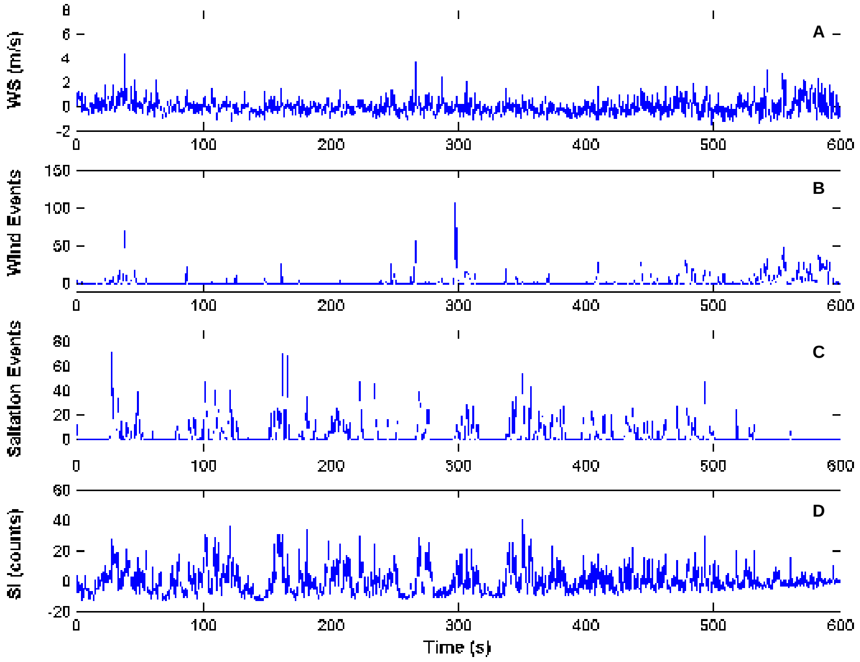

Fig. 5-22. Wavelet wind (B) and sand (C) events and the corresponding 5 Hz demeaned time series, wind speed “WS” (A) and saltation impacts “SI” (D) for Run 4.

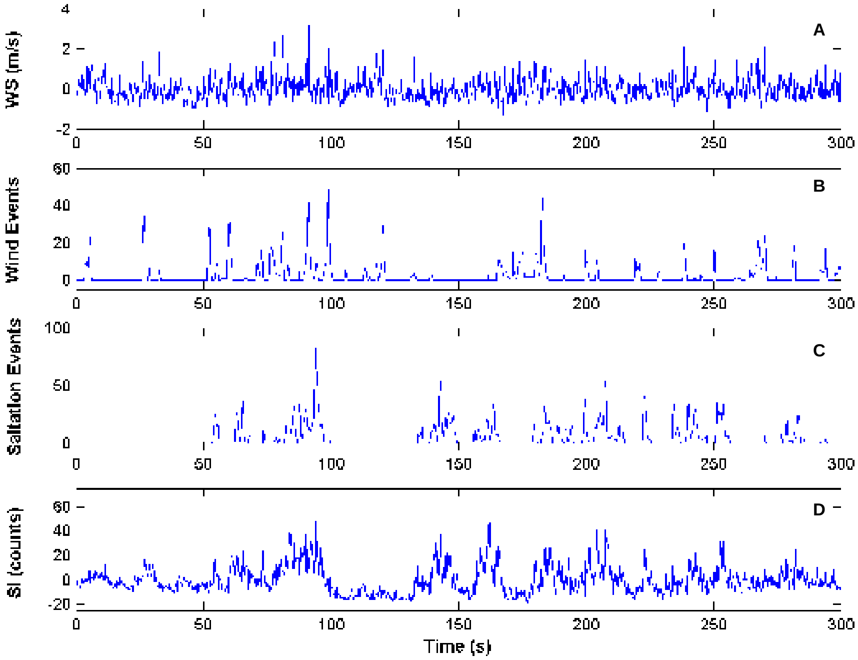

Fig. 5-23. Wavelet wind (B) and sand (C) events and the corresponding 5 Hz demeaned time series, wind speed “WS” (A) and saltation impacts “SI” (D) for Run 5.

Table 5-4. Number of events, average event spacing, average event duration, and the standard deviation for the average event duration for wind and saltation.

		Wind				**Saltation**			
	Record Length (s)	**Events**	**Event Spacing (s)**	**Average Duration (s)**	**Std (s)**	**Events**	**Event Spacing (s)**	**Average Duration (s)**	**Std (s)**
Run 1	354	63	5.62	2.17	2.36	60	5.90	2.14	1.51
Run 2	346	62	5.58	1.51	1.08	48	7.21	2.02	1.42
Run 3	450	62	7.26	2.17	1.79	68	6.62	1.89	1.59
Run 4	600	94	6.38	1.73	1.40	101	5.94	2.03	1.04
Run 5	300	53	5.66	1.79	1.11	44	6.82	2.40	1.65
Avg.			*6.10*	*1.87*	*1.55*		*6.50*	*2.10*	*1.44*

5.7 Cross Continuous Wavelet Transform

5.7.1 Methods

The cross continuous wavelet transform was used to find synchronous events in the wind and saltation fields. Power wavelet coefficients ($W_{b_{12}}$) were calculated using Eq. 2-19. Statistically significant regions (at the 5% level) and the Cone of Influence (§5.6.1) were graphed on the wavelet maps. Significant regions found within the small wavelet scales (less than or equal to an equivalent Fourier period of 3.0 seconds) were selected to discern events and calculate event durations (c.f., §5.6.1).

5.7.2 Cross Wavelet Maps

The wavelet maps showing the cross power wavelet coefficients are shown in Figs. 5-24 to 5-28. In general, the cross wavelet maps showed similar patterns observed by the wind and sand wavelet maps (§5.6.3), primarily that the significant (at the 95% confidence interval) wavelet regions at the small wavelet scales (≤ 3 s) correspond with increases in the time series. The individual cross wavelet maps for Runs 1-5 are discussed below.

Between ~40-75 s and ~100-150 s, there are few regions within Run 1 cross wavelet map (Fig. 5-24) that are significant (defined here using the 95% confidence interval) at scales smaller than 30. The corresponding time series shows that the signal is reduced during these periods. However, between ~150-275 s, the time series increases, the wavelet power increases, there is significance at the smaller scales (showing the details of the signal fluctuations), and there is significance at the larger scales (showing the larger trends of the signal).

The Run 2 cross wavelet map (Fig. 5-25) shows that there is a large amount of significance between 0-175 s, especially at wavelet scales around 32 s, and there is almost no significance toward the end of the record. The corresponding time series shows the same patterns found on the wavelet map.

The beginning (0-75 s) of the Run 3 cross wavelet map (Fig. 5-26) has a small amount of wavelet power, corresponding with a reduced, signal in the corresponding time series. The significant regions occurring at the smaller scales occur at approximately 80 s, 140 s, 180 s, 240 s, and 330 s, and correspond with the largest peaks in the time series.

The cross wavelet map for Run 4 (Fig. 5-27) reveals that there are significant regions at the small wavelet scales throughout the entire time series. There are no high-powered significant events at the large wavelet scales that persist for most of the run (similar to what is observed in Run 3, Fig. 3-26).

There are two periods Run 5 (Fig. 5-28) that show almost no significance at the small wavelet scales (<3 s), at ~0-55 s and at ~100-140 s, during cross wavelet analysis. There is a period of significance at the small scales between ~55-100 s that corresponds with an increase in the time series.

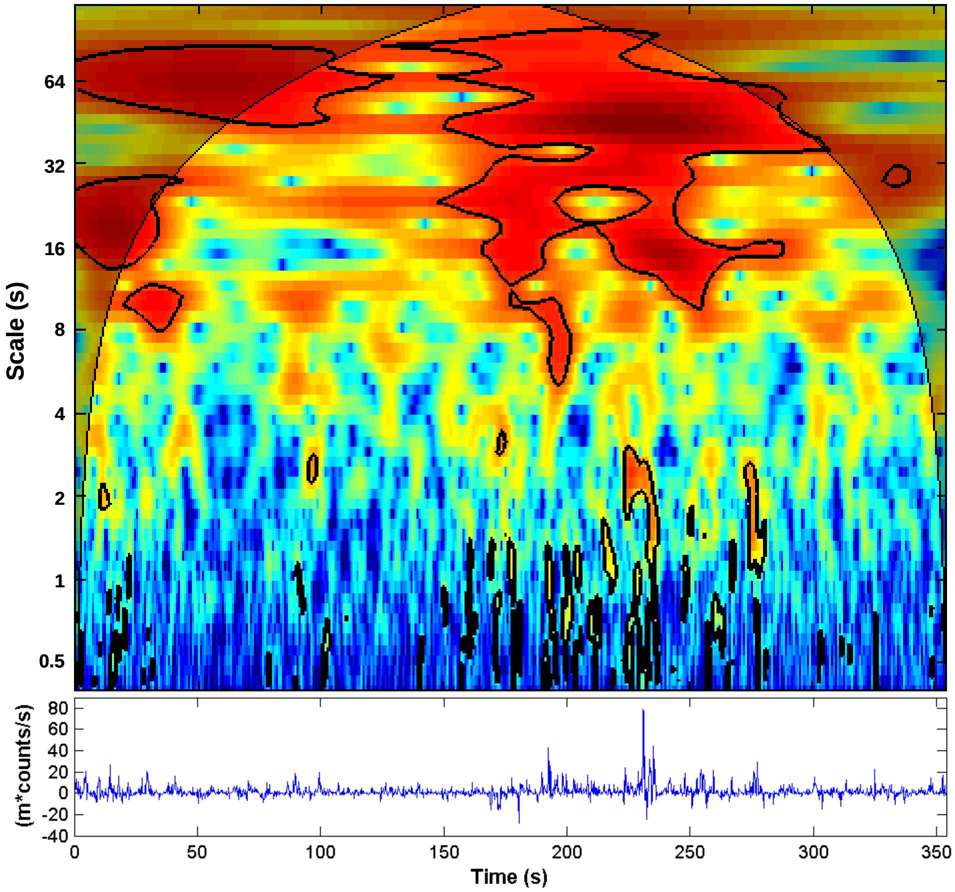

Fig. 5-24. The complex conjugate of wind and sand 5 Hz demeaned time series from Run 1 (bottom) and the corresponding wavelet map (top). Colors on the wavelet map indicate wavelet power intensity. ‘Hotter’ colors (red and orange) indicate higher power and ‘cooler’ colors (blue and cyan) indicate lower power. The bold black lines on the wavelet map designate regions that are significant at the 5% level (95% confidence interval).

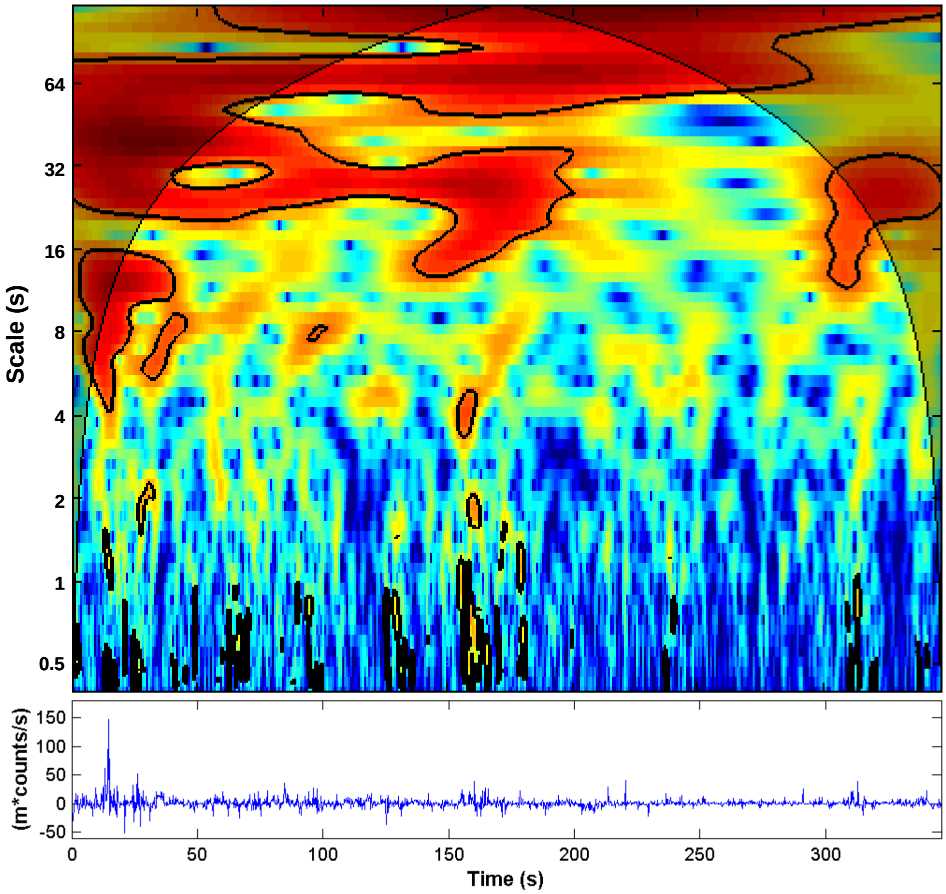

Fig. 5-25. The complex conjugate of wind and sand 5 Hz demeaned time series from Run 2 (bottom) and the corresponding wavelet map (top). Colors on the wavelet map indicate wavelet power intensity. ‘Hotter’ colors (red and orange) indicate higher power and ‘cooler’ colors (blue and cyan) indicate lower power. The bold black lines on the wavelet map designate regions that are significant at the 5% level (95% confidence interval).

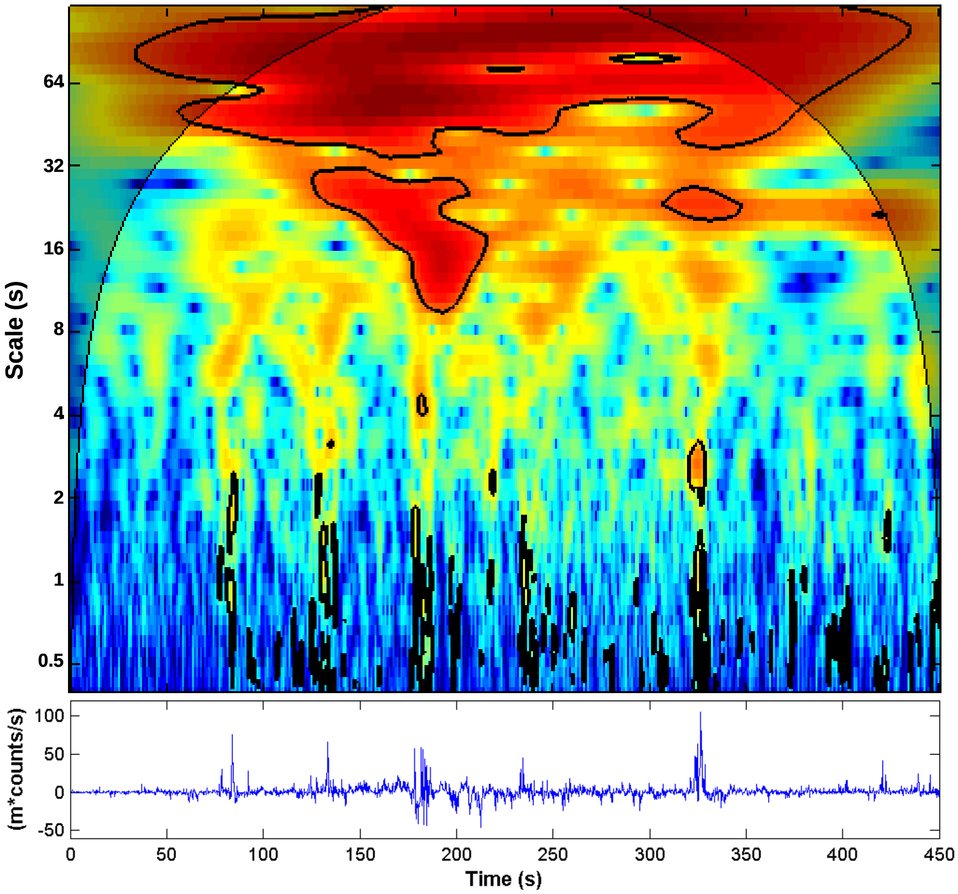

Fig 5-26. The complex conjugate of wind and sand 5 Hz demeaned time series from Run 3 (bottom) and the corresponding wavelet map (top). Colors on the wavelet map indicate wavelet power intensity. ‘Hotter’ colors (red and orange) indicate higher power and ‘cooler’ colors (blue and cyan) indicate lower power. The bold black lines on the wavelet map designate regions that are significant at the 5% level (95% confidence interval).

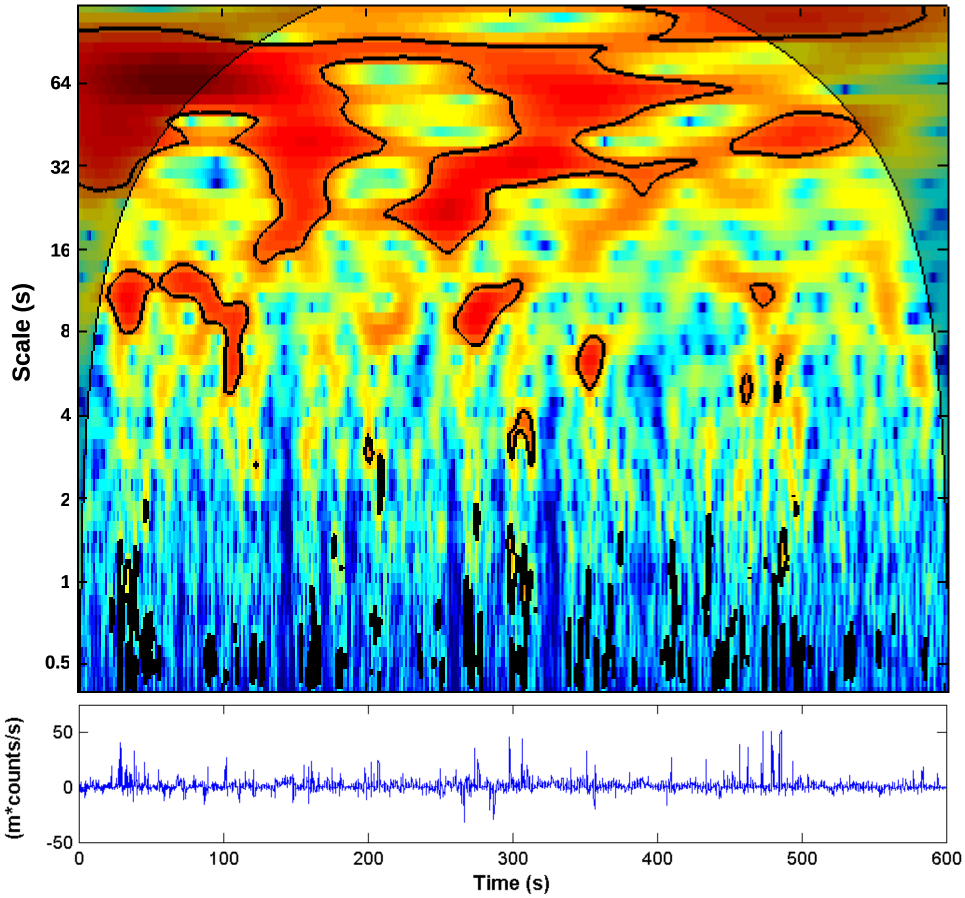

Fig. 5-27. The complex conjugate of wind and sand 5 Hz demeaned time series from Run 4 (bottom) and the corresponding wavelet map (top). Colors on the wavelet map indicate wavelet power intensity. ‘Hotter’ colors (red and orange) indicate higher power and ‘cooler’ colors (blue and cyan) indicate lower power. The bold black lines on the wavelet map designate regions that are significant at the 5% level (95% confidence interval).

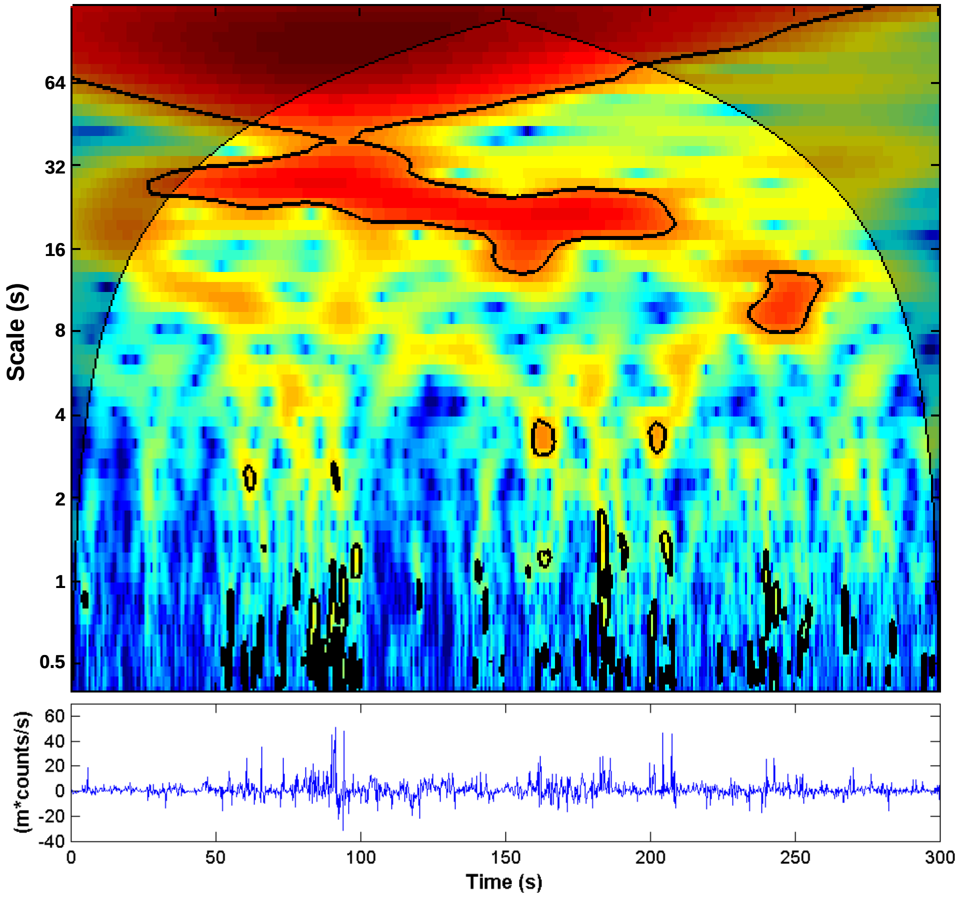

Fig. 5-28. The complex conjugate of wind and sand 5 Hz demeaned time series from Run 5 (bottom) and the corresponding wavelet map (top). Colors on the wavelet map indicate wavelet power intensity. 'Hotter' colors (red and orange) indicate higher power and 'cooler' colors (blue and cyan) indicate lower power. The bold black lines on the wavelet map designate regions that are significant at the 5% level (95% confidence interval).

5.7.3 Cross Event Detection and Analysis

The cross wavelet events are shown in Figs. 5-29 to 5-33. Similar to Figs. 5-19 to 5-23, the magnitudes of the events are not the focus this analysis; the event locations and durations are the focus. The top panel (A) of Figs. 5-29 to 5-33 shows the complex conjugate of the wind and saltation time series for visual comparison with the cross events. As described in §2.5.3, the cross wavelet is calculated by considering the complex conjugate of the wavelet coefficients of the wind and saltation, not by the continuous wavelet analysis of the time series presented in Figs. 5-29 to 5-33. However, there is strong correspondence between the wind-sand time series and the cross events in Figs. 5-29 to 5-33.

Cross wavelet events were selected from the wavelet maps using the same criterion established for the wind and saltation events (§5.6.4). Cross event spacing was calculated by dividing record length by number of events. The event characteristics from the cross wavelet analysis are shown in Table 5-5.

The average duration of the cross events is 1.73 s (standard error = 0.06 s) and the average event spacing is 6.72 s (standard error = 0.41 s) (both shown in Table 5-5). Runs 2 and 5 had the shortest average event duration (1.60 s), yet Run 1 had the shortest average event spacing (5.45 s). The average event duration of all runs ranged from 1.60 to 1.88 seconds.

The values correspond well with those calculated using continuous wavelet transform of the wind and saltation time series (Table 5-4). The average duration for the cross events was the shortest and the event spacing the longest.

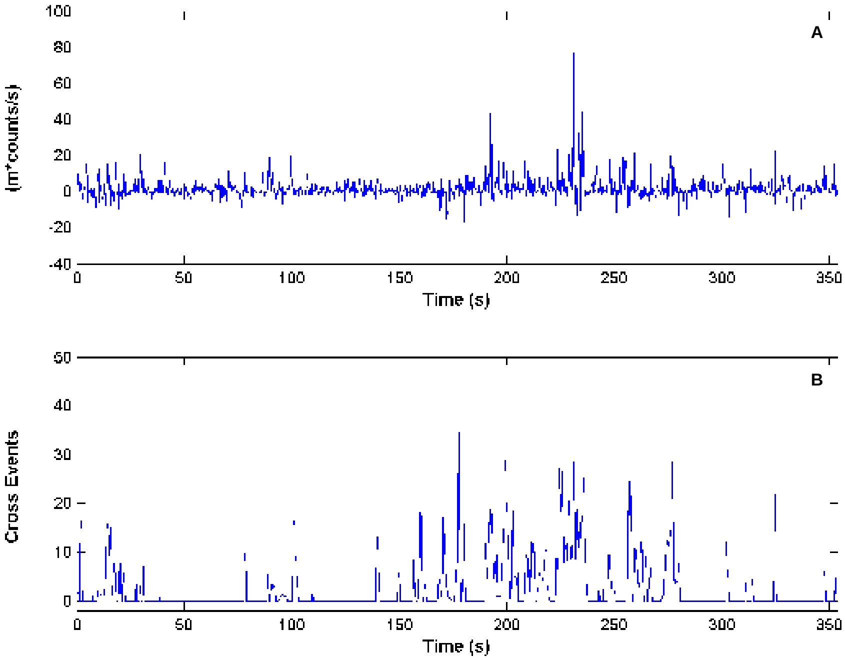

Fig. 5-29. The complex conjugate of the wind and sand 5 Hz demeaned time series from Run 1 (A) and the corresponding cross wavelet events (B).

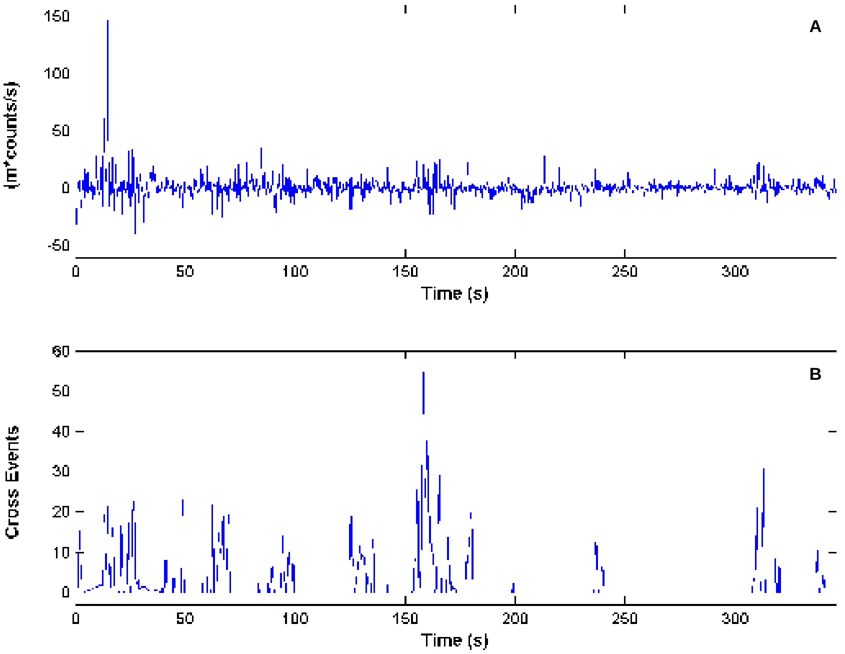

Fig. 5-30. The complex conjugate of the wind and sand 5 Hz demeaned time series from Run 2 (A) and the corresponding cross wavelet events (B).

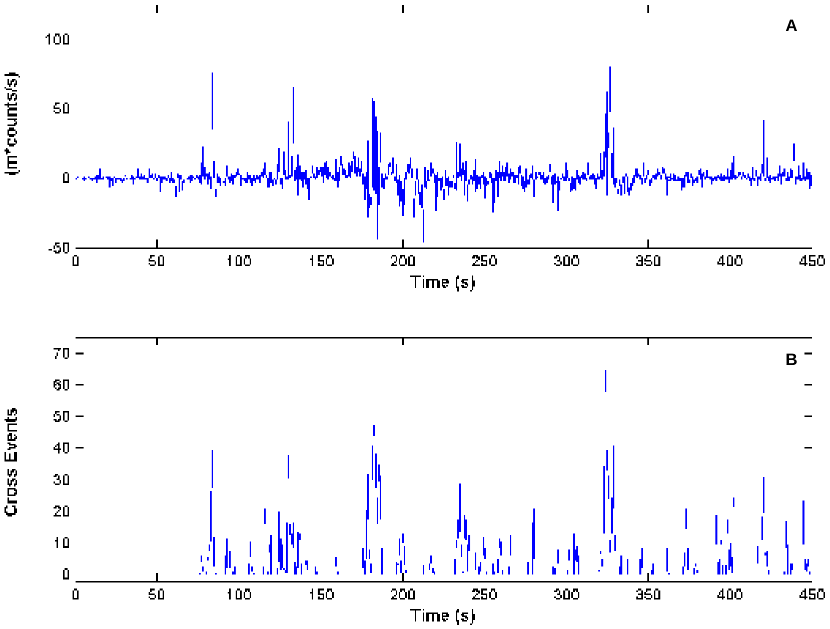

Fig. 5-31. The complex conjugate of the wind and sand 5 Hz demeaned time series from Run 3 (A) and the corresponding cross wavelet events (B).

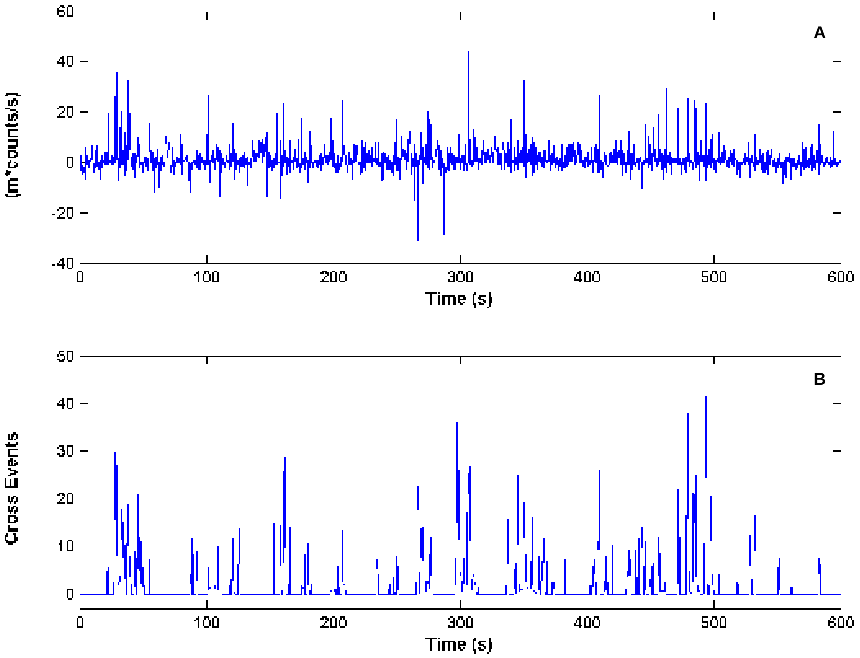

Fig. 5-32. The complex conjugate of the wind and sand 5 Hz demeaned time series from Run 4 (A) and the corresponding cross wavelet events (B).

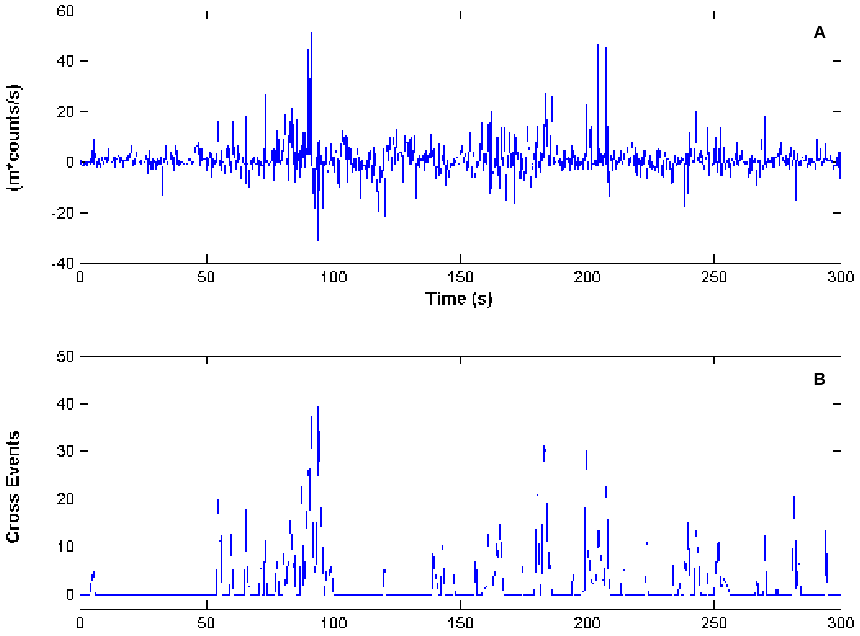

Fig. 5-33. The complex conjugate of the wind and sand 5 Hz demeaned time series from Run 5 (A) and the corresponding cross wavelet events (B).

Table 5-5. Number of cross wavelet events, average event spacing, average event duration, and the standard deviation for the average event duration for each run.

		Cross			
	Record Length (s)	**Events**	**Event Spacing (s)**	**Average Duration (s)**	**Std (s)**
Run 1	354	65	5.45	1.76	1.36
Run 2	346	46	7.52	1.60	0.97
Run 3	450	63	7.14	1.81	1.30
Run 4	600	81	7.41	1.88	1.88
Run 5	300	49	6.12	1.6	1.02
Avg.			*6.73*	*1.73*	*1.31*

6. DISCUSSION

6.1 Section Introduction

In this section the results presented in the data analysis section are discussed. The reason for the longer saltation event duration is explained. Also, it was determined that the event durations calculated in this research corresponded well with event durations calculated in previous studies. Calculations and a scaling analysis are presented to determine the bursting interval using the equation introduced by Rao et al. (1971). The bursting interval estimations are compared to the event duration values estimated from wavelet analysis. A discussion on the cross continuous wavelet method is included. It was found that this method produces false events, therefore it is suggested that cross wavelet is used in addition to wavelet analysis. This section concludes with a discussion on the type and origin of the coherent structures measured during this research.

6.2 Event Duration

The average wind event duration (for all runs) was shorter (1.87 s) than the average saltation event duration (2.10 s) (Table 5-4). The difference in the averages between the wind and saltation is not statistically distinct (p=0.19) when conducting a Student's t-test. However, it is suggested that the longer saltation event duration is because the inertial effects on the sand maintain the sand transport after the wind event has concluded. The effects of inertia were observed during Butterfield's (1998) laboratory study. Jackson (1996) conducted a field project that investigated inertia, specifically periods of saltation occurring at levels below the fluid threshold for motion that followed periods of saltation that took place when the fluid threshold for motion was exceeded. During this dissertation research, it is suggested that the inertial effects acting on the saltation system (discussed by Jackson, 1996) maintained the saltation for 0.2 seconds longer than the wind.

The duration of wind events here correspond well with event durations estimated by others, summarized in Table 6-1. The average duration (1.87 s) reported here is within the range of event durations calculated by others, 0.1 to 4.7 s. Leenders et al. (2005: 370) indicated that their values were "estimated" and that the event duration was primarily "explained by sampling frequency." The VITA method was employed by Baas (2003) to calculate event durations, however, he did not completely explain his methods. The 'traditional' VITA equations (Eqs. 2-11 to 2-15) do not provide estimates of event duration and he does not describe how his calculations were completed. Event detection methods were also not clearly defined in the Sterk et al. (1998) study.

Table 6-1. Wind event durations estimated in previous studies.

	Event Duration (s)	Comments
Sterk et al. (1998)	1.0 - 1.42	1 Hz sample rate
Baas (2003)	1.3 - 4.7	VITA-estimated, 5 Hz sample rate (his Table 6-5)
Leenders et al. (2005)	0.1	16 Hz sample rate, value “estimated” (p. 370)
Leenders et al. (2005)	0.2	8 Hz sample rate, value “estimated” (p. 370)

The saltation and wind event durations correspond well with the integral time scales calculated by the normal autocorrelation function (§5.5.1) and the power spectral density (§5.5.2) analyses. Table 6-2 shows the normal autocorrelation function and spectral-estimated integral time scales and the average event durations calculated using continuous wavelet transform for wind and saltation. Kaimal and Finnigan (1994: 35) define integral time scale as the scale “over which the turbulence remains correlated.” A two second integral time scale for the wind indicates that the turbulence, i.e., coherent structures (c.f., Robinson (1991a) definition of coherent structure in §2.2.3), measured in the wind had a temporal scale of two seconds. A wavelet-derived event duration of about two seconds reinforces the notion that the events that were measured were coherent structures.

Table 6-2. Summary of average integral time scales derived using the normalized autocorrelation function (NACF) and power spectral density analysis for the wind and saltation. These values can be compared to the average event durations derived from wavelet analysis.

	Integral Time Scale		Event Duration
	NACF (s)	Spectral Density (s)	Wavelet-derived (s)
Wind	1.84	1.56	1.87
Saltation	2.14	1.65	2.10

6.3 Event Spacing

Using the empirical scale relationship presented by Rao et al. (1971) (Eq. 2-7) and the data collected in this experiment, the mean bursting interval (mean burst period) was estimated. If the results of Rao et al.'s (1971) equation show strong similarities to the average event durations calculated herein (Table 5-4), it can be strongly suggested that the bursting was present during this research. Several calculations are necessary to solve Eq. 2-7, and are presented below.

It was briefly mentioned in §3.5 that this research was part of a larger field project. In that project, a thermal anemometer tower was deployed during Run 3 (shown in Figs. 3-9 and 3-10) with instruments at 0.02, 0.06, 0.12, and 0.20 meters above the bed. The thermal anemometer records were calibrated using methods outlined in §4.3.2 and the velocity profiles were derived employing 'method 1' from Bauer et al. (1998), excluding the anemometer at 0.02 m. The r^2 value for the velocity profile was 98.3%. Shear velocity (u_*) and roughness length (z_0) were calculated using the regression equations of the velocity profiles (method 1: Bauer et al., 1998). The roughness length was 0.67 mm and the u_* value was 0.32 m/s.

Boundary layer height (or thickness, δ) was estimated using Granger et al.'s (2006) equation for an internal boundary layer with roughness lengths ranging between 0.002-0.005 m:

$$\delta = 0.18x^{0.62} \tag{6-1}$$

where x is horizontal (streamwise) distance of the boundary layer, which was 125 m. (distance from the river to the instrument array, Fig. 3-1). Internal boundary layers are formed with a change in surface roughness. The internal boundary layers discussed in §2.2.3 (Fig. 2-5) are present 'inside' the internal boundary layers discussed here that are initiated from the fluid flowing over water (the Shoalhaven River) to sand. Granger et al. (2006) do not present an equation for roughness lengths less than 0.002 m. They report that internal boundary layer growth rates decrease with decreasing roughness lengths, therefore, the 3.6 m boundary layer height calculated using Eq. 6-1 may be slightly overestimated. Free stream velocity (U_∞) was calculated with the "law of the wall" (Eq. 2-1), using $\kappa = 0.4$, $z_0 = 0.00067m$, $u_* = 0.32m/s$, and $z = 3.6m$ (equivalent to the height of the internal boundary layer, estimated using Eq. 6-1).

A range of T^+ values have been used in previous studies, and are shown in Table 6-3. Rao et al. (1971) reported that $3 \le T^+ \le 7$, Blackwelder and Kaplan (1976) indicated a T^+ of ten, and a T^+ value of 19 can be estimated from Blackwelder and Haritonidis (1983). The dimensionless time from Blackwelder and Haritonidis (1983) is a maximum estimated from a range of T^+ values presented in their Fig. 10. The first row of data in Table 6-3 presents the bursting periods using

$u_* = 0.32 m/s$ and $U_\infty = 6.87 m/s$. The middle and bottom rows present bursting periods if the shear velocity was decreased (middle row) or increased (bottom row) by 15%. Table 6-3 indicates that the most sensitive portion of Eq. 2-7 the selection of T^+, not U_∞ (noting that, in this case, U_∞ is depended on u_* because U_∞ is calculated using Eq. 2-1).

Table 6-3 shows that for the conditions measured during this study, the potential bursting periods range between 1.37 and 11.72 seconds. The range of average event spacing from this research was 5.62 and 7.26 seconds (average = 6.10 s, Table 5-4). If a dimensionless time of ten (T^+=10) is selected (Blackwelder and Kaplan, 1976), the bursting range is between 4.56 and 6.17 s. These bursting periods correspond well with the average event spacing estimated using the wavelet method (Table 5-4) and suggest that bursting occurring during this experiment. The average event spacing for saltation was 6.50 s, indicating synchronization between the wind and saltation. The temporal correspondence between the two records also suggests that the driving mechanism for the saltation event measured herein was the bursting.

Bursting intervals presented in Table 6-4 were calculated by employing Granger et al.'s (2006) equation to estimate internal boundary layer thickness (Eq. 6-1). An analysis was completed to determine the sensitivity of the bursting interval values (*T*) on boundary layer thickness. Additional equations to calculate internal boundary layer height, presented by Elliot (1958), Brutsaert (1982), Pendergrass and Aria (1984), and Jegede and Foken (1999) were considered. Table 6-4 shows the results of this analysis, assuming a roughness length of 0.00067 m, and $u_* = 0.32 m/s$ (and the $\pm 15\%$ shear velocity range). The results for Pendergrass and Aria (1984) are not presented because they are within a few percent of those found with the Granger et al. (2006) model. The highest estimated internal boundary layers (Brutsaert, 1992) are presented in the top rows in Table 6-4 and the lowest estimated boundary layers (Granger et al., 2006) are presented in the bottom rows. As the internal boundary layer height increases, the bursting interval increases. Fig. 6-1 is a graph of the data presented in Table 6-4. The bold horizontal line on Fig 6-1 is drawn at 6.10 seconds, which is the average event spacing for the wind (Table 5-4). The vertical lines on Fig. 6-1 are drawn at $T^+ = 3$ and $T^+ = 7$ to indicate the dimensionless time range that was suggested by Rao et al. (1971).

Table 6-3. Bursting interval estimations using various values of dimensions time (T^+) and a range (±15%) of shear velocity (u_*) that influences free stream velocity (U_∞) using the Granger et al. (2006) model to estimate internal boundary layer height. Roughness length (z_0) was kept constant in all the calculations.

				Using T^+ (dimensionless) values of…T (in seconds) equals						
	z_0 (m)	**u_* (m/s)**	**U_∞ (m/s)**	**3**	**4**	**5**	**6**	**7**	**10**	**19**
	0.00067	0.32	6.87	1.57	2.10	2.62	3.15	3.67	5.24	9.96
u_* -15%		0.27	5.84	1.85	2.47	3.08	3.70	4.32	6.17	11.72
u_* +15%		0.37	7.90	1.37	1.82	2.28	2.74	3.19	4.56	8.66

It is evident that selection of the model to estimate internal boundary layer height strongly influences the predicted bursting interval. However, considering the models of Elliot (1958), Brustaert (1982), Jegede and Foken (1999), and Granger et al. (2006), the results from the average event duration calculated in this research (6.10 s) fit into every range of model estimations, including the ±15% shear velocity boundaries (with exception to Brustaert (1982) T^+= 3 (-u_* 15%)). Using the models of Brutsaert (1982) and Elliot (1958) the optimal dimensionless time (T^+) is four. The Jegede and Foken (1999) and Granger et al. (2006) models point toward an optimal T^+ of ten. Averaging the optimal dimensionless time values from the four models presented in Table 6-4 reveals and average of seven. These results are within the ranges reported by Rao et al. (1971) and within the ranges presented by Kostaschuck et al. (1991) and Kostaschuck and Church (1993) ($3 < T^+ < 7$), in their field-based investigations.

Table 6-4. Bursting interval estimations using various values of dimensions time (T^+), four different models to calculate boundary layer height (Brustaert, 1982; Elliot, 1958; Jegede and Foken, 1999; and Granger et al., 1999), and a range (±15%) of shear velocity (u_*) that influences free stream velocity (U_∞). Roughness length (z_0) was kept constant in all the calculations.

				Using T^+ (dimensionless) values of…T (in seconds) equals						
	z_0 (m)	**u_* (m/s)**	**U_∞ (m/s)**	**3**	**4**	**5**	**6**	**7**	**10**	**19**
Brutsaert (1982)	0.00067	0.32	7.94	5.21	6.95	8.69	10.43	12.16	17.38	33.02
u_*-15%		0.27	6.75	6.13	8.18	10.22	12.27	14.31	20.44	38.84
(δ=13.8m) u_*+15%		0.37	9.13	4.53	6.04	7.56	9.07	10.58	15.11	28.71
Elliot (1958)	0.00067	0.32	7.76	4.25	5.67	7.09	8.50	9.92	14.17	26.93
u_*-15%		0.27	6.60	5.00	6.67	8.34	10.01	11.67	16.68	31.68
(δ=11.0m) u_*+15%		0.37	8.92	3.70	4.93	6.16	7.40	8.63	12.33	23.42
Jegede and Foken	0.00067	0.32	7.01	1.84	2.45	3.07	3.68	4.29	6.14	11.66
(1999) u_*-15%		0.27	5.96	2.17	2.89	3.61	4.33	5.05	7.22	13.71
(δ=4.3m) u_*+15%		0.37	8.06	1.60	2.13	2.67	3.20	3.73	5.33	10.14
Granger et al. (2006)	0.00067	0.32	6.87	1.57	2.10	2.62	3.15	3.67	5.24	9.96
u_*-15%		0.27	5.84	1.85	2.47	3.08	3.70	4.32	6.17	11.72
(δ=3.6m) u_*+15%		0.37	7.90	1.37	1.82	2.28	2.74	3.19	4.56	8.66

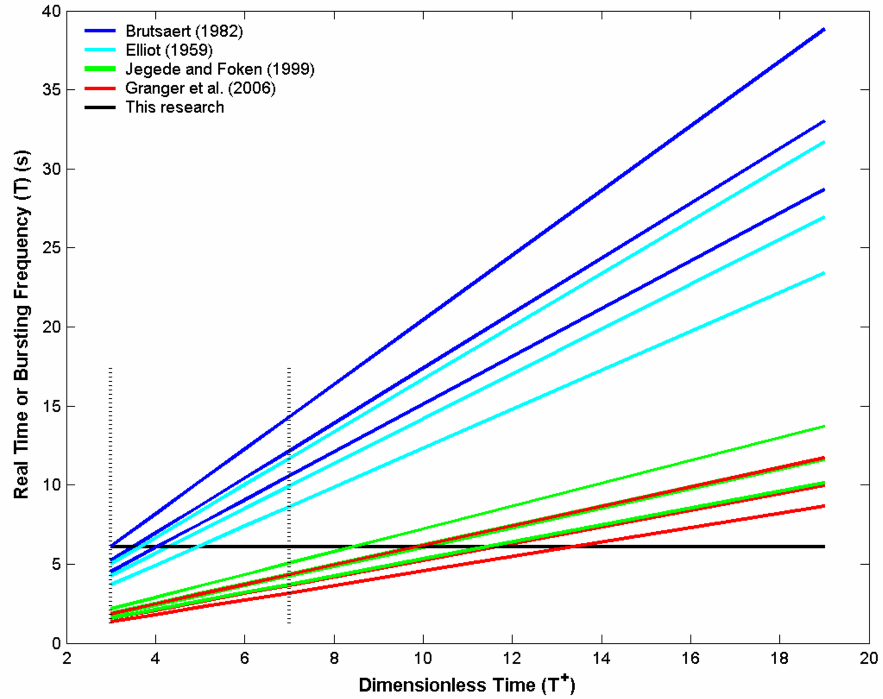

Fig. 6-1. Bursting time interval (*y*-axis) calculated using Rao et al.'s (1971) equation. Various estimations of boundary layer height were incorporated into Rao et al.,'s equation (shown in legend). The bold black line is at 6.10 seconds and is the average event spacing calculated in this research. Vertical lines at T^+=3 and T^+=7 indicate the range of dimensionless time values suggested by Rao et al. (1971).

The values estimated in Table 6-3 correspond fairly well with event durations estimated by others. Kim et al. (1971) reported mean event durations in water of 2.27 seconds when the flow was 0.152 m/s and 6.5 seconds when the flow was 0.076 m/s. Gustavsson and Lende (1980) suggest that event duration increases with increasing surface roughness. If z_0 (Table 6-3) is increased by 100%, the event duration only increases by about 16% percent.

In summary, the average wind event durations from this research using a multi-model analysis to determine internal boundary layer height (Table 6-4) indicate that the T^+ is seven. The correspondence between the estimations from this study and previous works (e.g., Rao et al., 1971) strongly suggest that bursting was present. The temporal correspondence in the saltation event duration suggests that the wind is the forcing agent of the saltation events during this research.

6.4 Cross Continuous Wavelet Method

The cross continuous wavelet method allows synchronous analysis of two data sets and was used in this research to examine matching between the wind and saltation records (research objective 2, §1.4). To the best of my knowledge, this is the only method that allows simultaneous analysis to detect discrete events (using the criterion presented in §5.7) within two data sets.

The event detection results using the cross wavelet method (§5.7.3) were compared to the event detection results using the wavelet method of the wind and saltation records (§5.6.4). Figs. 6-2 and 6-3 shows the wind (A), saltation (B), and cross (C) events from Runs 1 and 5 (these are the same event time series shown in Figs. 5-19, 5-23B/C and Fig. 5-29, 5-33B, re-presented here to see better the relationship between the three event time series).

To calculate the cross continuous wavelet coefficients, the wavelet coefficients from the wind and saltation records were convolved using Eq. 2-18. Ideally, the cross wavelet analysis should discern events only that are coincident to the wind and saltation fields. The mathematical byproduct, and disadvantage, to this process is that there are some instances, for example Run 5 at ~125 s (Fig. 6-2), where there is a large wind event, no corresponding saltation event, and a cross event is indicated. Between ~100-140 s the saltation count is minimal (c.f., the 5 Hz demeaned average (Fig. 4-15)), therefore it is evident that this particular 'cross' event is a 'wind-dominated' cross event.

Event detection using the cross wavelet method will produce 'false' events as a byproduct of the event detection criterion established in this research (small wavelet scale events (<3 seconds) that exceeded the 95% confidence interval (c.f., §5.7)). Considering all the data runs, 40% of the cross events are 'false' events. At approximately 150 seconds during Run 1 (Fig. 6-3) there is a wind event, no saltation event, and a cross event. Fig. 5-14 (5 Hz demeaned saltation time series) shows that around this time the saltation count is increasing. On the Run 1 saltation wavelet map (Fig. 5-14) there is a region around a wavelet scale of four that is fairly intense (shaded yellow). However, this increase in wavelet power is not powerful enough (i.e., is not selected by the 95% confidence interval) and is not at a small enough wavelet scale to be selected by the criterion established here. During Run 1 around 125 s (Fig. 6-3) there is an example where there is a saltation and wind event without a cross event.

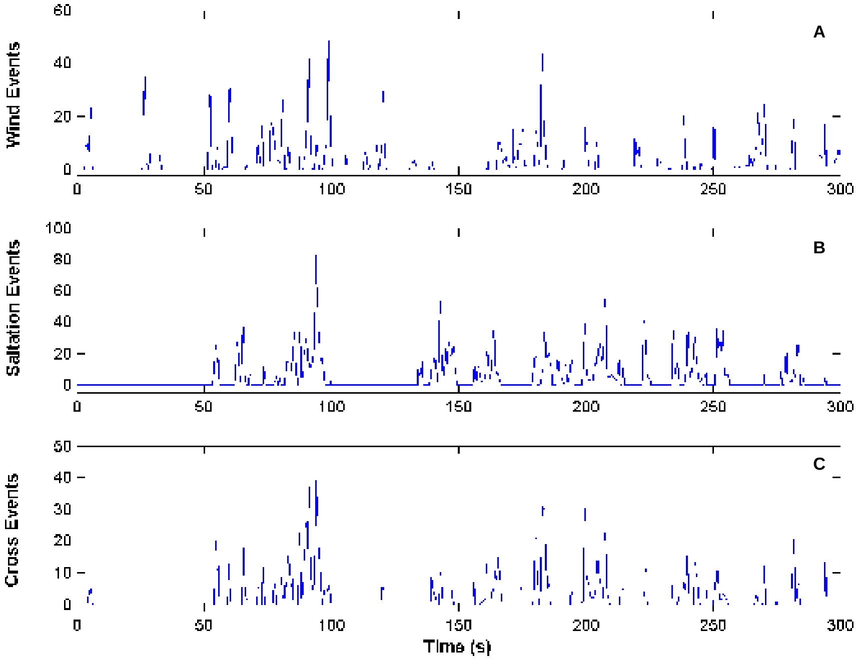

Fig. 6-2. Wind (A), saltation (B), and cross (C) events for Run 5.

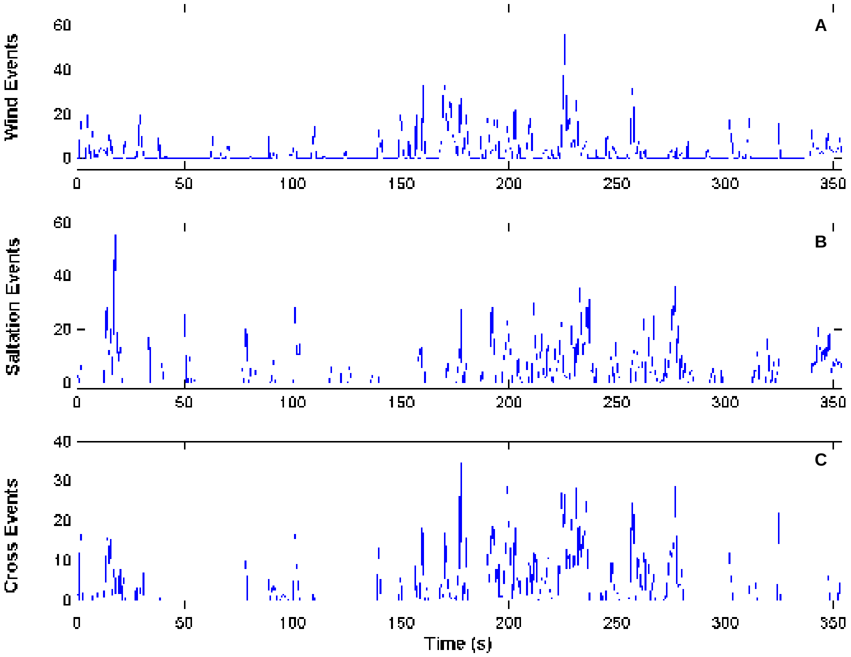

Fig. 6-3. Wind (A), saltation (B), and cross (C) events for Run 1.

6.5 Coherent Structure Formation and Characterization

This research was not designed to discern the origins of quasi-coherent structures. However, it can be inferred whether the structures were originated as ‘bottom-up’ or ‘top-down’ generated processes (Hunt and Morrison, 2000). The events (coherent structures) observed during this research do not scale to ‘bottom-up’ generated bursts initiated by local instabilities (Eq. 2-8, §2.2.3). Using the mean shear velocity (u_*) from Table 6-4 and a kinematic viscosity equaling $1.41*10^{-5}$ m^2/s (at 10°C for air), Eq. 2-8 equals $1.48*10^{-4}$ seconds. This finding strongly suggests that local surface instabilities did not initiate the bursting in the turbulent boundary layer. Negating local surface instabilities as a possible formation mechanism is in conflict with the findings of Schoppa and Hussain (1997) and Jiménez and Penelli (1999) and suggests that the burst and sweep quasi-coherent structures of this origin were not the structures measured during this research. This research suggests that the bursting events (evidenced from §6.3) originated from turbulent eddies formed in the outer portions of the boundary layer, according the ‘top-down’ model proposed by Hunt and Morrison (2000) (Fig. 2-5, §2.2.3).

The agreement between the event durations derived from wavelet analysis and Rao et al.’s equation (Eq. 2-7) provide strong evidence that bursting was present during this research (§6.3). Corino and Brodkey (1969) and Leenders et al. (2005) reported that bursting occurred approximately 20% of the total time of their investigations. During the study presented here, the wind events comprised an average of 17% of the total observations. The agreement between the previous research, in particular Leenders et al. (2005) because their study was field-based, and the study presented here, provides additional evidence to strongly suggest that bursting was measured here.

The turbulent wind events measured during this research had durations of approximately two seconds with concurrent saltation events. The bursting interval measured here was approximately six seconds for the wind-saltation system. Zhou et al. (1999) suggested that the origins of vortical motions were from the top portions of the boundary layer, thus supporting the ‘top-down’ model suggested here. Adrian et al. (2000) indicated that evidence of hairpin vortices are found throughout the boundary layer and Best (1992) linked the presences of hairpin vortices to the unsteadiness observed in sediment transport. The quasi-coherent structures observed during this research are perhaps vortex-shaped.

7. CONCLUSIONS

The experiment described in this dissertation was designed to ascertain if the unsteadiness in the wind field was correlated with the unsteadiness in aeolian transport. The objective of the study was to implement a field experiment to measure the short-term wind and sand transport fluctuations and to analyze the resultant time series for event detection, characterization, and matching. Event duration and spacing, derived from the continuous wavelet transform function, can be used to examine if coherent structures are driving sediment transport and if bursting structures are present in the boundary layer. Through prosecuting this research experiment, the following can be concluded:

1. *Thermal anemometers and miniphones successfully measured short-term fluctuations in wind speed and sand transport close to the bed in a field-based experiment.*
   Co-located thermal anemometers (§3.3.1) and miniphones (§3.3.2) were deployed at elevations between 0.01 and 0.0225 meters above the bed and were 0.02 meters apart on center. The instruments were sampled at 6000 Hz and the resultant time series were calibrated and reduced for data analysis (§4.5).

2. *Wind and saltation events can be discerned using the continuous wavelet transform.*
   There is strong correspondence between increases in the wind and saltation time series and the wavelet maps (§5.6.3). A Morlet wavelet base was employed in this study. A criterion was established to discern events, wavelet coefficients had to be significant at the 95% confidence level and be less than or equal to an equivalent Fourier period of three seconds.

3. *Wind and saltation events were temporally characterized.*
   The wind and saltation events derived from the continuous wavelet transform had durations of approximately two seconds and the event spacing was approximately six seconds (Table 5-4).

4. *Coherent structures (bursting events) were identified and are driving sediment transport.*
   Comparing event durations measured in this research to field-based evidence and empirical-based equations strongly suggest that bursting was present during this research (§6.3). Integral time scales and the event durations for wind and saltation approximate

two seconds (Table 6-2). The temporal coincidence of wind and saltation strongly indicates that the wind is driving sediment transport.

This research showed that there is a strong relationship between wind and saltation events and that this relationship can be established using quantitative methods, specifically the continuous wavelet transform. The conclusion that aeolian transport is event-driven debunks the temporal uniformity that is assumed throughout aeolian transport models (§1.2). Event-driven transport should be included with other factors, such as moisture and slope, as potential explanations for poor model performance, when compared with field-based measurements of sand transport rates (c.f., Sherman et al., 1998). The findings from this research may contribute to reducing the discrepancies found between the field and model predictions of sand transport. This research also contributes to the literature on intermittent saltation (c.f., Stout and Zobeck, 1997) because it indicates that transport is not constant.

REFERENCES

Adrian, R.J., Meinhard, C.D. and Tomkins, C.D., 2000. Vortex organization in the outer region of the turbulent boundary layer. Journal of Fluid Mechanics, 422: 1-54.

Anderson, R.S. and Haff, P.K., 1988. Simulation of eolian saltation. Science, 241: 820-823.

Anderson, R.S. and Haff, P.K., 1991. Wind modification and bed response during saltation of sand in air. In: O.E. Barndorff-Nielsen and B.B. Willets (Editors), Aeolian Grain Transport 1: Mechanics. Acta Mechanica Supplement 1. Springer-Verlag, Wien, pp. 21-52.

Antonia, R., Cahambers, A., Britz, D. and Brown, L., 1986. Organized structures in a turbulent plane jet: topology and contribution to momentum and heat transfer. Journal of Fluid Mechanics, 172: 211-229.

Australian Government Bureau of Meteorology, 2004. Observations for Nowra RAN Air Station AWS, Site Number 68072, WMO Number 94750, 3-4 August.

Baas, A.C.W., 2003. The formation and behavior of aeolian streamers. Ph.D. Thesis, University of Southern California, Los Angeles, 412 pp.

Baas, A.C.W., 2004. Evaluation of saltation flux impact responders (Safires) for measuring instantaneous aeolian sand transport intensity. Geomorphology, 59(1-4): 99-118.

Baas, A.C.W., 2006. Wavelet power spectra of aeolian sand transport by boundary layer turbulence. Geophysical Research Letters, 33: L05403.

Baas, A.C.W. and Sherman, D.J., 2005. Formation and behavior of aeolian streamers. Journal of Geophysical Research, 110: F03011.

Bagnold, R.A., 1936. The movement of desert sand. Proceedings of the Royal Society of London. Series A, Mathematical and Physical Sciences, 157: 594-620.

Bagnold, R.A., 1941. The Physics of Blown Sand and Desert Dunes. Chapman and Hall, London, 256 pp.

Bauer, B.O. and Namikas, S.L., 1998. Design and field test of a continuously weighing, tipping-bucket assembly for aeolian sand traps. Earth Surface Processes and Landforms, Technical and Software Bulletin, 23: 1171-1183.

Bauer, B.O., Houser, C.A. and Nickling, W.G., 2004. Analysis of velocity profile measurements from wind-tunnel experiments with saltation. Geomorphology, 59: 81-98.

Bauer, B.O., Yi, J., Namikas, S.L. and Sherman, D.J., 1998. Event detection and conditional averaging in aeolian systems. Journal of Arid Environments, 39(3): 345-375.

Best, J.L., 1992. On the entrainment of sediment and initiation of bed defects: insights from recent developments within turbulent boundary layer research. Sedimentology, 39: 797-811.

Best, J.L., 1993. On the interactions between turbulent flow structure, sediment transport and bedform development: some considerations from recent experimental research. In: N.J. Clifford, J.R. French and J. Hardisty (Editors), Turbulence: Perspectives on Flow and Sediment Transport. John Wiley & Sons Ltd., Chichester, pp. 62-92.

Blackwelder, R.F. and Haritonidis, J.H., 1983. Scaling of the bursting frequency in turbulent boundary layers. Journal of Fluid Mechanics, 132: 87-103.

Blackwelder, R.F. and Kaplan, R.E., 1976. On the wall structure of the turbulent boundary layer. Journal of Fluid Mechanics, 76(1): 89-112.

Blott, S.J. and Pye, K., 2001. GRADISTAT: a grain size distribution and statistics package for the analysis of unconsolidated sediments. Earth Surface Processes and Landforms, 26: 1237-1248.

Bogard, D.G. and Tiederman, W.G., 1986. Burst detection with single-point velocity measurements. Journal of Fluid Mechanics, 162: 389-413.

Brutsaert, W., 1982. Evaporation into the Atmosphere. D. Reidel, Dordrecht, 299 pp.

Butterfield, G.R., 1991. Grain transport rates in steady and unsteady turbulent airflows. In: O.E. Barndorff-Nielsen and B.B. Willets (Editors), Aeolian Grain Transport 1: Mechanics. Acta Mechanica Supplement 1. Springer-Verlag, Wien, pp. 97-122.

Butterfield, G.R., 1993. Sand transport response to fluctuating wind velocity. In: N.J. Clifford, J.R. French and J. Hardisty (Editors), Turbulence: Perspectives on Flow and Sediment Transport. John Wiley & Sons Ltd., Chichester, pp. 305-334.

Butterfield, G.R., 1998. Transitional behaviour of saltation: wind tunnel observations of unsteady winds. Journal of Arid Environments, 39: 377-394.

Butterfield, G.R., 1999a. Application of thermal anemometry and high-frequency measurement of mass flux to aeolian sediment transport research. Geomorphology, 29(1-2): 31-58.

Butterfield, G.R., 1999b. Near-bed mass flux profiles in aeolian sand transport: high-resolution measurements in a wind tunnel. Earth Surface Processes and Landforms, 24: 393-412.

Clifford, N.J. and French, J.R., 1993. Monitoring and modeling turbulent flow: historical and contemporary perspectives. In: N.J. Clifford, J.R. French and J. Hardisty (Editors), Turbulence: Perspectives on Flow and Sediment Transport. John Wiley & Sons, Ltd., Chichester, pp. 1-34.

Collineau, S. and Brunet, Y., 1993. Detection of turbulent coherent motions in a forest canopy part I: Wavelet analysis. Boundary-Layer Meteorology, 65: 357-379.

Corino, E.R. and Brodkey, R.S., 1969. A visual investigation of the wall region in turbulent flow. Journal of Fluid Mechanics, 37: 1-30.

Davidson-Arnott, R.G.D. and Bauer, B.O., 2006. In: Poster titled "Aeolian sediment transport conditions on a beach: II. Thresholds, and high frequency variability" presented at Sixth International Conference on Aeolian Research, 24-28 July 2006, University of Guelph, Guelph, Ontario, Canada.

Davidson-Arnott, R.G.D., Ollerhead, J., Hesp, P.A. and Walker, I.J., 2003. Spatial and temporal variability in intensity of aeolian transport on a beach and foredune. In: R.A. Davis and P.A. Howd (Editors), Coastal Sediments '03. WorldScientific Publishing Corporation and East Meets West Productions, Clearwater, FL, pp. CDROM, ISBN# 981.238.422.7.

Drake, T.G., Shreve, R.L., Dietrich, W.E., Whiting, P.J. and Leopold, L.B., 1988. Bedload transport of fine gravel observed by motion-picture photography. Journal of Fluid Mechanics, 192: 193-217.

Elliot, W.P., 1958. The growth of the atmospheric internal boundary layer. Transactions American Geophysical Union, 39(6): 1048-1054.

Ellis, J.T., 2006. (submitted). Measuring the transport of aeolian sand with a microphone system. Geomorphology.

Farge, M., 1992. Wavelet transforms and their applications to turbulence. Annual Review of Fluid Mechanics, 24: 395-457.

Farrell, E.J. and Sherman, D.J., 2003. Re-assessment of surface-wind systems for aeolian saltation. In: E. Özhan (Editor), Proceedings of the Sixth International Conference on the Mediterranean Coastal Environment, MEDCOAST 03, pp. 1457-1468.

Fox, J.A., 1977. An Introduction to Engineering Fluid Mechanics. MacMillan Press LTD, London, 446 pp.

Gamage, N. and Hagelberg, C., 1993. Detection and analysis of microfronts and associated coherent events using localized transforms. Journal of Atmospheric Science, 50: 750-756.

Gerety, K.M., 1985. Problems with determination of u* from wind-velocity profiles measured in experiments with saltation, International Workshop on the Physics of Blown Sand. Memoirs (Aarhus Universitet. Afdeling for Teoretisk Statistik). Department of Theoretical Statistics, Institute of Mathematics, University of Aarhus, Denmark, pp. 271-300.

Granger, R.J., Essery, R. and Pomeroy, J.W., 2006. Boundary-layer growth over snow and soil patches: field observations. Hydrological Processes, 20: 943-951.

Grass, A.J., 1971. Structural features of turbulent flow over smooth and rough boundaries. Journal of Fluid Mechanics, 50(2): 233-255.

Grass, A.J., 1983. The influence of boundary layer turbulence on the mechanics of sediment transort. In: B.M. Sumer and A. Muller (Editors), Euromech 156: Mechanics of Sediment Transport. A.A. Balkema, Istanbul, pp. 3-17.

Grinsted, A., Moore, J.C. and Jevrejeva, S., 2004. Application of the cross wavelet transform and wavelet coherence to geophysical time series. Nonlinear Processes in Geophysics, 11: 561-566.

Grossmann, A. and Morlet, J., 1985. Decomposition of Functions into Wavelets of Constant Shape and Related Transforms. In: L. Streit (Editor), Mathematics + Physics, Lectures on Recent Results. World Scientific, Singapore, pp. 135-165.

Gustavsson, L.H. and Linde, M., 1980. The gust as a coherent structure in the turbulent boundary layer, Wind Energy Conference. American Institute of Aeronautics and Astronautics, Inc., Boulder, CO, pp. 50-54.

Head, M.R. and Bandyopadhyay, P., 1981. New aspects of turbulent layer structure. Journal of Fluid Mechanics, 107: 297-338.

Hagelberg, C.R. and Gamage, N.K.K., 1994. Structure-preserving wavelet decomposition of intermittent turbulence. Boundary-Layer Meteorology, 70: 217-246.

Hunt, J.C.R. and Carlotti, P., 2001. Statistical structure at the wall of the high Reynolds number turbulent boundary layer. Flow, Turbulence and Combustion, 66: 453-475.

Hunt, J.C.R. and Morrison, J.F., 2000. Eddy structure in turbulent boundary layers. European Journal of Fluid Mechanics B-Fluids, 19: 673-694.

Jackson, D.W.T., 1996. Potential inertial effects in aeolian sand transport: preliminary results. Sedimentary Geology, 106(3-4): 193-201.

Jackson, D.W.T. and McCloskey, J., 1997. Preliminary results from a field investigation of aeolian sand transport using high resolution wind and transport measurements. Geophysical Research Letters, 24(2): 163-166.

Jackson, R.G., 1976. Sedimentological and fluid-dynamic implications of the turbulent bursting phenomenon in geophysical flows. Journal of Fluid Mechanics, 77: 531-569.

Jegede, O.O. and Foken, T., 1999. A study of the internal boundary layer due to a roughness change in neutral conditions observed during the LINEX field campaigns. Theoretical and Applied Climatology, 62: 31-41.

Jiménez, J. and Pinelli, A., 1999. The autonomous cycle of near-wall turbulence. Journal of Fluid Mechanics, 389: 335-359.

Johansson, A.V. and Alfredsson, P.H., 1982. On the structure of turbulent channel flow. Journal of Fluid Mechanics, 122: 295-314.

Kaimal, J.C. and Finnigan, J.J., 1994. Atmospheric Boundary Layer Flows: Their Structure and Measurement. Oxford University Press, New York, 289 pp.

Kawamura, R., 1951. Study on sand movement by wind. Reports of Physical Sciences Research Institute of Tokyo University, 5(3-4): 95-112 [Translated from Japanese by National Aeronautic and Space Administration (NASA), Washington DC, 1972].

Kim, H.T., Kline, S.J. and Reynolds, W.C., 1971. The production of turbulence near a smooth wall in a turbulent boundary layer. Journal of Fluid Mechanics, 50(1): 133-160.

Kline, S.J., Reynolds, W.C., Schraub, F.A. and Runstadler, P.W., 1967. The structure of turbulent boundary layer. Journal of Fluid Mechanics, 30(4): 741-773.

Kline, S.J. and Robinson, S.K., 1989. Quasi-coherent structures in the turbulent boundary layer: Part I. Status report on a community-wide summary of the data. In: S.J. Kline and N.H. Afgan (Editors), Near-wall Turbulence. Hemisphere, New York, pp. 200-217.

Kolmogorov, A.N., 1941. Dissipation of energy in a locally isotropic turbulence. Doklady Akad. Nauk SSSR, 32(1): 19-21 (English translation in: American Mathematical Society Translations, 1958, Series 2, Vol. 8, p. 57, Providence, R.I.).

Kostaschuk, R.A. and Church, M.A., 1993. Macroturbulence generated by dunes, Fraser River, Canada. Sedimentary Geology, 85: 25-37.

Kostaschuk, R., Church, M.A. and Luternauer, J.L., 1991. Acoustic images of turbulent flow structures in Fraser River estuary, British Columbia. Current Research, Part E: Geological Survey of Canada, Paper 91-1E: 83-90.

Krogstad, P-Å, and Skåre, P.E., 1995. Influence of a strong adverse pressure gradient on the turbulent structure in a boundary layer. Physics of Fluids, 7: 2014-2024.

Krumbein, W.C. and Pettijohn, F.J., 1938. Manual of Sedimentary Petrography: I. Sampling, preparation for analysis, mechanical analysis and statistical analysis. Appleton-Century, New York, 549 pp.

Küchermann, D., 1965. Report on the IUTAM symposium on concentrated vortex motion in fluids. Journal of Fluid Mechanics, 21: 1-20.

Kumar, P. and Fourfoula-Georgiou, E., 1997. Wavelet analysis for geophysical applications. Reviews of Geophysics, 35(4): 385–412.

Lancaster, N. and Nickling, W., 1994. Aeolian sediment transport. In: A.D. Abrahams and A.J. Parsons (Editors), Geomorphology of Desert Environments. Chapman & Hall, London, pp. 447-473.

Laufer, J., 1975. New trends in experimental turbulence research. Annual Reviews in Fluid Mechanics, 7: 307-326.

Lee, J.A., 1987. A field experiment on the role of small scale wind gustiness in aeolian sand transport. Earth Surface Processes and Landforms, 12: 331-335.

Leenders, J.K., Van Boxel, J.H. and Sterk, G., 2005. Wind forces and related saltation transport. Geomorphology, 71: 357-372.

Lettau, H.H. and Lettau, K., 1977. Experimental and micrometerological field studies of dune migration. In: K. Lettau and H.H. Lettau (Editors), Exploring the World's Driest Climate. University of Wisconsin-Madison, Madison, pp. 110-147.

Liandrat, J. and Moret-Bailly, F., 1990. The wavelet transform - Some applications to fluid dynamics and turbulence. European Journal of Fluid Mechanics B-Fluids, 9(1): 1-19.

Lim, Y.-H. and Lye, L.M., 2004. Wavelet analysis of tide-affected low streamflows series. Journal of Data Science, 2: 149-163.

Liu, P.C. and Babanin, A.V., 2004. Using wavelet spectrum analysis to resolve breaking events in the wind wave time series. Annales Geophyscicae, 22: 3335-3345.

Liu, H., Wang, L. and Jezak, K.C., 2005. Wavelet-transform based edge detection approach to derivation of snowmelt onset, end and duration from satellite passive microwave measurements. International Journal of Remote Sensing, 26(21): 4639-4660.

Mallat, S. and Zhong, S., 1992. Wavelet transform maxima and multiscale edges. In: M.B. Ruskai (Editor), Wavelets and their Applications. Jones and Bartlett, Boston, pp. 67-104.

McEwan, I.K., 1993. Bagnold's Kink; A physical feature of a wind velocity profile modified by blown sand? Earth Surface Processes and Landforms, 18: 145-156.

McEwan, I.K. and Willetts, B.B., 1991. Numerical model of the saltation cloud. In: O.E. Barndorff-Nielsen and B.B. Willets (Editors), Aeolian Grain Transport 1: Mechanics. Acta Mechanica Supplement 1. Springer-Verlag, Wien, pp. 53-66.

McEwan, I.K. and Willetts, B.B., 1993. Adaptation of the near-surface wind to the development of sand transport. Journal of Fluid Mechanics, 252: 99-113.

McKenna Neuman, C. and Nickling, W.G., 1994. Momentum extraction with saltation: Implications for experimental evaluation of wind profile parameters. Boundary-Layer Meteorology, 68: 35-50.

McLean, S.R., Nelson, J.M. and Shreve, R.L., 1996. Flow-sediment interactions in separating flows over bedforms. In: P.J. Ashworth, S.J. Bennett, J.L. Best and S.J. McLelland (Editors), Coherent Flow Structures in Open Channels. John Wiley and Sons, New York, pp. 203-226.

Meyers, S.D., Kelley, B.G. and O'Brien, J.J., 1993. An introduction to wavelet analysis in oceanography and meteorology: Application to the dispersion of Yanai waves. Monthly Weather Review, 121(10): 2858-2866.

Mi, X., Ren, H., Ouyang, Z., Wei, W. and Ma, K., 2005. The use of the Mexican hat and the Morlet wavelets for detection of ecological patterns. Plant Ecology, 179: 1-19.

Middleton, G.V. and Southard, J.B., 1984. Mechanics of Sediment Movement. Short Coarse No. 3, Society of Economic Paleontologists, Oklahoma.

Mori, N., Liu, P.C. and Yasuda, T., 2002. Analysis of freak wave measurements in the Sea of Japan. Ocean Engineering, 29(11): 1399-1414.

Namikas, S.L., 1999. Aeolian saltation: Field measurements and numerical simulations. Ph.D. Thesis, University of Southern California, Los Angeles, 475 pp.

Namikas, S.L., 2002. A floating-element drag plate for direct measurement of bed shear stress during eolian transport. Journal of Sedimentary Research, 72(2): 328-334.

Namikas, S.L., 2003. Field measurement and numerical modeling of aeolian mass flux distributions on a sandy beach. Sedimentology, 50(2): 303-326.

Narashimha, R. and Kailas, S.V., 1990. Turbulent bursts in the atmosphere. Atmospheric Environment, 24A(7): 1625-1645.

Pease, P., Lecce, S., Gares, P.A. and Lange, M., 2002. Suggestions for low-cost equipment for physical geography II: Field equipment. Journal of Geography, 101: 199-206.

Pendergrass, W. and Aria, S.P.S., 1984. Dispersion in neutral boundary layer over a step change in surface roughness - I. Mean flow and turbulence structure. Atmospheric Environment, 18: 1267-1279.

Perot, B. and Moin, P., 1995. Shear free turbulent boundary layers. Part 1. Physical insight into near wall turbulence. Journal of Fluid Mechanics, 295: 199-227.

Petenko, I.V., 2001. Advanced combination of spectral and wavelet analysis ("spavelet" analysis). Boundary-Layer Meteorology, 100: 287-299.

Pope, S.B., 2000. Turbulent Flows. Cambridge University Press, Cambridge, 771 pp.

Prandtl, L., 1938. On fully developed turbulence. Translated in Goldestein, S. (Ed.) 1938. Modern Developments in Fluid Dynamics, Vol 1. Oxford, Oxford University Press.

Quadrio, M. and Luchini, P., 2003. Integral space-time scales in turbulent wall flows. Physics of Fluids, 15(8): 2219-2227.

Rao, K.N., Narashimha, R. and Narayanan, M.A.B., 1971. The 'bursting' phenomenon in a turbulent boundary layer. Journal of Fluid Mechanics, 48(2): 339-352.

Reynolds, O., 1895. On the dynamical theory of incompressible viscous fluids and the determination of the criterion. Phil. Trans. Roy. Soc. A1, 186: 123.

Robinson, S.K., 1991a. Coherent motions in the turbulent boundary layer. Annual Review of Fluid Mechanics, 23: 601-639.

Robinson, S.K., 1991b. The kinematics of turbulent boundary layer structure. Ph.D. Thesis, Stanford University, Stanford, CA, 389 pp.

Runstadler, P.W., Kline, S.J. and Reynolds, W.C., 1963. An Experimental Investigation of the Flow Structure of the Turbulent Boundary Layer. Technical Report Number MD-8, Department of Mechanical Engineering, Stanford University, Palo Alto, CA, 308 pp.

Salmond, J., 2005. Wavelet analysis of intermittent turbulence in a very stable nocturnal boundary layer: Implications for the vertical mixing of ozone. Boundary-Layer Meteorology, 114: 463-488.

Schlichting, H. and Gersten, K., 2000. Boundary-Layer Theory. Springer, Berlin, 799 pp.

Schönfeldt, H.J. and von Löwis, S., 2003. Turbulence-driven saltation in the atmospheric surface layer. Meteorologische Zeitschrift, 12(5): 257-268.

Schoppa, W. and Hussain, F., 1997. Genesis and dynamics of coherent structures in near-wall turbulence: a new look. In: R.L. Panton (Editor), Self-Sustaining Mechanisms of Wall Turbulence. Computations Mechanics Publications, Southampton, UK and Boston, USA.

Sciremammano, F., 1979. A suggestion for the presentation of correlations and their significance levels. Journal of Physical Oceanography, 9: 1273-1276.

Sherman, D.J., 1992. An equilibrium relationship for shear velocity and apparent roughness length in aeolian saltation. In: J.D. Phillips and W.H. Renwick (Editors), Geomorphic Systems: Proceedings of the 23rd Binghamton Symposium in Geomorphology held 25-27 September 1992. Elsevier, Amsterdam, pp. 419-431.

Sherman, D.J., Jackson, D.W.T., Namikas, S.L. and Wang, J., 1998. Wind-blown sand on beaches: an evaluation of models. Geomorphology, 22: 113-133.

Short, A.D., 1983. Beaches of the New South Wales Coast. Australian Beach Safety and Management Program, Sydney.

Smith, C.R. and Walker, J.D.A., 1990. A conceptual model of wall turbulence. In: S. Robinson (Editor), Proceedings of the NASA Langley Boundary Layer Workshop, pp. 7.

Smith, C.R., Walker, J.D.A., Haidari, A.H. and Sobrun, U., 1991. On the dynamics of near-wall turbulence. Philosophical Transactions of the Royal Society of London, Series A, 336: 131-175.

Spaan, W.P. and van den Abeele, G.D., 1991. Wind borne particle measurements with acoustic sensors. Soil Technology, 4: 51.63.

Spies, P.-J. and McEwan, I.K., 2000. Equilibration of saltation. Earth Surface Processes and Landforms, 25(4): 437-453.

Spies, P.-J., McEwan, I.K. and Butterfield, G.R., 2000. One-dimensional transitional behaviour in saltation. Earth Surface Processes and Landforms, 25(5): 505-518.

Sterk, G., Jacobs, A.F.G. and Van Boxel, J.H., 1996. The effect of turbulent flow structures on sediment transport in the atmospheric boundary layer. In: G. Sterk (Editor), Wind Erosion in the Sahelian one of Niger: processes, models, and control techniques. Tropical Resource Management Papers 15. Wageningen Agricultural University, The Netherlands, pp. 13-31.

Sterk, G., Jacobs, A.F.G. and Van Boxel, J.H., 1998. The effect of turbulent flow structures on saltation sand transport in the atmospheric boundary layer. Earth Surface Processes and Landforms, 23: 877-887.

Sterk, G., Van Boxel, J.H. and Zuurbier, R., 2002. Interactions between turbulent wind flow and saltation sand transport. In: J.A. Lee and T.M. Zobeck (Editors), Proceedings of ICAR5/GCTE-SEN Joint Conference, International Center for Arid and Semiarid Lands Studies, Texas Tech University, Lubbock, TX, pp. 63-65.

Stout, J.E. and Zobeck, T.M., 1997. Intermittent saltation. Sedimentology, 44: 959-970.

Sullivan, P., Day, M. and Pollard, A., 1994. Enhanced VITA technique for turbulent structure identification. Experiments in Fluids, 19: 10-16.

Terradellas, E., Morales, G., Cuxart, J. and Yugue, C., 2001. Wavelet methods: Application to the study of the stable atmospheric boundary layer under non-stationary conditions. Dynamics of Atmospheres and Oceans, 34: 255-244.

Thomas, C. and Foken, T., 2005. Detection of long-term coherent exchange over spruce forest using wavelet analysis. Theoretical and Applied Climatology, 80: 91-104.

Torrence, C. and Compo, G.P., 1998. A practical guide to wavelet analysis. Bulletin of the American Meteorological Society, 79(1): 1-78.

Torrence, C. and Compo, G.P., accessed 2006. Wavelet software, available at http://paos.colorado.edu/research/wavelets/.

Vennard, J.K. and Street, R.L., 1982. Elementary Fluid Mechanics. John Wiley and Sons, New York.

Wallace, J.M., Eckelmann, H. and Brodkey, R.S., 1972. The wall region in turbulent shear flow. Journal of Fluid Mechanics, 54(1): 39-48.

Williams, G.P., 1986. Aeolian entrainment thresholds in a developing boundary layer. Ph.D. Thesis, Queen Mary and Westfield College, University of London, 524 pp.

Wiggs, G.F.S., Atherton, R.J. and Baird, A.J., 2004. Thresholds of aeolian sand transport: establishing suitable values. Sedimentology, 51(1): 95-108.

Wojtaszczyk, P., 1997. An Introduction to Wavelets. London Mathematical Society Student Texts, 37. Cambridge University Press, Cambridge, 272 pp.

Wright, L.D., 1970. The influence of sediment availability on patterns of beach ridge development in the vicinity of the Shoalhaven River Delta, N.S.W. The Australian Geographer, XI(3): 336-348.

Zhou, J., Adrian, R.J., Balachandar, S. and Kendall, T.M., 1999. Mechanisms for generating coherent packets of hairpin vortices in channel flow. Journal of Fluid Mechanics, 387: 353-396.

APPENDIX A

MEASURING THE TRANSPORT OF AEOLIAN SAND WITH A MICROPHONE SYSTEM

Abstract

This paper describes the “miniphone,” an instrument to measure aeolian saltation. This instrument is a modified electret microphone that detects the impacts of individual grains. The unidirectional miniphone is inexpensive (approximately US$10) and small, posing minimal disruption to the wind field. It can be sampled at rates up to 44,100 Hz using commonly available sound card technology or it can be interfaced with a data acquisition system. Data from deployments on beaches on Marco Island, FL, USA, and near Shoalhaven Heads, NSW, Australia, using sample rates of 44,100 Hz and 6000 Hz, are presented. An algorithm for identifying discrete impacts of grains is described. Saltation impacts were not reduced when sub-sampling a record from 44,100 Hz to 6000 Hz. Impacts detected by the miniphone were comparable to a scaled saltation flux measured by a co-located sand trap.

1. Introduction

Measuring the transport of aeolian sand has been a concern for almost three-quarters of a century (Bagnold, 1936). Numerous studies have focused on simultaneously measuring the rates of sediment transport (flux) and vertical profiles of wind velocity to compare the rates of field-based and model-estimated transport. Sherman et al. (1998), for example, found that the Lettau and Lettau (1977) model with the Belly (1964) moisture correction factor, best predicts sediment transport measured with traps. Sherman et al. (1998, 131) concluded that the results were “constrained by uncertainties regarding the efficiency of traps.” Nevertheless, traps continue to be the most commonly used method for measuring sediment flux in the field (Bauer and Namikas, 1998; Wang and Kraus, 1999; Namikas, 2002; Dong et al., 2004).

This paper has been submitted to Geomorphology.

Traps are limited because of poor temporal and spatial resolution, scouring around the base, and large, un-segregated openings (e.g., Jackson and Nordstrom’s (1999) traps were 0.05 m wide and 0.4 m high). Many attempts have been made to overcome these limitations, some are described in Table 1. Wang and Kraus (1999) installed a horizontal water trap level with the sand surface to cause minimal disturbance to the wind field. Jackson (1996), Bauer and Namikas (1998), and Namikas (2002) introduced traps that increased the temporal resolution of ‘traditional traps.’ Jackson (1996) and Bauer and Namikas (1998) built automated sediment weighing and recording systems that sampled at 1 Hz and 5 Hz, respectively. Jackson’s (1996) trap is a 0.24 m diameter circle, installed flush with the sand surface, that registers changes in weight at one gram intervals. Bauer and Namikas (1998) used the Nickling and McKenna-Neuman (1997) trap and designed a tipping bucket (T-BASS) mechanism below the bed to mechanically weigh and measure the captured sand. Namikas (2002) used sets of vertical and horizontal load-cell traps to improve the spatial and temporal resolution of measurements of flux.

Several alternatives to traps have been implemented in laboratory and field environments (e.g., Willetts and Rice, 1985; Sherman, 1990; Butterfield, 1998). Butterfield (1998) used laser/CCD optical sand transport sensors, or periscopes, sampling at 25 Hz with adjustable distances between 10 mm and 100 mm in the laboratory. In the field, adhesive surfaces (Matthews et al., 1998), tracers (Willetts and Rice, 1985), and injections of colored sand (Sherman, 1990), have been implemented with various degrees of success.

Most measurements at point sources obtained from sensors use piezo-electric technology (e.g., Gillette and Stockton, 1986; Baas, 2004) or microphones (e.g., Spaan and Van den Abeele, 1991) to detect the impacts of sand grains. The SENSIT™ is a commercially produced omni-directional sensor, costing approximately US$1900 with a piezo-electric crystal and has been deployed in the field by Gillette and Stockton (1986), Stout and Zobeck (1997), Atherton (2002),

Table A-1: A review of several measuring devises for aeolian transport used in laboratory- and field-based studies.

Sand Measuring Device	**Approximate Dimensions Downstream * Cross-stream * Height**	**Advantages**	**Disadvantages**
Traps	Varies	Measures mass flux; inexpensive; low-technology	Scouring; poor temporal and spatial resolution; edge effects
Solenoid trap (Jackson, 1996)	Trap opening is a 0.24m diameter circle flush with bed	Minimal interference with wind field; moderately inexpensive (£200); measures saltation, reptation, and short-term suspension	Measures at 1 Hz; registers readings when 1g interval change is exceeded
Tipping bucket (Bauer and Namikas, 1998)	Above ground dimensions vary; this paper - 0.20m*0.12m*0.75m using Nickling and McKenna-Neuman (1997) design	Measures mass flux; rotates 60º to adjust to mean wind direction; higher temporal resolution than "traditional" traps; 5 Hz sample rate	Low capacity (10-20g) tipping bucket (noted by authors) limits temporal duration of deployment; no vertical resolution
Water trap (Wang and Kraus, 1999)	Varies; this paper - opening was 1.5 m*2.0 m (flush with bed)	No interference with wind field; measures saltation, reptation, and short-term suspension; low-technology; trapping efficiency close to unity	Poor temporal (30 min runs in this paper) and spatial resolution
Load cell traps (Namikas, 1999)	HTRAP: 2.11m*0.15m*undef. (35 openings, 0.02m – 0.016m downwind length); VTRAP: undef.*2.5m*0.35m (15 openings: 0.01m, 0.20m, or 0.04m high, all 0.06m cross-stream)	Measures mass flux; high sample rate compared to other traps (burst sampled at 100 Hz for 0.1s at 1s intervals to resolve to 1 Hz)	Low spatial resolution relative to sensors
Adhesive surface (Matthews et al., 1998)	undef.*0.05m*0.043m	Measures vertical flux distribution and impact counts	Poor temporal resolution relative to sensors (deployed at 120s intervals)
Tracers	Not applicable	No wind field interference; low technology	Low recovery of traced sand
Optical sensors (Butterfield, 1998)	Periscopes (2): 0.068m*0.005m adjustable to 0.8m; sample area: 0.068m*0.01m to 0.1m*up to 0.8m	Up to 40 Hz sample rate; measures mass flux; relatively non-intrusive to wind field	Laboratory only (has not been deployed in field)
SENSIT^{TM} - piezo-electric crystal (Model H21)	Cylinder-shaped: 0.37m high* 25.4mm diameter; frontal sensing area: 325mm^2	Obtains impact counts	Relatively expensive (US$1900)
Safire - piezo-electric crystal	0.02m diameter*0.3m height (sensor frontal area is 400mm^2)	Measures impact counts and voltage; 20 Hz sample rate; minimal flow obstruction	Omnidirectional; calibration complications; 200 hits per second maximum
Saltiphone (Spaan and Van den Abeele, 1991)	0.30m*0.19m*0.20m (microphone membrane is 201mm^2)	Self-orients to wind; tube protects microphone from adverse environmental conditions; records individual grain impacts; continuous sample rate	Relatively large; poor spatial resolution; sensor 0.1m above bed; does not measure mass flux
Miniphone (this study)	Cylinder-shaped: 0.3m high* 9.4mm diameter; frontal sensing area 28.27mm^2 (varies depending on microphone model)	Obtains impact counts; sample rate limited by data acquisition system; minimal flow obstruction; inexpensive (~US$10)	Does not self-orient to wind direction, nor measure mass flux

and Wiggs et al. (2004), for example. The SENSIT^{TM} is a cylinder measuring 0.37 m long and 25.4 mm in diameter (personal communication, Paul Stockton, model H12) with a 325 mm^2 piezo-electric crystal (frontal area) that registers the impacts of sand grains. A disadvantage to the SENSIT^{TM} is that when using the kinetic energy channel the output of the sensor has a positive linear dependency on temperature (Heidenreich et al., 2002). Therefore, as the ambient temperature increases, the level of the background noise increases. Davidson-Arnott et al. (2003) and Baas (2004) used the *Safire* (manufactured by Sabatech, approximately US$300), an omni-directional, peizo-electric probe, with a height of 0.3 m and diameter of 0.02 m. Located 0.12 m from the instrument base is a sensing ring connected to a peizo-electric crystal. The crystal has a frontal surface area of 400 mm^2 that can detect a maximum of 200 sand impacts per second (Davidson-Arnott et al., 2003). Baas (2004) described several deficiencies associated with the *Safire*. First, the response is not constant around the azimuth of the sensitive ring; two “sweet spots” occur with relatively high sensitivity. Also, when comparing multiple sensors, each has a different momentum threshold. Thus, extensive and careful calibration is required for each sensor.

Microphones represent an alternative to piezo-electric crystal technology for sensing the impacts of grains. Spaan and Van den Abeele (1991) introduced the “saltiphone” to measure saltation in field-based aeolian experiments and it has been used by Arens (1996), Van Dijk et al. (1996), and Sterk et al. (1998). The saltiphone is a microphone mounted in a stainless-steel tube at 0.1 m above the bed. The tube protects the microphone against adverse environmental conditions. No calibration problems have been cited, but Spaan and Van den Abeele (1991) and Arens (1996) did recognize that 90% of all saltation occurs below the sensor height (0.1 m above the bed). Saltiphones are inexpensive; but are relatively large (0.91 m wide, 0.3 m long, and 0.20 m high). Arrays of vertical or dense horizontal instrument sets are not possible because of modifications to the wind field (wake effects).

The sensor described here is a high-resolution instrument that is microphone-based, unidirectional, relatively inexpensive, and small (Fig. A-1). The sensor uses technology similar to the saltiphone (microphone). The “miniphone” has a cross-section area of less than 0.0001 m^2 and is not self-orienting. The small size permits relatively dense vertical and horizontal arrays with minimal disruption of the wind field. The miniphone can be deployed at elevations less than 0.01 m above the bed, compared to the 0.04 m deployment elevation employed by Baas (2004), for example. The unidirectional design avoids the “sweet spot” issues such as those described by Baas (2004). This sensor produces an electronic signal with spikes in the signal indicating the impacts by sand grains.

2. Instrument Details

The primary component of the miniphone instrument is an electret microphone, a modified version of the classic capacitor, or condenser, microphone. Electret microphones produce changes in capacitance because of mechanical vibrations that produce voltage variations proportional to sound waves. A JLI Electronics microphone was used in this example. This company (and several others) produces a range of microphone sizes and specifications (e.g., sensitivity and frequency response). The microphone used in this study was model F9445AL that is 9.4 mm in diameter (69.36 mm^2 frontal area) and has a sensor diameter of 6.0 mm (28.27 mm^2 frontal area). Fig. A-2 shows an “off-the-shelf” microphone.

The electret microphones were modified before use in the field. The miniphone functions similar to a drum; when a sand grain strikes, the diaphragm vibrates and generates an electronic signal. Because of minimal momentum, small or slow-moving sand grains do not register an audible impact through the protective black (felt) surface (Fig. A-2a). Therefore, the felt and an underlying metal casing were removed. Care was taken to remove only the metal casing and not the outer ring that secures the microphone diaphragm, i.e., the sensor (arrow on Fig. A-1). Signal and common ground wires (22 AWG) were soldered to the pins on the back of the miniphone (Fig. A-2b), for connection to the computer. Wired microphones were glued inside brass tubes that were wrapped in tape to ensure that grain impacts on the outside of the tube would not be detected.

Miniphones can be interfaced with a computer through a high-end analog-to-digital data acquisition system that is capable of recording signals in the millivolt range on a sound card. Between one and nine volts of additional (battery) power is required between the miniphone and the data acquisition system to power the internal Field Effect Transistors (FET) in the microphone. When the miniphone is excited, during grain impacts, for example, FETs amplify the small distance changes between the charged diaphragm and the capacity plate behind it. Most conventional data acquisition systems, operating with multiple instruments (i.e., channels), sample at rates less than 10,000 Hz when all channels are programmed to record simultaneously. Alternatively, when connecting the miniphones to the sound card in the computer, power is drawn exclusively from the computer, the sample rate is 44,100 Hz, and one sound card is required for each miniphone.

A sensitivity analysis was performed to estimate potential maximum counts of sand impact. Previous studies using microphone-based sensors indicate signal saturation with rates of grain impacts between 500 and 1000 per second (Spaan and Van den Abeele, 1991; Schönfeldt and von Löwis, 2003, respectively). The saturation risk for the miniphone was estimated using the exponential vertical distribution for field-based studies presented by Farrell and Sherman (2003; their Figure 4), the Lettau and Lettau (1977) transport model, shear stresses equal to 0.5 m/s and 0.35 m/s, and grain sizes of 0.25 and 0.20 mm. At shear stresses equal to 0.5 m/s and 0.35 m/s and at 0.02 m above the bed, 460 and 100 impacts/s were estimated for grain sizes of 0.25 mm. When the grain size is reduced to 0.20 mm, the estimated counts of impacts increases to 875 and 210 impacts/s at an elevation of 0.02 m above the bed for shear stresses equal

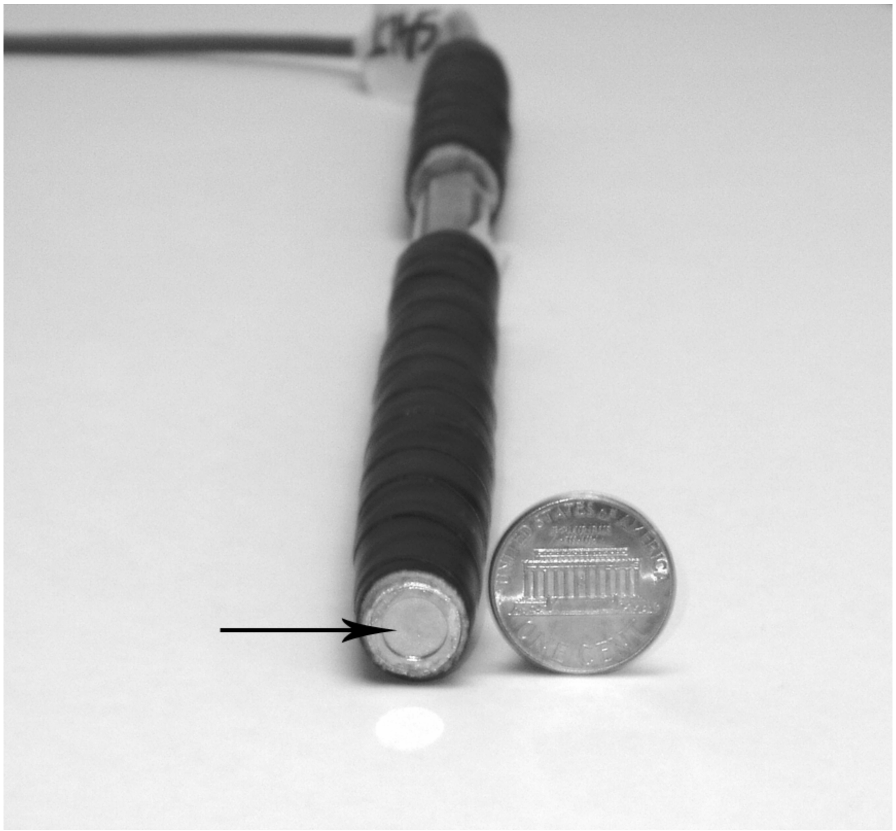

Fig. A-1: Field-ready miniphone encased in a tape-wrapped brass tube. The microphone diaphragm, indicated by the arrow, is the sensor portion of the instrument. A United States one cent coin is shown for scale.

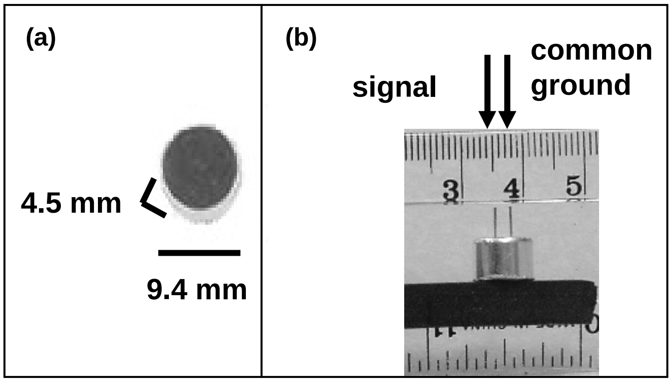

Fig. A-2: The microphone as produced by the manufacturer. Unit diameter is 9.4 mm and depth is 4.5 mm (a). Backside of instrument has pins to connect leads (wires) for the miniphone output signal and common ground (b).

to 0.5 m/s and 0.35 m/s, respectively. Adjusting height of the sensor above the bed has a considerable effect on the number of expected impacts. The predicted grain per second count decreases 50% if the elevation of the miniphone is increased from 0.02 to 0.05 m above the bed.

3. Miniphone Field Evaluation

3.1 Field Deployment and Conditions

A miniphone connected to a sound card sampling at 44,100 Hz was deployed on Residents Beach in Marco Island, FL, USA on 29 December 2003 for 155 seconds (s). The average grain size was approximately 0.2 mm. A second miniphone was deployed between Seven Mile and Comerong beaches near Shoalhaven Heads, NSW, Australia on 3 August 2004. A miniphone was monitored using a 6000 Hz sample rate and mounted 0.02 m above the bed for 354 s. A hose-type sand trap (Pease et al., 2002), with an orifice measuring 0.1 m by 0.1 m, was deployed 0.20 m from the miniphone. Fig. A-3 shows images of the beaches of Marco Island and Shoalhaven Heads.

Fig. A-3: Marco Island, FL, USA (a) and Shoalhaven Heads, NSW, Australia (b).

3.2 Analysis and Results of Sampling on Marco Island

Fig. A-4a is a five second sample of the raw 44,100 Hz signal from Marco Island. Periods where the signal is higher (around 4.5 s, for example) indicate increased sediment transport. A one second excerpt of the five second record (Fig. A-4a) is shown in Fig. A-4b and Fig. A-4c shows a 0.1 second portion of the one second record. Spikes in the time series, most visible in Fig. A-4c, indicate impacts of individual grains. Twenty-six impacts occurred between 2.4-2.5 s (Fig. A-4c) and 697 impacts occurred between 2.0-3.0 s (Fig. A-4b).

The 44,100 Hz record (Fig. A-4a) can be sub-sampled to 6000 Hz to correspond to the sample rate used in the field deployment at Shoalhaven Heads. This exercise also is a method to calibrate the efficiency of miniphone sampling at 6000 Hz. Fig. A-5 compares the 44,100 Hz time series depicted in Fig. A-4c with the 6000 Hz sub-sampled time series. Decreasing the sample rate to 6000 Hz decreases the magnitude of the signal, yet the individual grain impacts remain distinguishable.

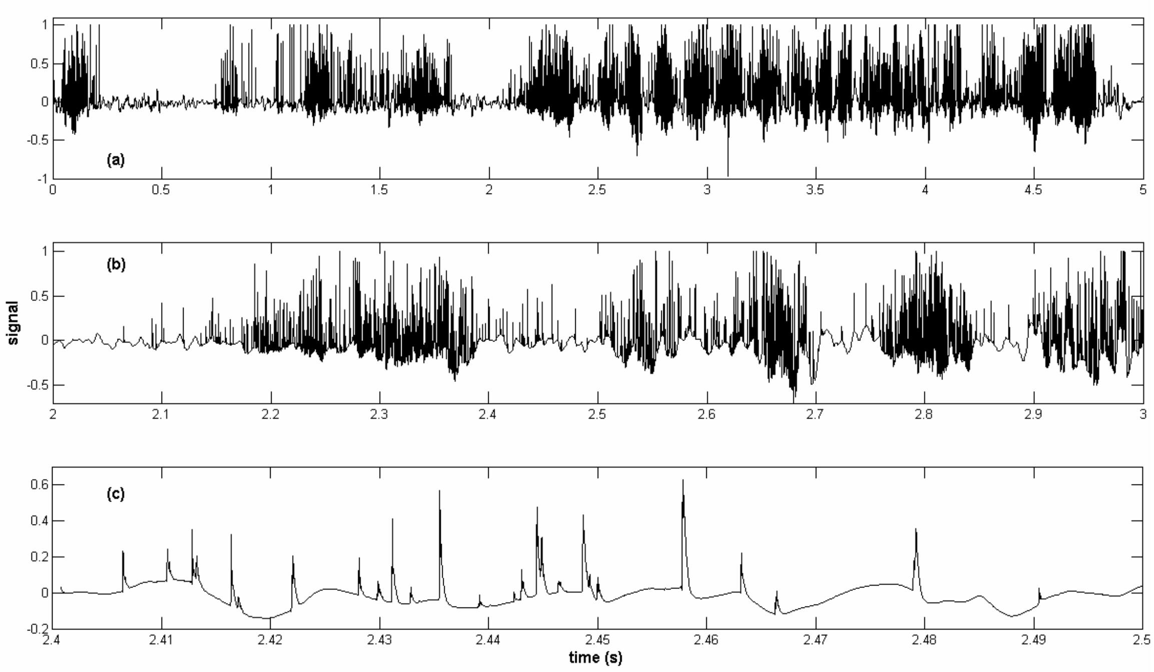

Fig. A-4: A five second time series of grain impacts sampled with a sound card at 44,100 Hz (a). A one second portion of the five second record (a) is shown in (b); (c) is a 0.1 second portion of the time series shown in (a) and (b).

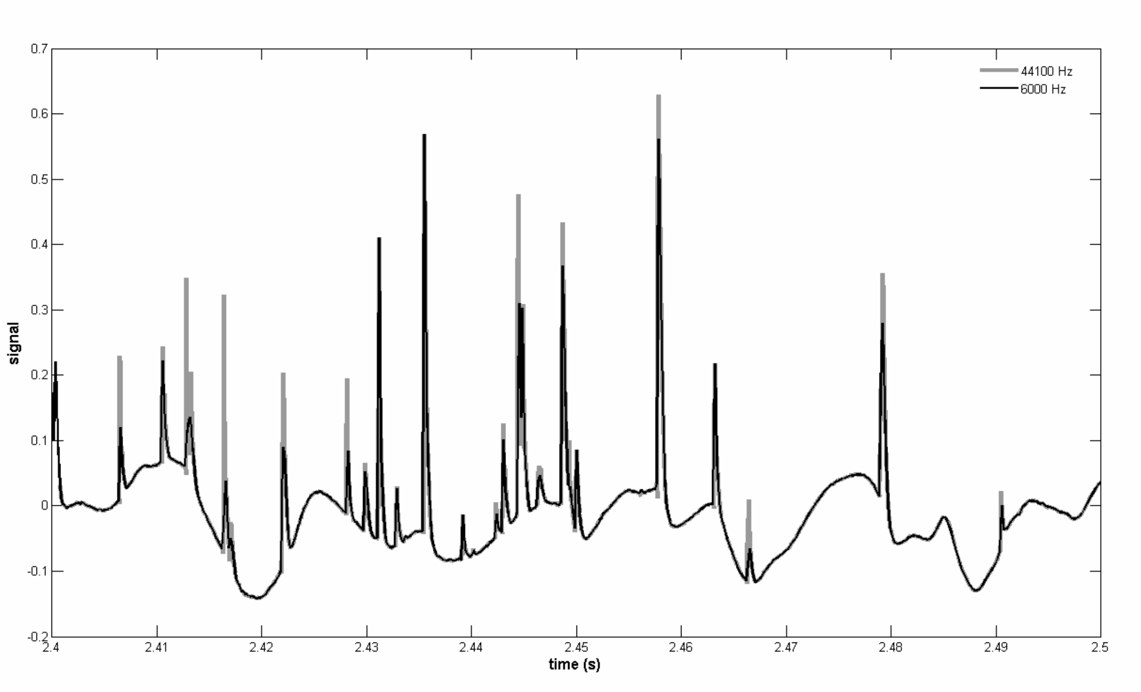

Fig. A-5: Time series from the miniphone sampled at 44,100 Hz (grey trace) and sub-sampled to 6000 Hz (black trace).

3.3 Analysis and Results for Sampling at Shoalhaven Heads

Fig. A-6 shows a five (a), one (b), and 0.1 (c) second sample from an unprocessed time series from the instrument on Shoalhaven Heads. An algorithm, developed to isolate the inputs of the grains from the background noise in the time series, is outlined in the following seven steps, given a "raw" microphone time series u:

1) The three-point running mean is subtracted from each raw data value.

$$v_i = u_i - \left(\overline{u_{i-1} + u_i + u_{i+1}}\right)$$

2) All negative values in the time series are set to zero.

3) The absolute value of the moving range of two values is calculated.

$$w_i = \left|v_i - v_{i-1}\right|$$

4) The mean from the time series (w) is removed.

$$x_i = w_i - \overline{w}$$

5) Values less than four standard deviations of the x time series (step 4) are set to zero.

6) Maxima are identified and remaining points set to zero. Maxima are defined as data points (x_i) greater than the previous point (x_{i-1}) and greater than or equal to the latter point (x_{i+1}). If using MATLAB, the following code may be employed, where y is the new time series:

```
for i=2:length(x)-1
if x(i-1)<x(i) & x(i)>=x(i+1)
y(i)=x(i);
else
y(i)=0;
end
end
```

7) The identification of signal maxima and setting non-maxima to zero (step 6) is repeated to remove double counting of a single grain impact. If using the MATLAB code from step 6, one should replace the x with the y time series and identify a new variable in place of y. Double counting was not frequent in the signal examined here.

Figs. A-7a and A-7b show the same 1.0 and 0.1 second portions of the time series shown in Figs. A-6b and A-7c, respectively. Fig. A-7 shows, however, the time series after application of the aforementioned algorithm. Data points designated by circles in Fig. A-7 represent the impacts of grains.

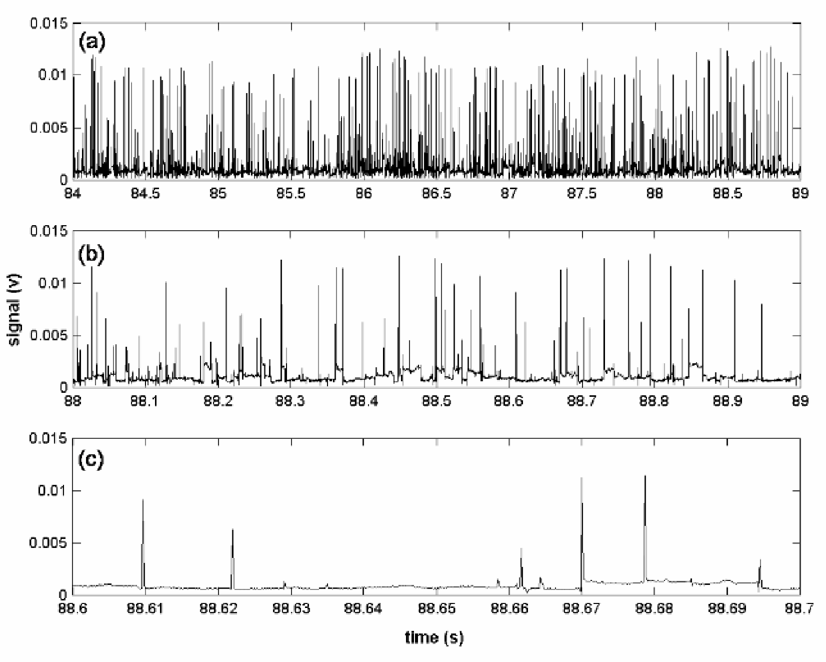

Fig. A-6: Five (a), one (b), and 0.1 (c) second time series of an unprocessed miniphone sampled 6000 Hz.

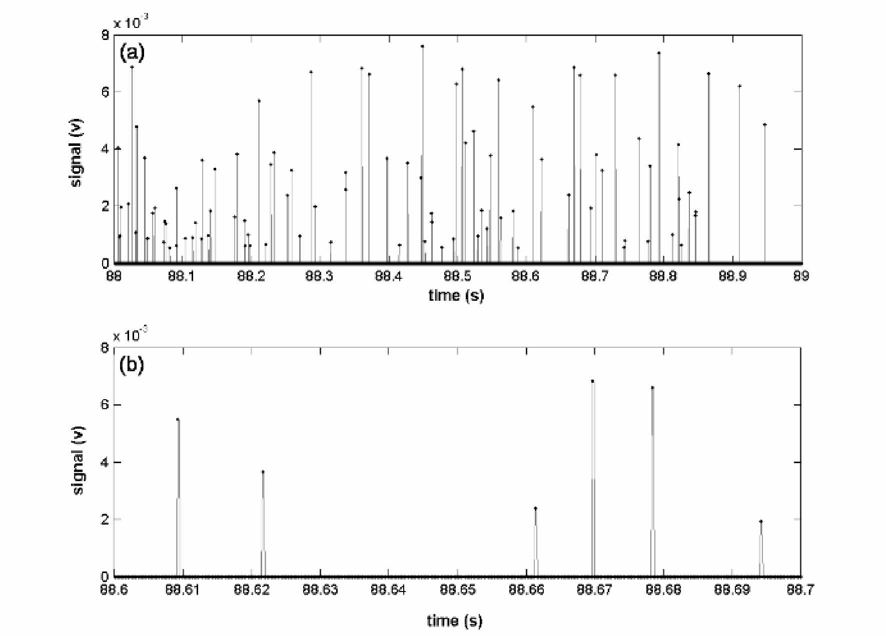

Fig. A-7: One (a) and 0.1 (b) second time series of a processed miniphone sampled 6000 Hz. These examples correspond to those shown in Figs. 6b and 6c. Circles greater than zero indicate the inputs of grains.

3.4 Comparing Transport as Detected by a Sand Trap and Miniphone

The quantity of sediment captured by the hose-style trap can be compared to the number of impacts measured by the miniphone as a means to assess the performance of the latter. To make this comparison, the 0.01 m^2 trap was mathematically reduced in size to equal the miniphone surface area, 0.00002829 m^2, to calculate an equivalent saltation flux. It was assumed that the mini-trap was centered at 0.01 m above the bed, the same elevation as the miniphone, and experienced no additional boundary effects compared to the 0.01 m^2 trap. The exponential-based vertical profile relationship of Kawamura (1951):

$$q(z) = 0.11((1/z) - (1/14))^{1.08} \tag{1}$$

where z is elevation above the bed (in cm), was used to integrate the amount of sediment captured in the mini-trap. During the 354 s data run, 1018.25 g of 0.25 mm sand were captured. The distribution of grain sizes is shown in Fig. A-8. Using Eq. 1, the mini-trap captured 90.62 g during the sample period, or 0.25 g/s.

The miniphone detected a total of 40,540 impacts from sand grains, equivalent to 115 impacts/s, during the 354 second time series. The percentage mass flux for each grain size classification (shown in Fig. A-8) was calculated to compare the rate of impacts detected by the miniphone with the value for mini-trap mass flux (90.26 g). This calculation reveals that an estimated mass of 167.39 g impacted the miniphone during the sample period, or 0.47 g/s.

Using the value of the mass flux value from a hose-style trap deployed 0.20 m from the miniphone, an equivalent rate of transport for a miniphone-sized trap revealed that the mini-trap captured 54% of the transport estimated by the miniphone. Possible reasons for differences in the estimations include, horizontal variability in the saltation field (c.f., Gares et al., 1996; Jackson and Nordstrom, 1999) and errors associated with the calculations, for example the difference between the actual and predicted vertical profile mass flux (Kawamura, 1951). However, given the multiple potential sources for error, the extrapolated mass flux values for the miniphone and sand trap are quite similar.

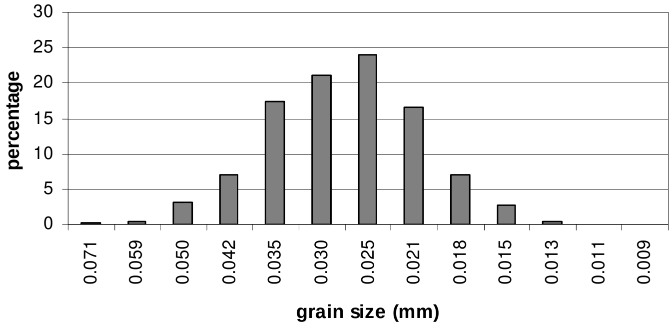

Fig. A-8: Distribution of grain sizes for the sand trap deployed near Shoalhaven Heads, NSW, Australia.

4. Summary

A modified electret microphone system was used to detect and record individual impacts of grains in the saltation layer at high frequencies. The miniphone improves upon previous microphone-based systems (e.g., Spaan and Van den Abeele, 1991) because it is smaller (exposed area to wind is 69 mm^2 and 28 mm^2 for the entire instrument and the sensor, respectively) and, therefore, can measure saltation inside the most active region of saltation, and is much less expensive. Miniphones, wired to a sound card, samples at 44,100 Hz, vastly exceeding the rates of sampling for previously described sensors and traps (e.g., Spaan and Van den Abeele, 1991; Namikas, 2002; Baas, 2004). If the miniphones are connected to a data acquisition system and are set sample at 6000 Hz, the miniphone does not miss any impacts compared to the faster sample rate of 44,100 Hz. An algorithm is presented that selects the individual grain impacts from background (“raw”) miniphone time series.

The miniphone is an ideal instrument to detect saltation intermittency (e.g., Stout and Zobeck, 1997). Also, many studies have attempted to establish a correspondence between the turbulent wind field and the fluctuations in the saltation field (e.g., Bauer et al., 1998; Davdison-Arnott et al., 2003). The results of these studies have been mixed to inconclusive. Wiggs et al., (2004) acknowledge that their large instrument distance, about one meter, between their wind and sand measuring devises may have contributed to some of their discrepancies in their data. The advent of the miniphone allows for closely located anemometer and miniphone deployments, and therefore, may help to contribute to a more clear understanding of the linkages between fluctuating wind and saltation.

5. Acknowledgements

Financial support was provided in part from a NSF Doctoral Dissertation Research Improvement Grant (Award #0425770, JTE and Douglas Sherman) and a National Science Foundation East Asia Summer Institute for US Graduate Students Grant (Award #0413541, JTE), that is supported by the Australian Academy of Sciences. Marco Island field assistance was provided by Joanna Todisco. The Shoalhaven Heads data was collected as a part of a larger project in which the following assisted or provided logistical support: Rob Brander, Eugene Farrell, Wansang Ryu, Douglas Sherman, Andy Short, and Julia Short.

6. References

Arens, S.M., 1996. Rates of aeolian transport on a beach in a temperature humid climate. Geomorphology, 17: 3-18.

Atherton, R.J., 2002. Moisture dynamics and aeolian activity on a temperate meso-tidal beach. Ph.D., University of Sheffield, Sheffield.

Baas, A.C.W., 2004. Evaluation of saltation flux impact responders (Safires) for measuring instantaneous aeolian sand transport intensity. Geomorphology, 59: 99-118.

Bagnold, R.A., 1936. The movement of desert sand. Proceedings of the Royal Society of London. Series A, Mathematical and Physical Sciences, 157: 594-620.

Bauer, B.O. and Namikas, S.L., 1998. Design and field test of a continuously weighing, tipping-bucket assembly for aeolian sand traps. Earth Surface Processes and Landforms, Technical and Software Bulletin, 23: 1171-1183.

Bauer, B.O., Yi, J., Namikas, S.L. and Sherman, D.J., 1998. Event detection and conditional averaging in aeolian systems. Journal of Arid Environments, 39(3): 345-375.

Belly, P.Y., 1964. Sand Movement by Wind, U.S. Army Corps of Engineers, CERC, Washington D.C.

Butterfield, G.R., 1998. Transitional behaviour of saltation: wind tunnel observations of unsteady winds. Journal of Arid Environments, 39: 377-394.

Davidson-Arnott, R.G.D., Ollerhead, J., Hesp, P.A. and Walker, I.J., 2003. Spatial and temporal variability in intensity of aeolian transport on a beach and foredune. In: Coastal Sediments '03 (Eds R.A. Davis and P.A. Howd), pp. CDROM, ISBN# 981.238.422.7. WorldScientific Publishing Corporation and East Meets West Productions, Clearwater, FL.

Dong, Z., Sun, H. and Zhao, A., 2004. WITSEG sampler: a segmented sand sampler for wind tunnel test. Geomorphology, 59: 119-129.

Farrell, E.J. and Sherman, D.J., 2003. Re-assessment of surface-wind systems for aeolian saltation. In: Proceedings of the Sixth International Conference on the Mediterranean Coastal Environment, MEDCOAST 03 (Ed E. Özhan), 3, pp. 1457-1468.

Gares, P.A., Davidson-Arnott, R.G.D., Bauer, B.O., Sherman, D.J., Carter, R.W.G., Jackson, D.W.T. and Nordstrom, K.F., 1996. Alongshore variations in aeolian sediment transport: Carrick Finn Strand, Ireland. Journal of Coastal Research, 12: 673-682.

Gillette, D.A. and Stockton, P.H., 1986. Mass, momentum and kinetic energy fluxes of saltating particles. In: Aeolian Geomorphology. Proceedings of the 17th Binghampton Symposium on Geomorphology (Ed W. Nickling), pp. 35-56. Allen & Unwin, Boston.

Heindenreich, S.K., Leys, J.F., McTainsh, G.H. and Larney, F.J., 2002. Temperature sensititvity of a peizo-electric sensor used for wind erosion measurements. In: J.A. Lee and T.M. Zobeck (Editors), Proceedings of ICAR5/GCTE-SEN Joint Conference, International Center for Arid and Semiarid Lands Studies, Texas Tech University, Lubbock, Texas, USA, pp. 108-110.

Jackson, D.W.T., 1996. A new, instantaneous aeolian sand trap design for field use. Sedimentology, 43: 791-796.

Jackson, N.L. and Nordstrom, K.F., 1999. Spatial variation in source characteristics and aeolian trapping rates on a beach. In: Coastal Sediments '99 (Eds N.C. Kraus and W.G. McDougal), pp. 1198-1206. American Society of Civil Engineers, Long Island, New York.

Kawamura, R., 1951. Study on sand movement by wind. Reports of Physical Sciences Research Institute of Tokyo University, 5: 95-112 [Translated from Japanese by National Aeronautic and Space Administration (NASA), Washington DC, 1972].

Lettau, H.H. and Lettau, K., 1977. Experimental and Micrometerological Field Studies of Dune Migration. In: Exploring the World's Driest Climate (Eds K. Lettau and H.H. Lettau), IES Report 101, pp. 110-147. University of Wisconsin-Madison, Madison.

Matthews, R.J., Stutz, M.L. and Sam Smith, A.W., 1998. A field investigation study to determine the properties of windblown beach sand. Journal of Coastal Research, 14: 444-450.

Namikas, S.L., 1999. Aeolian saltation: Field measurements and numerical simulations. Ph.D., University of Southern California, Los Angeles, CA, 475 pp.

Namikas, S.L., 2002. Field evaluation of two traps for high-resolution aeolian transport measurements. Journal of Coastal Research, 18: 136-148.

Nickling, W.G. and McKenna-Neuman, C., 1997. Wind tunnel evaluation of a wedge-shaped aeolian sediment trap. Geomorphology, 18: 333-345.

Pease, P., Lecce, S., Gares, P.A. and Lange, M., 2002. Suggestions for low-cost equipment for physical geography II: Field equipment. Journal of Geography, 101: 199-206.

Schönfeldt, H.J. and von Löwis, S., 2003. Turbulence-driven saltation in the atmospheric surface layer. Meteorologische Zeitschrift, 12: 257-268.

Sherman, D.J., 1990. Evaluation of aeolian sand transport equations using intertidal-zone measurements, Saunton Sands, England. Sedimentology, 37: 385-392.

Sherman, D.J., Jackson, D.W.T., Namikas, S.L. and Wang, J., 1998. Wind-blown sand on beaches: an evaluation of models. Geomorphology, 22: 113-133.

Spaan, W.P. and Van den Abeele, G.D., 1991. Wind borne particle measurements with acoustic sensors. Soil Technology, 4: 51.63.

Sterk, G., Jacobs, A.F.G. and Van Boxel, J.H., 1998. The effect of turbulent flow structures on saltation sand transport in the atmospheric boundary layer. Earth Surface Processes and Landforms, 23: 877-887.

Stout, J.E. and Zobeck, T.M., 1997. Intermittent saltation. Sedimentology, 44: 959-970.

Van Dijk, P.M., Stroosnijder, L. and De Lima, J.L.M.P., 1996. The influence of rainfall on transport of beach sand by wind. Earth Surface Processes and Landforms, 21: 341-352.

Wang, P. and Kraus, N.C., 1999. Horizontal water trap for measurement of aeolian sand transport. Earth Surface Processes and Landforms, 24: 65-70.

Wiggs, G.F.S., Atherton, R.J. and Baird, A.J. 2004. Thresholds of aeolian sand transport: establishing suitable values. Sedimentology, 51: 95-108.

Willetts, B.B. and Rice, M.A. 1985. Wind tunnel tracer experiments using dyed sand. In: Proceedings of the International Workshop on the Physics of Blown Sand, Department of Theoretical Statistics, Aarhus University, Memoirs no. 8, pp. 225-242.

APPENDIX B

This appendix shows the calibration information for the Dantec Dynamics thermal anemometers. Fig. A-9 shows a screen-grab from the MS Excel spreadsheet provided by Dantec Dynamics. The digital version of the spreadsheet (available from the author or from Dantec Dynamics) is only able to calibrate one data point (voltage to wind speed) at a time (by entering a value in cell E11), therefore a MATLAB algorithm was used to process the entire time series (Fig. A-10). The values in cells A19:A26 and B19:B26 (for velocity, “U” and voltage, “V”) in Fig. A-1 are the unique calibration values for thermal anemometer #SN006 (cell E9) which was the instrument that was used for Runs 1-5.

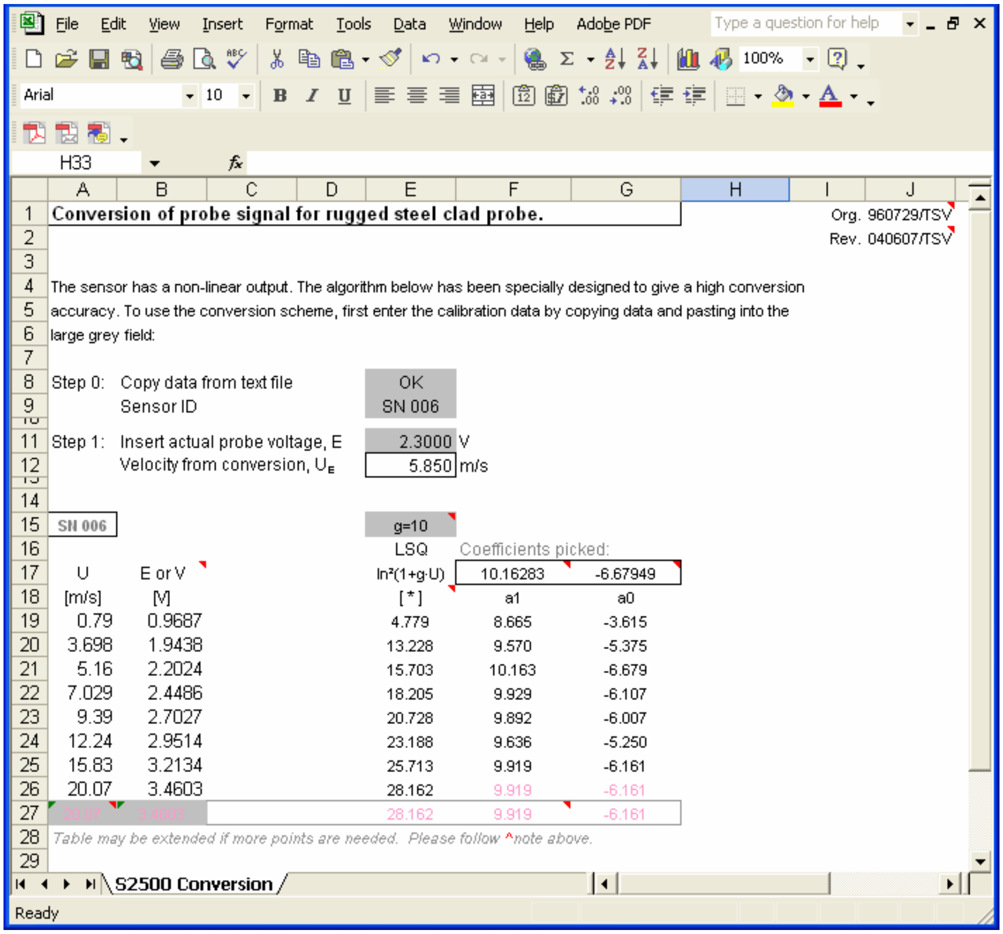

Conversion of probe signal for rugged steel clad probe.

Org. 960729/TSV
Rev. 040607/TSV

The sensor has a non-linear output. The algorithm below has been specially designed to give a high conversion accuracy. To use the conversion scheme, first enter the calibration data by copying data and pasting into the large grey field:

Step 0: Copy data from text file — OK
Sensor ID — SN 006

Step 1: Insert actual probe voltage, E — 2.3000 V
Velocity from conversion, U_E — 5.850 m/s

A	B	E	F	G
SN 006		g=10		
		LSQ	Coefficients picked:	
U	E or V	ln²(1+g·U)	10.16283	-6.67949
[m/s]	[V]	[*]	a1	a0
0.79	0.9687	4.779	8.665	-3.615
3.698	1.9438	13.228	9.570	-5.375
5.16	2.2024	15.703	10.163	-6.679
7.029	2.4486	18.205	9.929	-6.107
9.39	2.7027	20.728	9.892	-6.007
12.24	2.9514	23.188	9.636	-5.250
15.83	3.2134	25.713	9.919	-6.161
20.07	3.4603	28.162	9.919	-6.161
20.07	3.4603	28.162	9.919	-6.161

Table may be extended if more points are needed. Please follow ^note above.

Fig. A-9. Screen-grab from Microsoft Excel program provided by Dantec Dynamics to calibrate the thermal anemometers used in this study.

```
function [yyc] = calTA(yy,sn);

% calTA.m
%   Purpose:  Calibrates thermal anemometer
%   Input:
%      yy = signal record (v)
%      sn = calibration 'SN006caldata.txt' file from Dantec
%   Export:
%       yyc = calibrated (m/s) record
%   History:
%      Jean Ellis, TAMU Geography, February 2005
%      Created for MATLAB v. 6.0
%   Comment:
%      Column letters correspond with file provided by Dantec
%             (shown in screen grab, Appendix A-2A)

% Least squares (LSQ) (column E)
for kk=1:length(sn);
    lsq(kk,1) = (log(1+10*sn(kk,1)))^2;
end

% First coefficient column (column F)
for kk=1:length(sn)-1
    coa(kk,1)=(lsq(kk+1,1)-lsq(kk,1))/(sn(kk+1,2)-sn(kk,2));
end
kk = length(coa);
coa(kk+1,1)=coa(kk,1);

% Second coefficient column (column G)
for kk=1:length(coa)
    cob(kk,1)=lsq(kk,1)-coa(kk,1)*sn(kk,2);
end
kk = length(cob);
cob(kk+1,1)=cob(kk,1);

% Pick the optimal coa (coefficient A = cell F17) = coaf
% Pick the optimal cob (coefficient B = cell G17) = cobf
for kk = 1:length(yy)
    for mm=1:length(coa)-1
        if yy(kk,1)>=max(sn(:,2))
             coaf(kk,1)=coa(mm,1);
             cobf(kk,1)=cob(mm,1);
        elseif yy(kk,1)>=sn(mm,2) & yy(kk,1) < sn(mm+1,2)
             coaf(kk,1)=coa(mm,1);
             cobf(kk,1)=cob(mm,1);
        end
    end
end

% Apply final calibration
for kk = 1:length(yy)
       yyc(kk,1) = (exp(sqrt(coaf(kk,1)*yy(kk,1)+cobf(kk,1)))-1)/10;
end
```

Fig. A-10. MATLAB code used to calibrate the thermal anemometers based on the information provided in the Microsoft Excel spreadsheet by Dantec Dynamics (Fig. A-9).

VITA

Name: Jean Taylor Ellis

Address: Department of Geography, Texas A&M University, College Station, TX 77843-3147

Email Address: jean@geog.tamu.edu

Education: B.S., Environmental Studies (Biology), minor Geography, University of Southern California, 1999
M.S., Geography, University of Southern California, 2001